iScience

CellPress
OPEN ACCESS

Article

Early death of ALS-linked CHCHD10-R15L transgenic mice with central nervous system, skeletal muscle, and cardiac pathology

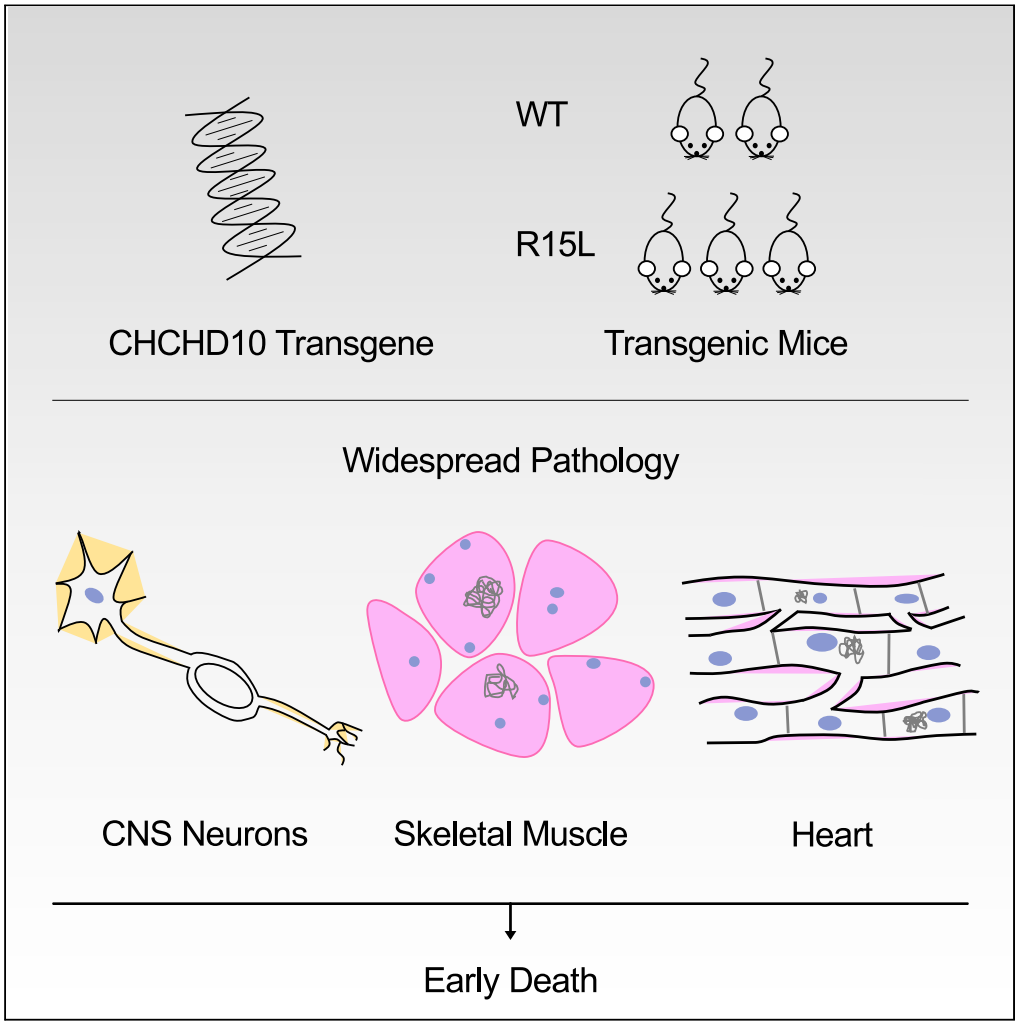

Éanna B. Ryan, Jianhua Yan, Nimrod Miller, Sudarshan Dayanidhi, Yongchao C. Ma, Han-Xiang Deng, Teepu Siddique

t-siddique@northwestern.edu

HIGHLIGHTS

Transgenic mice expressing wild-type or ALS-linked CHCHD10 p.R15L developed

CHCHD10-R15L mice display widespread axonal swellings in the CNS

Mice perform well in motor tests despite CNS, skeletal muscle, and cardiac pathology

Early death of CHCHD10-R15L mice likely due to cardiac failure

Ryan et al., iScience 24, 102061
February 19, 2021
https://doi.org/10.1016/j.isci.2021.102061

iScience

CellPress
OPEN ACCESS

Article

Early death of ALS-linked CHCHD10-R15L transgenic mice with central nervous system, skeletal muscle, and cardiac pathology

Éanna B. Ryan,[1,2] Jianhua Yan,[1] Nimrod Miller,[3] Sudarshan Dayanidhi,[4] Yongchao C. Ma,[3] Han-Xiang Deng,[1] and Teepu Siddique[1,2,5,6,7,*]

SUMMARY

Mutations in coiled-coil-helix-coiled-coil-helix domain containing 10 (*CHCHD10*) have been identified in patients suffering from various degenerative diseases including mitochondrial myopathy, spinal muscular atrophy Jokela type, frontotemporal dementia, and/or amyotrophic lateral sclerosis (ALS). The pathogenic mechanism underlying *CHCHD10*-linked divergent disorders remains largely unknown. Here we show that transgenic mice overexpressing an ALS-linked CHCHD10 p.R15L mutation leads to an abbreviated lifespan compared with CHCHD10-WT transgenic mice. The occurrence and severity of the phenotype correlates to transgene copy number. Central nervous system (CNS), skeletal muscle, and cardiac pathology is apparent in CHCHD10-R15L transgenic mice. Despite the pathology, CHCHD10-R15L transgenic mice perform comparably to control mice in motor behavioral tasks until very close to death. Although paralysis is not observed, these models provide insight into the pleiotropic nature of CHCHD10 and suggest a contribution of CNS, skeletal muscle, and cardiac pathology to CHCHD10 p.R15L-ALS pathogenesis.

INTRODUCTION

Amyotrophic lateral sclerosis (ALS) is a fatal neurodegenerative disease characterized by the degeneration of upper and lower motor neurons leading to paralysis, and ultimately death, usually within 3 to 5 years of diagnosis (Brown and Al-Chalabi, 2017). The causes of ALS are mostly unknown; however, approximately 10% of cases are recognized as familial. The causative genetic mutation has been identified in approximately 60% of these familial ALS (FALS) cases. The most common genes identified to be mutated in ALS patients include *SOD1*, *C9orf72*, and *FUS* (Rosen et al., 1993; Dejesus-Hernandez et al., 2011; Renton et al., 2011; Vance et al., 2009; Kwiatkowski et al., 2009), with over twenty more genes implicated to a lesser extent. One such gene is coiled-coil-helix-coiled-coil-helix domain containing 10 (*CHCHD10*). Mutations have been reported in *CHCHD10* in individuals affected with ALS as well as in other degenerative diseases including mitochondrial myopathy, other motor neuron phenotypes such as the Jokela type of spinal muscular atrophy, and frontotemporal dementia (FTD), among others (Bannwarth et al., 2014; Ajroud-Driss et al., 2015; Muller et al., 2014; Johnson et al., 2014; Jiao et al., 2016; Penttila et al., 2015; Kurzwelly et al., 2015; Project Mine ALS Sequencing Consortium, 2018; Auranen et al., 2015; Zhang et al., 2015; Lehmer et al., 2018). *CHCHD10* is understood to encode for a mitochondrial protein. This could provide a direct etiological link between mitochondrial dysfunction and ALS pathogenesis.

CHCHD10 is so named due to the presence of two coiled coil helices, which each contain two cysteines separated by any nine amino acids (CX_9C). The disulfide relay system facilitates the import of a CHCH-domain containing protein from the cytosol into the mitochondrial intermembrane space. The protein enters the intermembrane space in a reduced state, and, upon encountering CHCHD4/Mia40, disulfide bridges are formed to link the cysteines of one coiled-coil helix with the other and the maturely folded protein is maintained in the intermembrane space (Fischer and Riemer, 2013; Riemer et al., 2011; Herrmann and Riemer, 2012). The function(s) of CHCHD10 continues to be investigated. Proposals include, but are not limited to, a role for CHCHD10 in the mitochondrial contact site and cristae organizing system (MICOS) (Genin et al., 2016) as has been described for CHCHD3 and CHCHD6 (Darshi et al., 2012; Ott et al., 2015; An et al., 2012), although conflicting data questions this role (Huang et al., 2018; Burstein et al., 2018).

[1]The Ken and Ruth Davee Department of Neurology, Northwestern University Feinberg School of Medicine, Tarry Building, Room 13-715, 303 East Chicago Avenue, Chicago, IL 60611, USA

[2]Northwestern University Interdepartmental Neuroscience Program, Chicago, IL, USA

[3]Ann and Robert H. Lurie Children's Hospital of Chicago and Departments of Pediatrics, Neurology and Physiology, Northwestern University Feinberg School of Medicine, Chicago, IL, USA

[4]Shirley Ryan AbilityLab and Department of Physical Medicine and Rehabilitation, Northwestern University Feinberg School of Medicine, Chicago, IL, USA

[5]Department of Cell and Developmental Biology, Northwestern University Feinberg School of Medicine, Chicago, IL, USA

[6]Department of Pathology, Northwestern University Feinberg School of Medicine, Chicago, IL, USA

[7]Lead Contact

*Correspondence: t-siddique@northwestern.edu

https://doi.org/10.1016/j.isci.2021.102061

CHCHD10 has also been proposed as a regulator of the efficiency of action of the electron transport chain (Burstein et al., 2018; Straub et al., 2018; Purandare et al., 2018) and as a biorganellar protein with a nuclear role in the regulation of gene transcription (Purandare et al., 2018). The latter function is similar to that proposed for CHCHD2 (Aras et al., 2015), mutations of which have been identified in familial Parkinson disease (PD) patients (Funayama et al., 2015). Expression of both CHCHD10 and CHCHD2 has been shown to be sensitive to oxygen tension (Purandare et al., 2018), and loss of one impacts the expression level of the other (Purandare et al., 2018; Huang et al., 2018). Protein-protein interactions and functional redundancy have been observed between CHCHD10 and CHCHD2 (Huang et al., 2018; Burstein et al., 2018; Straub et al., 2018).

Investigations examining the impact of knockdown (KD) or knockout (KO) of CHCHD10/CHCHD2 orthologs in *C. elegans*, zebrafish, and drosophila have been performed, and a variety of phenotypes were observed (Woo et al., 2017; Brockmann et al., 2018; Meng et al., 2017). Often, rescue was accomplished with introduction of the human wild-type CHCHD10 or CHCHD2 but not disease-linked mutations leading the authors to propose loss-of-function mechanisms of disease. It must be noted that a phenotype arising due to KD or KO of these orthologs cannot be attributed to loss of either CHCHD10 or CHCHD2 specifically, due to their homology. The *C. elegans* ortholog shares ~41% amino acid identity with CHCHD10 and CHCHD2. The zebrafish ortholog shares ~65% and ~57% amino acid identity with CHCHD10 and CHCHD2, respectively. The drosophila ortholog shares ~37% and ~48% amino acid identity with CHCHD10 and CHCHD2, respectively. The discordance in protein homology is amplified in the N-terminus, making it difficult to assess the impact of introduction of the human CHCHD10 p.R15L mutant, in particular, into these model systems.

Murine Chchd10 shares ~85% amino acid identity with human CHCHD10 and ~51% amino acid identity with human CHCHD2. Short-term studies of Chchd10-KO mice do not reveal a striking phenotype (Burstein et al., 2018; Liu et al., 2020b; Anderson et al., 2019). However, Chchd10/Chchd2 double KO mice display a variety of phenotypes including vacuolar pathology and abnormal mitochondrial cristae structure in the heart along with echocardiographic deficits (Liu et al., 2020b). Furthermore, the double KO mice display increased OMA1 cleavage of OPA1 and upregulation of the mitochondrial integrated stress response. The same study reported similar deficits in Chchd10 p.S55L knock-in (KI) mice, which model the human CHCHD10 p.S59L mutation that was identified in patients with complex and varying phenotypes including myopathy, ataxia, cognitive impairment, motor neuron disease and deafness, as well as a singleton ALS-FTD case (Bannwarth et al., 2014). Combined, these data lead the authors to propose that aggregation prone CHCHD10 p.S59L may act through a dominant negative mechanism by pulling soluble CHCHD10 and CHCHD2 into an insoluble fraction, thereby mimicking the double KO mice. Alternatively, or additionally, the insoluble fraction may act through a toxic gain-of-function mechanism. Further investigation is required to distinguish between the two mechanisms.

Chchd10 p.S55L KI mice were previously developed by two other independent groups (Anderson et al., 2019; Genin et al., 2019). Both groups report a survival of ~330 days. One group reports progressive motor deficits, myopathy, cardiomyopathy, Chchd10 aggregation, and upregulation of the mitochondrial integrated stress response (Anderson et al., 2019). None of these phenotypes were observed in Chchd10-KO mice, leading the authors to propose a toxic gain-of-function mechanism of action of Chchd10 p.S55L but cautioned that loss-of-function or dominant negative mechanisms may still play a role in human disease manifestation. The second group report a variety of mitochondrial ultrastructure, mitochondrial DNA, and respiratory chain deficiencies in muscle, heart, brain, and spinal cord (Genin et al., 2019). The authors propose that early myopathic changes precede central nervous system involvement. A conditional skeletal muscle knockout mouse model has also been developed and displays some mild motor deficits, along with neuromuscular junction structural and electrophysiological deficits (Xiao et al., 2019).

Combined, these data from *in vivo* models highlight the importance of functional redundancy between CHCHD10 and CHCHD2, the tissue-specific impact of mutations, and that the underlying mechanism of disease for individual mutations remains to be fully elucidated.

As part of efforts to identify genetic causes of ALS, we identified a CHCHD10 p.R15L mutation in five FALS pedigrees (Manuscript in preparation). This mutation has also been identified by five other independent research groups and is likely responsible for <1% of FALS cases (Muller et al., 2014; Kurzwelly et al.,

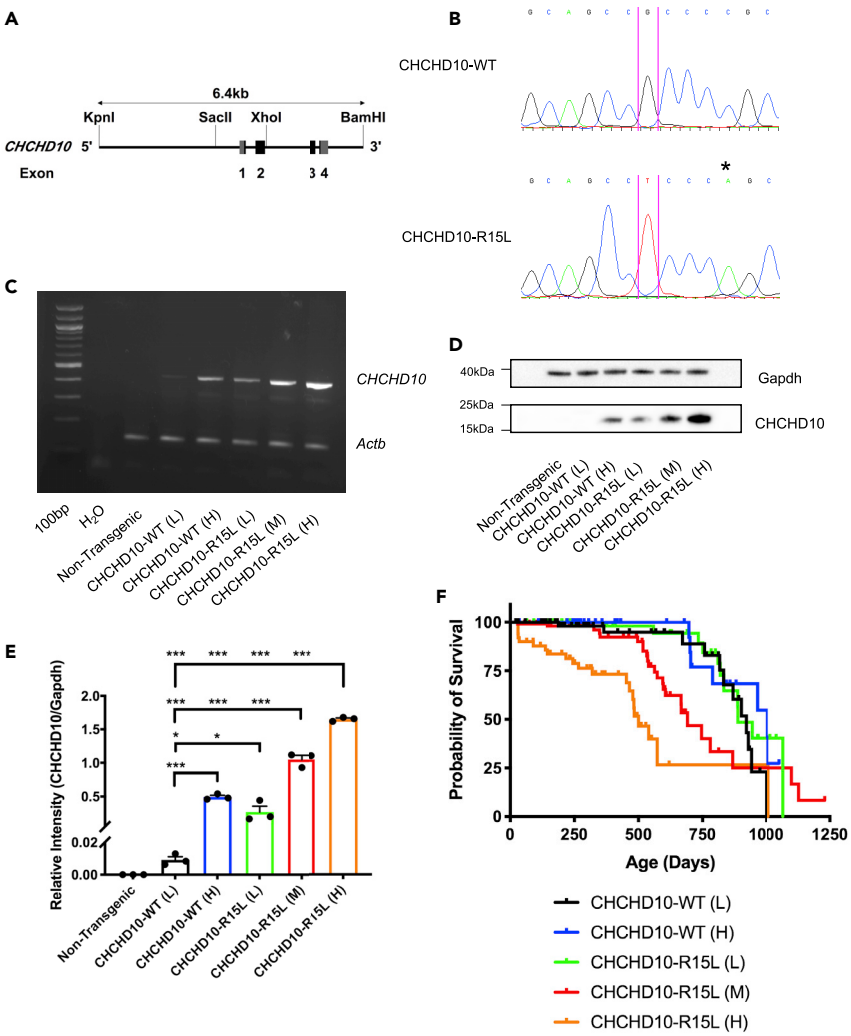

Figure 1. Development and survival analysis of CHCHD10 transgenic mice

(A) 6.4kb human *CHCHD10* transgene design indicating restriction enzyme cutting sites and exons 1–4. Gray boxes represent untranslated regions. Black boxes represent translated regions.

(B) Electropherograms displaying the nucleotide sequences of CHCHD10-WT and CHCHD10-R15L transgenes identified in mouse tail DNA. The pathogenic G > T change leading to the R15L mutation is indicated in pink. A C > A change in the CHCHD10-R15L lines, indicated by the overlying asterisk, is a reported synonymous SNP in humans (rs179468) that was also introduced during site-directed mutagenesis.

(C) Agarose gel displaying PCR amplification products of indicated mouse tail DNA using primers directed against human *CHCHD10* and murine *Actb*. A non-transgenic mouse tail DNA sample and H_2O sample are used as negative controls, demonstrating the specificity of the primers used. The relative transgene copy number is demonstrated qualitatively.

(D) Western blot analysis of transgene expression at the protein level. Mouse forebrain lysate was prepared using RIPA buffer, and immunoblotting was carried out using the indicated antibodies.

(E) Quantitation of transgenic human CHCHD10 protein expression in indicated mouse lines from n = 3 independent experiments. Data are represented as mean ± SEM. One-way ANOVA with Tukey's multiple comparison test, *p < 0.05, ***p < 0.001.

(F) Kaplan-Meier survival analysis of the indicated CHCHD10 founder lines. Death of a mouse for unknown reasons is considered a death event, as indicated by a drop in the line. Mice still living or death of a mouse due to intervention by the investigators are considered censored events, as indicated by tick marks along a line. Median survival for CHCHD10-WT (L) is 921 days, n = 12 death events and n = 76 censored events. Median survival for CHCHD10-WT (H) is 1,003 days, n = 7 death events and 51 censored events. Gehan-Breslow-Wilcoxon test, p = 0.1847 in comparison to CHCHD10-WT (L) line. Median survival for CHCHD10-R15L (L) is 888 days, n = 11 death events and 83 censored events. Gehan-Breslow-Wilcoxon test, p = 0.5900 in comparison to CHCHD10-WT (L) line. Gehan-Breslow-Wilcoxon test, p = 0.5879 in comparison to CHCHD10-WT (H) line. Median survival for CHCHD10-R15L (M) is 691 days, n = 24 death events and n = 107 censored

Figure 1. *Continued*
events. Gehan-Breslow-Wilcoxon test, p = 0.0317 comparison to CHCHD10-WT (L) line. Gehan-Breslow-Wilcoxon test, p = 0.0062 in comparison to CHCHD10-WT (H) line. Median survival for CHCHD10-R15L (H) is 500 days, n = 21 death events and n = 30 censored events. Gehan-Breslow-Wilcoxon test, p < 0.0001 in comparison to CHCHD10-WT (L) line. Gehan-Breslow-Wilcoxon test, p < 0.0001 in comparison to CHCHD10-WT (H) line.

2015; Johnson et al., 2014; Project Mine ALS Sequencing Consortium, 2018; Zhang et al., 2015). In the current study, we sought to investigate ALS pathogenesis caused by the CHCHD10 p.R15L mutation. We undertook the approach of engineering transgenic mouse models expressing the human *CHCHD10* gene with, and without, the p.R15L mutation under the control of the endogenous *CHCHD10* gene promoter. We have observed a range of striking pathologies of the CNS, skeletal muscle, and heart in CHCHD10-R15L transgenic mice that result in an abbreviated lifespan in a copy-number-correlated fashion.

RESULTS

Development of CHCHD10 transgenic mouse lines

We constructed a 6.4kb *KpnI/BamHI* human *CHCHD10* genomic DNA transgene using a human genomic DNA BAC clone (RP11-124F9, 180.7kb) as a template. The transgene was assembled by ligation of three fragments (Figure 1A). The transgene includes the promoter region of 3.4kb upstream of the CHCHD10 transcription starting site, all four exons and three introns of *CHCHD10*, and 0.7kb fragment downstream of the *CHCHD10* poly(A) signal (Figure 1A). The ALS-linked CHCHD10 p.R15L mutation was introduced by site-directed mutagenesis (Figure 1B). A reported synonymous SNP in humans (rs179468) was also introduced to the CHCHD10-R15L construct during site-directed mutagenesis. Transgenic mouse lines were established by microinjection of the transgene into fertilized eggs. Analysis of the transgene copy number and transgenic protein expression levels indicated that the CHCHD10-WT (L) line had significantly lower transgene copy number and expression than that of the CHCHD10-R15L lines (Figures 1C–1E). We subsequently performed another round of transgene microinjection and identified a mouse line, CHCHD10-WT (H), with a transgene copy number and transgenic protein expression level higher than that of the low-expressing CHCHD10-R15L (L) line.

The transgenic mouse lines examined in this study include a low-expressing CHCHD10-WT (L) line, a high-expressing CHCHD10-WT (H) line, a low-expressing CHCHD10-R15L (L) line, a medium-expressing CHCHD10-R15L (M) line, and a high-expressing CHCHD10-R15L (H) line (Figures 1C–1E). The CHCHD10-R15L (H) line is particularly difficult to breed, as demonstrated by a reduced litter size at P21 compared with other genotypes, and only 22% of mice weaned at P21 being transgenic, compared with the expected 50% (Figure S1). These data do not account for death of mice or cannibalism by a parent before P21. Strikingly, CHCHD10-R15L (M) and CHCHD10-R15L (H) transgenic mice die unexpectedly before the CHCHD10-WT (L) and CHCHD10-WT (H) mice in a copy-number-correlated fashion (Figures 1F, S2A, and S2B).

Behavioral and phenotypic testing reveal differences between CHCHD10-WT and CHCHD10-R15L lines

A cohort of mice from the CHCHD10-WT (L), CHCHD10-WT (H), and CHCHD10-R15L (M) lines was monitored for body weight and rotarod performance in a longitudinal study in order to examine the general health and motor ability of the transgenic mouse lines. Mice were tested every 60 days, beginning at 60 days of age. Rotarod performance is comparable between the lines available up to the 600-day time point (Figures 2A, S2C, and S2D, Tables S1–S18). Following on from this, there is a combination of early death of CHCHD10-R15L (M) mice and a precipitous decline in the rotarod performance of those surviving. These phenomena are preceded by a notable loss of body weight compared with the CHCHD10-WT (L) mice, although body weight is similar between CHCHD10-WT (H) and CHCHD10-R15L (M) mice (Figures 2B and 2C, Tables S19–S30). The motor behavior of separate cohorts of 4-month-old and 14- to 20-month-old mice was monitored in an open field test. All genotypes traveled similar distances at similar velocities over the course of the experiment (Figures 2D–2G). As an approximate measure of anxiety-like behavior, all genotypes of mice spent an equivalent length of time in the periphery and center of the open field at both ages (Figures 2H–2K) (Seibenhener and Wooten, 2015; Simon et al., 1994). DigiGait analysis reveals few statistically significant gait disturbances between CHCHD10-WT (L) and CHCHD10-R15L (M) transgenic mice (Tables S31 and S32), with the vast majority of parameters tested equivalent between the two lines at both ages. We noted that a greater number of 20-month-old CHCHD10-R15L (M) mice were

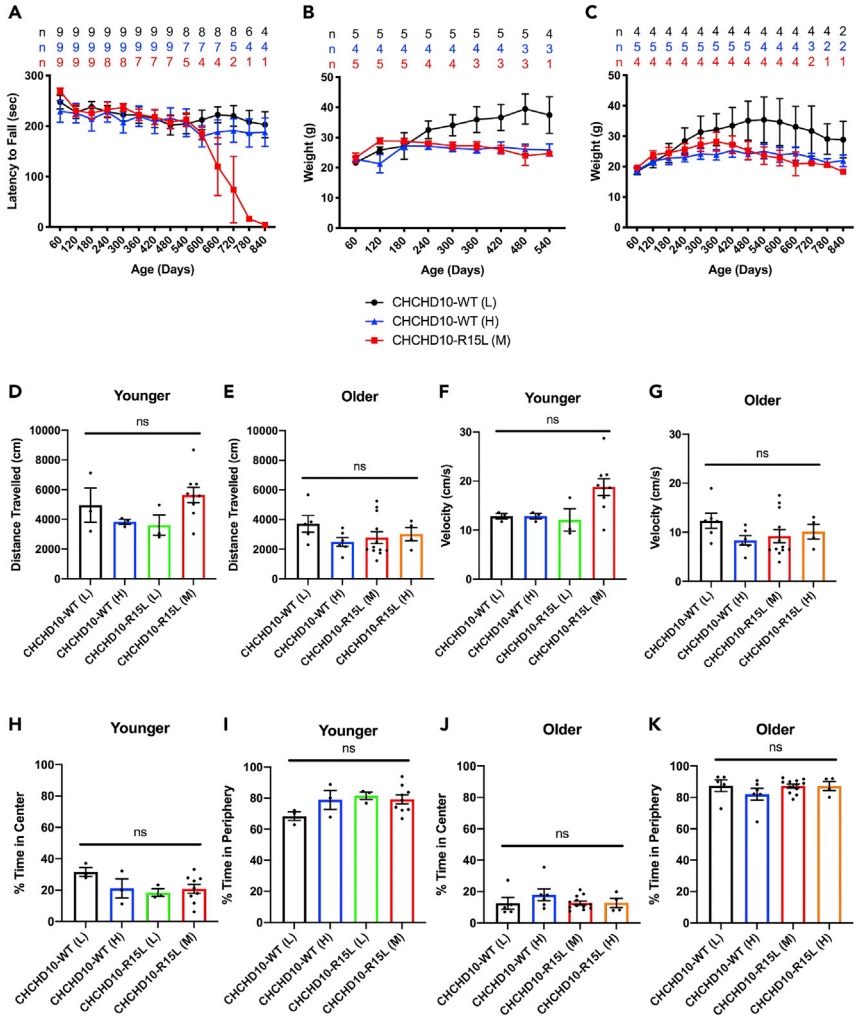

Figure 2. Behavioral testing of CHCHD10 transgenic mouse lines

(A) Mouse rotarod performance. Mice were tested on an accelerating rotarod task every 60 days beginning at 60 days of age until all CHCHD10-R15L (M) mice in the cohort died. The overlying numbers indicate the number of mice from each line used to calculate mean latency to fall at each time point. Data are represented as mean ± SEM. Two-way ANOVA with Holm-Šidák post hoc statistical analysis summarized in Tables S1–S6.

(B) Male mouse body weight measurements. Mouse body weight was measured every 60 days beginning at 60 days of age until all male CHCHD10-R15L (M) mice in the cohort died. The overlying numbers indicate the number of mice from each line used to calculate mean body weights at each time point. Data are represented as mean ± SEM. Two-way ANOVA with Holm-Šidák post hoc statistical analysis summarized in Tables S25–S30.

(C) Female mouse body weight measurements. Mouse body weight was measured every 60 days beginning at 60 days of age until all female CHCHD10-R15L (M) mice in the cohort died. The overlying numbers indicate the number of mice from each line used to calculate mean body weights at each time point. Data are represented as mean ± SEM. Two-way ANOVA with Holm-Šidák post hoc statistical analysis summarized in Tables S19–S24.

(D) The mean distance traveled by 4-month-old mice of the indicated lines in an open field test over five minutes. Data are represented as mean ± SEM. One-way ANOVA with Tukey's multiple comparison test, ns $p > 0.05$.

(E) The mean distance traveled by 14- to 20-month-old mice of the indicated lines in an open field test over 5 minutes. Data are represented as mean ± SEM. One-way ANOVA with Tukey's multiple comparison test, ns $p > 0.05$.

(F) The mean velocity of 4-month-old mice of the indicated lines in an open field test over 5 minutes. Data are represented as mean ± SEM. One-way ANOVA with Tukey's multiple comparison test, ns $p > 0.05$.

(G) The mean velocity of 14- to 20-month-old mice of the indicated lines in an open field test over 5 minutes. Data are represented as mean ± SEM. One-way ANOVA with Tukey's multiple comparison test, ns $p > 0.05$.

(H) The mean percentage time spent in the center of the open field by 4-month-old mice of the indicated lines. Data are represented as mean ± SEM. One-way ANOVA with Tukey's multiple comparison test, ns $p > 0.05$.

Figure 2. *Continued*

(I) The mean percentage time spent in the periphery of the open field by 4-month-old mice of the indicated lines. Data are represented as mean ± SEM. One-way ANOVA with Tukey's multiple comparison test, ns $p > 0.05$.

(J) The mean percentage time spent in the center of the open field by 14- to 20-month old mice of the indicated lines. Data are represented as mean ± SEM. One-way ANOVA with Tukey's multiple comparison test, ns $p > 0.05$.

(K) The mean percentage time spent in the periphery of the open field by 14- to 20-month-old mice of the indicated lines. Data are represented as mean ± SEM. One-way ANOVA with Tukey's multiple comparison test, ns $p > 0.05$.

unable to complete the task at higher belt speeds compared with CHCHD10-WT (L) mice (Table S33). However, those mice unable to perform at higher belt speeds performed, comparably to CHCHD10-WT (L) mice, at slower belt speeds, demonstrating their ability to execute the movement but their sensitivity to the intensity of the task. A loss of motivation to perform the task at higher belt speeds could also arise due to cognitive impairment, rather than the development of motor deficits. These behavioral tests of motor function demonstrate that CHCHD10-R15L (M) mice perform, comparably to controls, until close to the point of death. Paralysis was never observed to occur before death.

Profound central nervous system pathology of CHCHD10-R15L transgenic mice

Given the progressive behavioral deficits apparent in the CHCHD10-R15L (M) transgenic mice, we analyzed the pathology of the central nervous system at various timepoints. When using either commercial or in-house designed antibodies directed against CHCHD10-specific epitopes, we observe a remarkable and widespread pathology in CHCHD10-R15L transgenic mice characterized by abnormal swellings along neuritic processes (Figures 3A–3J, S3, and S4). These swellings often contain a strongly immunoreactive component, localized to a focal point on the periphery of the swelling. The CNS pathology is present in all three lines, including the lowest expressing line, although the pathology is more florid in the higher expressors (Figure 3K). This pathology first becomes apparent at 60 days of age in CHCHD10-R15L (M) mice (Figure S6). The pathology appears to arise due to the CHCHD10-R15L mutation, rather than an artifact of transgene overexpression as it is absent from both CHCHD10-WT (L) and CHCHD10-WT (H) transgenic mouse lines and is present in all CHCHD10-R15L lines, regardless of copy number. Given the reported mitochondrial and nuclear localization of CHCHD10, this immunohistochemical profile is surprising, as it does not reflect a typical mitochondrial or nuclear staining profile.

In order to determine the nature of the neuritic processes harboring these abnormal swellings, we analyzed the colocalization of either dendritic or axonal markers with CHCHD10. This revealed an overlap between CHCHD10 and neurofilament markers (SMI 32, SMI 310R, and NF-68) but not Map2-positive dendrites (Figures 4A–4F, and S4A–S4F). Confirmation of the neuronal, and specifically axonal, location of these swellings was provided by ultrastructural analysis with transmission electron microscopy (Figures 4G, 4H, and S6A–S6F). This revealed myelinated axons harboring membrane-bound swellings with an amorphous matrix. The membrane lining is predominantly a single membrane with focal accumulations of membranous whorls protruding into the swelling visible in most cases. These are likely to be the strongly immunoreactive components observed by immunohistochemistry.

Given the known mitochondrial location of CHCHD10, we examined whether mitochondrial proteins contribute to any component of the axonal swellings. Firstly, the unusual staining pattern of long stretches of neuritic processes observed using various CHCHD10 antibodies was specific to those antibodies and not observed when using other antibodies directed against mitochondrial proteins. Interestingly, although the vast majority of the membranes of the swellings did not co-localize with other mitochondrial markers, the strongly immunoreactive CHCHD10-positive focal components often co-localized with mitochondrial markers. This co-localization was most prominent for inner mitochondrial membrane proteins, ATP synthase α subunit, and COX IV subunit VIb (Figures S4G–S4L).

By using the endogenous *CHCHD10* gene promoter to drive expression of the transgene, we did not restrict expression to any particular known cell type. Indeed, the pathological swellings observed are present in axons of a variety of neurons throughout the CNS. To describe the CHCHD10-R15L (M) line in detail, the swellings are apparent in cholinergic motor neurons in the spinal cord anterior horn (Figures S5 and S7). Prominent swellings are also apparent in the anterior commissure of the spinal cord. They can be observed in all levels and laminae of the spinal cord gray matter, with a greater abundance in the anterior gray matter. Swellings are numerous and apparent in the brainstem of all CHCHD10-R15L transgenic mouse lines and to varying extents in other brain regions (Figure S8). We examined whether pathology extended to the

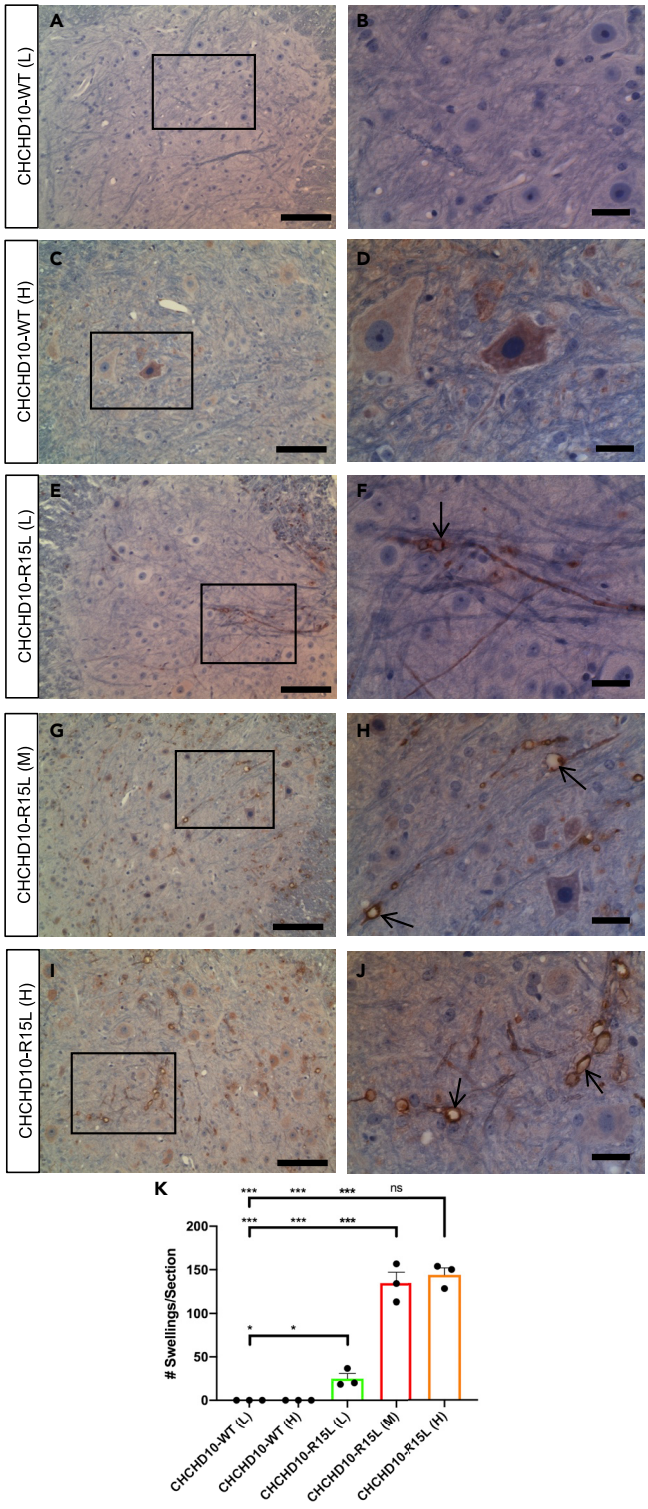

Figure 3. CNS pathology of CHCHD10-R15L transgenic mice

(A) A 20-month-old male CHCHD10-WT (L) anterior horn from one side of a transverse spinal cord section stained using an antibody targeting CHCHD10. Region within black box outline is magnified in (B). Scale bar: 100 μm.

(B) Higher magnification of region indicated in (A). Scale bar: 25 μm.

Figure 3. *Continued*

(C) A 35-month-old male CHCHD10-WT (H) anterior horn from one side of a transverse spinal cord section stained using an antibody targeting CHCHD10. Region within black box outline is magnified in (D). Scale bar: 100 μm.
(D) Higher magnification of region indicated in (C). Scale bar: 25 μm.
(E) A 10-month-old male CHCHD10-R15L (L) anterior horn from one side of a transverse spinal cord section stained using an antibody targeting CHCHD10. Region within black box outline is magnified in (F). Scale bar, 100 μm.
(F) Higher magnification of region indicated in (E) demonstrates the presence of neuritic processes with swellings along the length of the neuritic process. Example of a swelling is indicated by a black arrow. Scale bar, 25 μm.
(G) A 13-month-old male CHCHD10-R15L (M) anterior horn from one side of a transverse spinal cord section stained using an antibody targeting CHCHD10. Region within black box outline is magnified in (H). Scale bar, 100 μm.
(H) Higher magnification of region indicated in (G) demonstrates the presence many neuritic processes with swellings that appear either in isolation or in sequence along the length of the neuritic process. Examples of swellings are indicated by black arrows. Scale bar, 25 μm.
(I) A 14-month-old female CHCHD10-R15L (H) anterior horn from one side of a transverse spinal cord section stained using an antibody targeting CHCHD10. Region within black box outline is magnified in (J). Scale bar, 100 μm.
(J) Higher magnification of region indicated in (I) demonstrates the presence many neuritic processes with swellings along the length of the neuritic process. Examples of swellings are indicated by black arrows. Scale bar, 25 μm.
(K) Quantitation of the number of swellings in the right and left lumbar spinal cord anterior horn gray matter per section of 8- to 14-month-old mice (n = 3, m = 3/genotype). Data are represented as mean ± SEM. One-way ANOVA with Tukey's multiple comparison test, ns $p > 0.05$, *$p < 0.05$, ***$p < 0.001$.

peripheral nervous system by analyzing the numbers and caliber distribution of femoral nerve motor branch axons. No difference in axon number or axon caliber distribution was apparent between the transgenic lines examined (Figures S9A–S9D, Table S34). These data indicate that the CNS pathology does not result in a loss of motor neurons that give rise to peripheral motor axons.

Given the mitochondrial location of CHCHD10 and the CNS axonal pathology observed, we analyzed the movement of mitochondria in the axons of primary neurons derived from E12.5 embryonic spinal cords. This assay revealed a reduction in both the anterograde and the retrograde movement of mitochondria of CHCHD10-R15L (M) primary neurons compared with non-transgenic primary neurons derived from littermates (Figure S9E). Net movement of CHCHD10-R15L (M) mitochondria is in the retrograde direction, and this can be accounted for by a reduction in the percent of time mitochondria were observed moving anterogradely (Figure S9F). There was no difference in the mitochondrial density or basal oxygen consumption rate of these neurons, but there was a slight increase in the length of CHCHD10-R15L (M) mitochondria compared with non-transgenic mitochondria (Figures S9G–S9I). Taken together, these data suggest deficits in mitochondrial trafficking and dynamics of CHCHD10-R15L (M) mouse spinal cord neurons with the caveat that these deficits may arise due to transgene over-expression and/or the mutation.

Cytoplasmic p62-positive skein-like inclusions in motor neurons are a pathological hallmark of ALS. Loss of nuclear TDP-43 and cytoplasmic TDP-43 inclusions are a common pathological feature in ALS cases, with notable exceptions including, but not limited to, SOD1-ALS (Mackenzie et al., 2007). Although we do not observe cytoplasmic p62-positive skein-like inclusions in motor neurons, abundant punctate p62-positive immunoreactivity is apparent in the spinal cord gray matter of CHCHD10-R15L (M) and CHCHD10-R15L (H) mice (Figure S10). The identity of the cells and cellular compartments harboring these p62-positive puncta remains to be determined. Immunohistochemical staining of spinal cord using an antibody targeting TDP-43 appears typical with prominent nuclear immunoreactivity (Figure S10).

Skeletal and cardiac muscle pathology of CHCHD10-R15L transgenic mice

The relatively long life-span and unexpected death of CHCHD10-R15L transgenic mice over a wide time frame suggests cardiopulmonary failure as the immediate cause of death. Given the severe CNS pathology that is apparent at least from 60 days of age in CHCHD10-R15L (M) mice in axons of a wide array of neurons of diverse neuronal systems, the length of the lifespan, although abbreviated, is quite surprising. We observed, however, that the respiratory rate of the CHCHD10-R15L (M) mice appeared to be increased in the weeks before death. This led us to examine the muscular pathology of the diaphragm, which revealed some striking features (Figures S11D–S11F). There is an obvious increase of connective tissue and cellularity between myofibers. We expanded this analysis to include the quadriceps and gastrocnemius of other mouse lines and observe similar myopathic changes (Figures 5A–5F, and S11A–S11C). Many abnormal myofiber profiles are apparent by hematoxylin and eosin (H&E) staining such as short diameter fibers, cytoplasmic hematoxylin invasion with focal eosinophilic cores, and central nuclei. Upon immunohistochemical

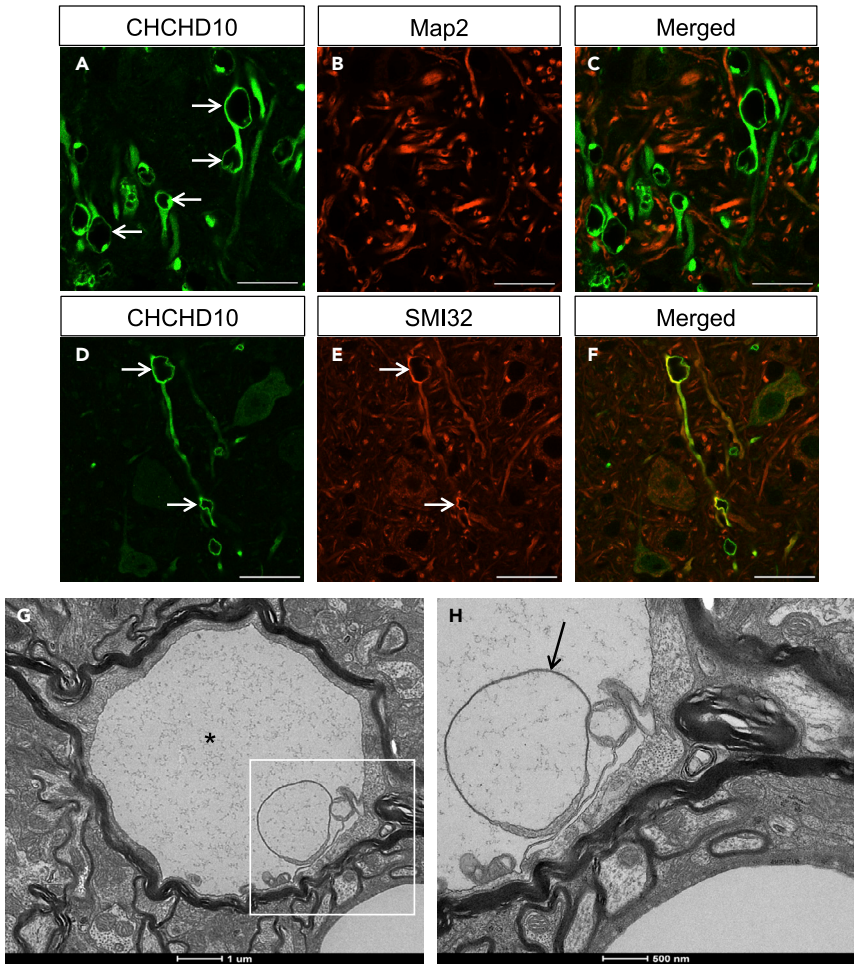

Figure 4. CNS axonal pathology evident in CHCHD10-R15L transgenic mice

(A–C) Immunofluorescence of 10-month-old CHCHD10-R15L (M) transgenic mice spinal cord gray matter using antibodies targeting CHCHD10 and the dendritic protein, Map2. The staining profiles are mutually exclusive, indicating that neuronal dendrites do not harbor the pathological swellings (examples indicated by white arrows). Scale bars, 25 μm.

(D–F) Immunofluorescence of 10-month-old CHCHD10-R15L (M) transgenic mice spinal cord gray matter using antibodies targeting CHCHD10 and SMI 32, non-phosphorylated neurofilament heavy chain protein. White arrows indicate SMI 32-positive neurites harbor pathological swellings. Scale bars, 25 μm.

(G) Transmission electron microscopy image of 5-month-old CHCHD10-R15L (M) transgenic mouse spinal cord gray matter. A myelinated axon is apparent harboring a swelling resembling those observed under light microscopy (black asterisk). The white box outline is magnified in (H).

(H) Membranous protrusions into the amorphous matrix of the swelling are apparent (black arrow).

analysis, we again observed an unusual staining profile when using antibodies targeting CHCHD10. Staining was absent from some myofibers. Other myofibers harbored CHCHD10-positive accumulations some of which, but not all, were p62-positive (Figures 6G–6N). Electron microscopy reveals large fibrous interruptions of unknown composition to the myofibrillary network (Figures S11G–S11J). Despite the severe pathology, high-resolution respirometry analysis of soleus or tibialis anterior muscles does not reveal any difference in the oxygen consumption of 7- to 8-month-old mice (Figures 6O and 6P), indicating that mitochondrial oxidative phosphorylation capacity is not compromised, at least at this relatively early stage in CHCHD10-R15L (M) transgenic mice skeletal muscle.

We carried out an echocardiography study of younger and older cohorts of mice to determine whether any cardiac impairment might contribute to the early death of CHCHD10-R15L transgenic mice. No statistically significant difference was observed in any parameter tested, including, but not limited to, cardiac output,

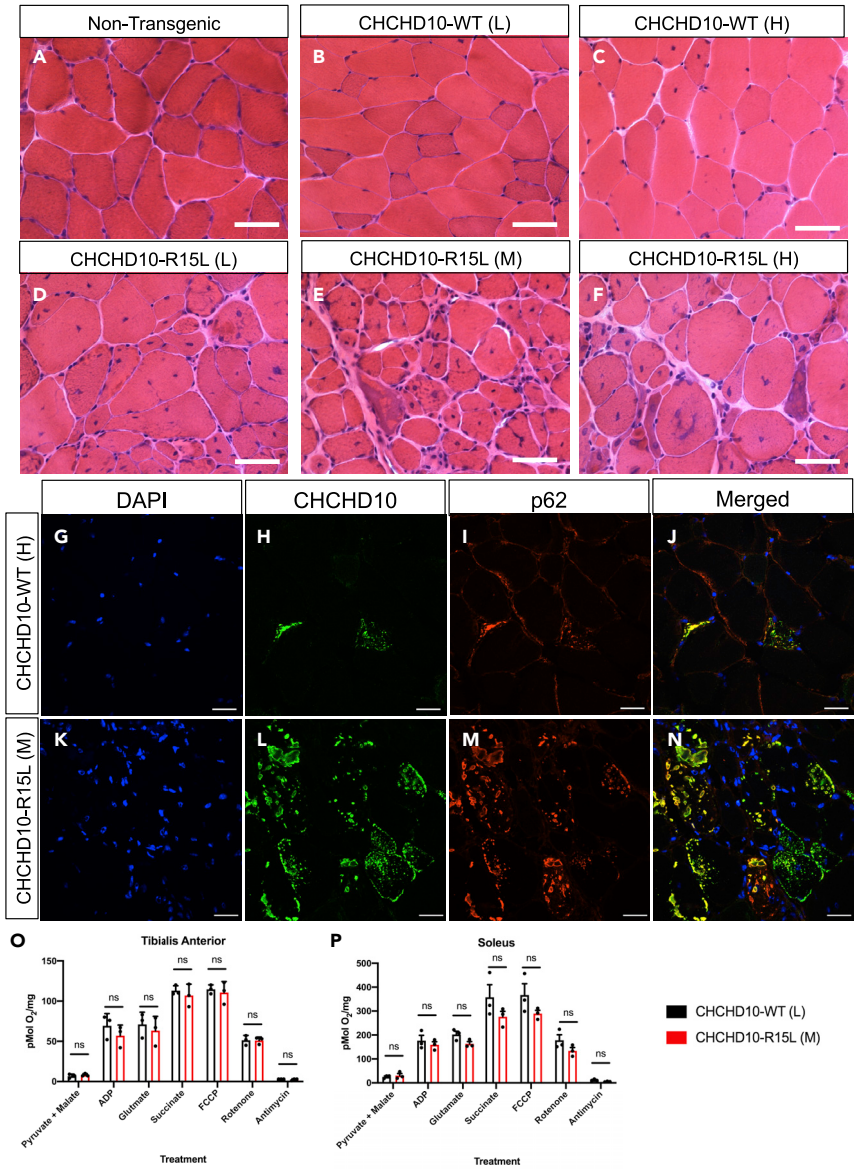

Figure 5. Widespread myopathic abnormalities in CHCHD10-R15L transgenic mice

(A–F) Hematoxylin and eosin staining of quadriceps of a 22-month-old female non-transgenic mouse (A), a 5-month-old male CHCHD10-WT (L) mouse (B), a 14-month-old female CHCHD10-WT (H) mouse (C), a 23-month-old female CHCHD10 R15L (L) mouse (D), a 15-month-old female CHCHD10-R15L (M) mouse (E), and a 12-month-old male CHCHD10-R15L (H) mouse (F). Abundant myopathic features are apparent in the CHCHD10-R15L transgenic mice including central nuclei, hematoxylin invasion, eosinophilic cores, and increased intermyofibrillary cellularity. Milder myopathic changes are apparent in CHCHD10-WT (H) skeletal muscle with occasional central nuclei. Scale bars, 50 μm.

(G–N) Immunofluorescence of 14-month-old female CHCHD10-WT (H) and 15-month-old female CHCHD10-R15L (M) transgenic mouse quadriceps using antibodies targeting CHCHD10 and p62. Transgenic CHCHD10 protein expression is somewhat mosaic in appearance and often shares immunoreactivity with p62-positive inclusions. Scale bars, 25μm. (J, K) Muscle respirometry of permeabilized fibers from tibialis anterior (O) or soleus (P) from 7- to 8-month-old male mice (n = 3/group) demonstrating the oxygen consumption of the muscle fibers under sequential substrate, uncoupler, and inhibitor application conditions, as indicated. Data are represented as mean ± SEM. Unpaired t test, ns $p > 0.05$.

ejection fraction, fractional shortening, left ventricular mass, and stroke volume in the younger cohort (Figures 6A–6F, 6J, and 6K). Although limited in number, we carried out an echocardiography study of an older cohort of available mice (Figures 6G–6I, 6L, and 6M). Fourteen- to sixteen-month-old CHCHD10-R15L (H)

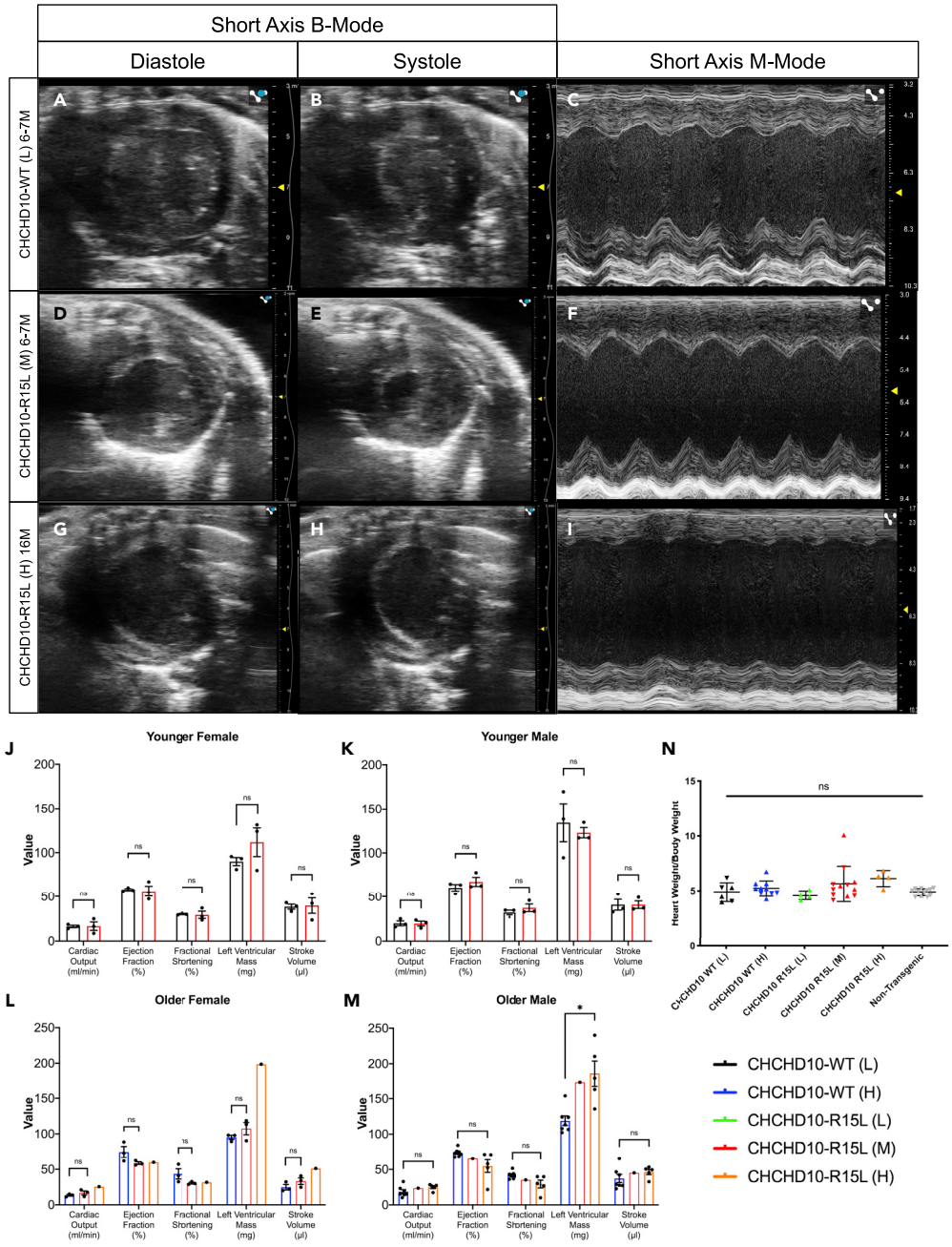

Figure 6. Echocardiography demonstrates transgene copy number and age-related decline in cardiac function

(A–C) Representative short axis echocardiography views from a 6-month-old male CHCHD10-WT (L) transgenic mouse.

(D–F) Representative short axis echocardiography views from a 7-month-old male CHCHD10-R15L (M) transgenic mouse.

(G–I) Representative short axis echocardiography views from a 16-month-old male CHCHD10-R15L (H) transgenic mouse.

(J) Echocardiography calculations derived from short axis M-Mode measurements of younger female mice. n = 3 6- to 7-month-old CHCHD10-WT (L) mice; n = 3 7- to 9-month-old CHCHD10-R15L (M) mice. Data are represented as mean ± SEM. Unpaired t test, ns $p > 0.05$.

(K) Echocardiography calculations derived from short axis M-Mode measurements of younger male mice. n = 3 6- to 7-month-old CHCHD10-WT (L) mice; n = 3 6- to 7-month-old CHCHD10-R15L (M) mice. Data are represented as mean ± SEM. Unpaired t test, ns $p > 0.05$.

(L) Echocardiography calculations derived from short axis M-Mode measurements of older female mice. n = 3 18-month-old CHCHD10-WT (H) mice; n = 3 18-month-old CHCHD10-R15L (M) mice; n = 1 15-month-old CHCHD10-R15L (H) mouse. Data are represented as mean ± SEM. Unpaired t test, ns $p > 0.05$.

Figure 6. *Continued*
(M) Echocardiography calculations derived from short axis M-Mode measurements of older male mice. n = 7 12- to 18-month-old CHCHD10-WT (H) mice; n = 1 15-month-old CHCHD10-R15L (M) mouse; n = 5 14- to 16-month-old CHCHD10-R15L (H) mice. Data are represented as mean ± SEM. Unpaired t test, ns $p > 0.05$, *$p < 0.05$.
(N) Mean heart weight:body weight ratio of indicated mouse lines. Upward facing triangles represent mice older than 12 months of age. Downward facing triangles represent mice younger than 12 months of age. Data are represented as mean ± SEM. One-way ANOVA with Tukey's multiple comparison test, ns $p > 0.05$.

mice displayed a statistically significant increased left ventricular mass compared with CHCHD10-WT (H) mice. Included in this study was a 16-month-old male CHCHD10-R15L (H) transgenic mouse that displayed an increased respiratory rate around the time of testing. This mouse had a reduced ejection fraction (22%) and fractional shortening (10%), severe ventricular hypokinesis (Figures 6G–6I), as well as an increased left ventricular mass (240mg) indicating a cardiomyopathy and cardiac failure. The mouse died 10 days later around the median age of death for this line. The onset of cardiac failure appears to be sudden as four other 14- to 16-month-old mice of the same gender and genotype did not display functional deficits as severe as the 16-month-old mouse. Furthermore, heart weight:body weight ratios were comparable across all lines, indicating that cardiac hypertrophy is not a factor at the ages measured (Figure 6N).

We also examined the cardiac pathology of the transgenic mouse lines. All CHCHD10-R15L transgenic lines display degenerating cardiomyocytes with CHCHD10-positive, p62-positive, and ubiquitin-positive accumulations (Figures 7A–7U). This pathology appears to be correlated with age and transgene copy number, similar to the previously described pathologies. A similar mild pathology is apparent in the CHCHD10-WT (H) mice. Unlike the CNS pathology, the possibility remains that transgenic protein overexpression is a causative factor giving rise to this pathology rather than the mutation, because it is apparent in the CHCHD10-WT (H) mice to a limited extent. The current data do not facilitate resolving these possibilities; nevertheless, the pathology and echocardiography data suggest that CHCHD10-R15L mice die suddenly from cardiac failure due to the degeneration of cardiomyocytes.

Chchd10 knockout mice

In order to address whether the pathology and deficits observed in CHCHD10-R15L transgenic mice occur as a result of a toxic gain- or loss-of-function, we analyzed mice lacking murine Chchd10 (Figures S12A–S12C). A cohort of Chchd10 homozygous knockout (KO) and control C57BL/6J mice was monitored for survival, body weight, and rotarod performance in a longitudinal study (Figure 8). Little difference was observed between the lines at any age tested. Furthermore, the axonal swelling pathology and cardiac pathology observed in the CHCHD10-R15L transgenic lines are absent from the Chchd10-KO mice (Figures S12D–S12G). A recent report describing Chchd10/Chchd2 double KO mice describes vacuolar pathology and abnormal mitochondrial cristae structure in the heart along with echocardiographic deficits resulting in early death of the mice (Liu et al., 2020b). The discordance between the single and double KO mice suggests Chchd2 compensates for the lack of Chchd10 in the single KO mice. The cardiac phenotype displays some similarity with the CHCHD10 transgenic mice; however, no CNS pathology was reported in the double KO mice. Although mutant CHCHD10 might act through a toxic gain-of-function mechanism in the heart, these data also raise the possibility that mutant CHCHD10 might act through a combination of loss of function of mutant CHCHD10 and a dominant negative mechanism of action on wild-type CHCHD10 and CHCHD2 to prevent compensation, resulting in a cardiac phenotype. CHCHD10 p.R15L appears to act through a toxic gain-of-function mechanism to give rise to the CNS pathology apparent in CHCHD10-R15L transgenic mice, because it is absent from CHCHD10-WT transgenic mice and Chchd10-KO mice and not reported in Chchd10/Chchd2 double KO mice.

In summary, CHCHD10-R15L transgenic mice display age- and copy-number-correlated pathologies of the CNS, skeletal muscle, and heart. These pathologies precede premature death and provide an insight into the mechanisms of disease at play in CHCHD10 p.R15L-ALS.

DISCUSSION

We report here the development of transgenic mouse models that provide useful tools to study the pathogenesis of CHCHD10 p.R15L-ALS. Mutations in *CHCHD10* have been identified in individuals suffering from distinct diseases of the nervous and muscular systems. This highlights the pleiotropic nature of *CHCHD10* in that it can impact upon distinct phenotypes. These transgenic mouse models support the

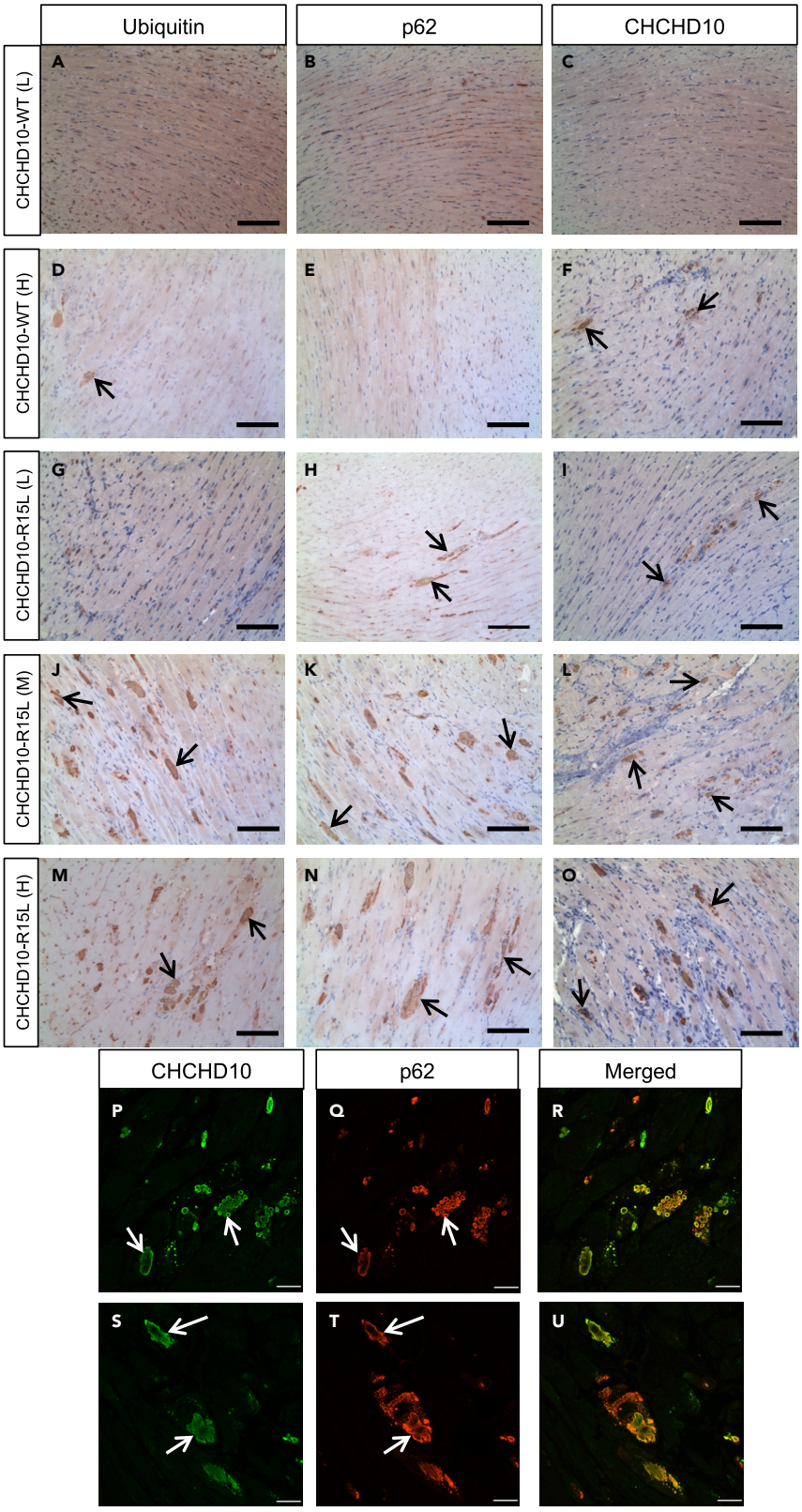
Ubiquitin
p62
CHCHD10
CHCHD10-WT (L)
CHCHD10-WT (H)
CHCHD10-R15L (L)
CHCHD10-R15L (M)
CHCHD10-R15L (H)
A
B
C
D
E
F
G
H
I
J
K
L
M
N
O
CHCHD10
p62
Merged
P
Q
R
S
T
U

Figure 7. Transgenic overexpression of CHCHD10 gives rise to CHCHD10-positive, p62-positive, ubiquitin-positive, protein accumulations in cardiac muscle

(A–C) A 25-month-old male CHCHD10-WT (L) transverse heart section stained using the indicated antibodies. Scale bars, 100 μm.

(D–F) A 20-month-old female CHCHD10-WT (H) transverse heart section stained using the indicated antibodies. Black arrows indicate examples of pathological protein accumulations. Scale bars, 100 μm.

(G–I) A 23-month-old female CHCHD10-R15L (L) transverse heart section stained using the indicated antibodies. Black arrows indicate examples of pathological protein accumulations. Scale bars, 100 μm.

(J–L) A 23-month-old male CHCHD10-R15L (M) transverse heart section stained using the indicated antibodies. Black arrows indicate examples of pathological protein accumulations. Scale bars, 100 μm.

(M–O) A 12-month-old male CHCHD10-R15L (H) transverse heart section stained using the indicated antibodies. Black arrows indicate examples of pathological protein accumulations. Scale bars, 100 μm.

(P–U) Immunofluorescence of a 23-month-old CHCHD10-R15L (M) transgenic mouse heart using antibodies targeting CHCHD10 and p62 demonstrating pathological protein inclusions (white arrows). Scale bars, 25 μm.

hypothesis that *CHCHD10* is a pleiotropic gene and suggest that a combination of tissue-specific pathologies may act in concert to cause disease in CHCHD10 p.R15L-ALS.

One must be cautious in interpreting data from transgenic mouse models due to confounding factors related to overexpression, position effects, and variable expression levels across models. In addition to these confounding factors, animal models may have limitations due to species differences and their short lifespan, which is particularly relevant to late-onset neurodegenerative disease. We took the approach of developing these models because transgenic overexpression of mutant genes that cause late-onset disorders is typically employed to exaggerate the toxicity of the mutant protein and thus compensate for the short lifespan of the model. The shared pathological phenotypes across multiple independent lines suggests position effects are not a major concern. We are mindful of the impact and potential confounding of transgene overexpression. It is for this reason that we established and characterized five independent transgenic mouse lines, as described. We screened 66 potential CHCHD10-WT founder mice generated over two rounds of microinjections in order to obtain a line with comparable levels of expression to the CHCHD10-R15L lines that have a range of transgene expression levels. Given the limitations of the technology in that we could not control levels of transgene expression with exquisite precision, we proceeded with the best available lines. A recent report describes the development of a transgenic mouse model expressing FLAG-tagged CHCHD10 under the control of the CNS-enriched *Prp* promoter (Liu et al., 2020a). FLAG-tagged CHCHD10-R15L transgenic mice display one-half the transgene expression level of the FLAG-tagged CHCHD10-WT control mice, again highlighting the inherent difficulties of obtaining transgenic mice with comparable transgene expression levels. The authors describe a disruption of the interaction between CHCHD10, Opa1, and mitofilin, a component of the MICOS system, in the mutant mice. No behavioral, pathological, or survival data are described, making it difficult to compare the models.

The FLAG-tagged CHCHD10 transgenic mouse model contrasts with the transgenic mouse models we describe in that we did not restrict expression to a particular cell type or tissue. The transgene design, incorporating the entire human *CHCHD10* gene and endogenous upstream promoter, has several favorable features. Use of the endogenous promoter allows for analysis of the impact of expression on the organism as a whole, without restriction to a specific cell type or tissue, thus providing a means of discerning the pleiotropic properties of CHCHD10. Furthermore, the availability of the human gene sequence in a mouse model provides a means to perform preclinical studies targeting the human sequence *in vivo*, an approach undertaken leading to ongoing investigations related to SOD1-ALS therapeutic development (Mccampbell et al., 2018; Borel et al., 2016).

ALS is a genetically, clinically, and pathologically complex disease. With the discovery of mutations in genes such as *SQSTM1*, *C9orf72*, *VCP*, *HNRNPA1*, and *HNRNPA2/B1* in ALS patients (Fecto et al., 2011; Dejesus-Hernandez et al., 2011; Renton et al., 2011; Johnson et al., 2010; Kim et al., 2013), it has come to be recognized that ALS can fall within a spectrum of clinical presentations. These genes can also be mutated in patients suffering from the individual diseases or various combinations of frontotemporal dementia, myopathy, and/or Paget disease of bone (Dejesus-Hernandez et al., 2011; Renton et al., 2011; Kim et al., 2013; Watts et al., 2004). A spectrum of ALS pathologies has also become apparent with the identification of causative gene mutations. For example, *SOD1*-FALS cases are not typically observed to harbor FUS, TDP-43, or OPTN-positive protein inclusions, as is the case for many sporadic ALS and

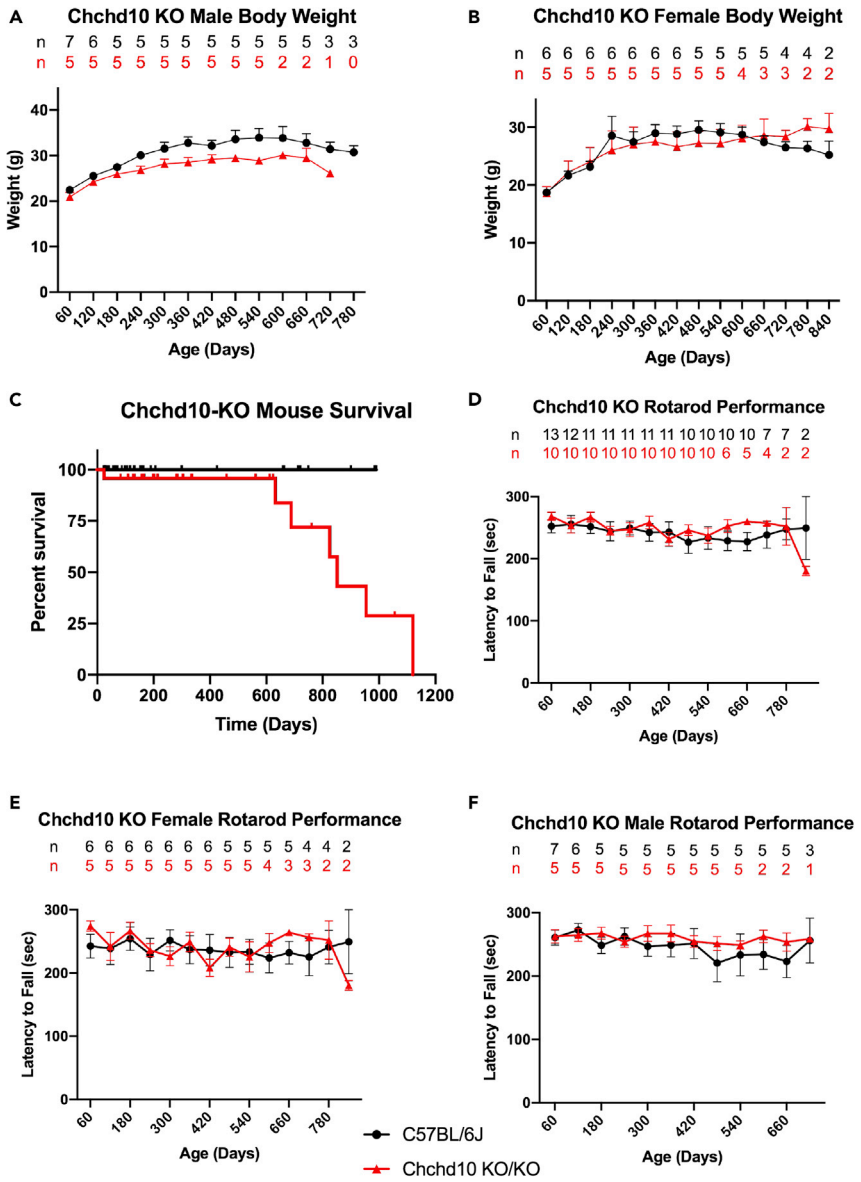

Figure 8. Chchd10-KO mouse behavioral testing

(A) Male mouse body weight measurements. Mouse body weight was measured every 60 days beginning at 60 days of age. The overlying numbers indicate the number of mice from each line used to calculate mean body weights at each time point. Data are represented as mean ± SEM. Two-way ANOVA with Holm-Šidák post hoc statistical analysis summarized in Tables S35–S36.

(B) Female mouse body weight measurements. Mouse body weight was measured every 60 days beginning at 60 days of age. The overlying numbers indicate the number of mice from each line used to calculate mean body weights at each time point. Data are represented as mean ± SEM. two-way ANOVA with Holm-Šidák post hoc statistical analysis summarized in Tables S37–S38.

(C) Kaplan-Meier survival analysis of Chchd10-KO mice compared with C57BL/6J mice. Death of a mouse for unknown reasons is considered a death event, as indicated by a drop in the line. Mice still living or death of a mouse due to intervention by the investigators are considered censored events, as indicated by tick marks along a line. Median survival for Chchd10-KO mice is 851 days, n = 8 death events and n = 40 censored events. Median survival for C57BL/6J mice is undefined, n = 0 death events and n = 94 censored events. Gehan-Breslow-Wilcoxon test, p = 0.0107.

(D) Mouse rotarod performance. Mice were tested on an accelerating rotarod task every 60 days beginning at 60 days of age. The overlying numbers indicate the number of mice from each line used to calculate mean latency to fall at each time point. Data are represented as mean ± SEM. Two-way ANOVA with Holm-Šidák post hoc statistical analysis summarized in Tables S39–S40.

Figure 8. *Continued*

(E) Female mouse rotarod performance. Mice were tested on an accelerating rotarod task every 60 days beginning at 60 days of age. The overlying numbers indicate the number of mice from each line used to calculate mean latency to fall at each time point. Data are represented as mean ± SEM. Two-way ANOVA with Holm-Šidák post hoc statistical analysis summarized in Tables S41–S42.

(F) Male mouse rotarod performance. Mice were tested on an accelerating rotarod task every 60 days beginning at 60 days of age. The overlying numbers indicate the number of mice from each line used to calculate mean latency to fall at each time point. Data are represented as mean ± SEM. Two-way ANOVA with Holm-Šidák post hoc statistical analysis summarized in Tables S43–S44.

non-*SOD1*-FALS cases (Deng et al., 2010, 2011; Tan et al., 2007; Mackenzie et al., 2007). Despite the pathological diversity, these cases may be clinically indistinguishable. It is with this in mind that we observe an array of striking pathologies of the CNS, skeletal muscle, and heart in CHCHD10-R15L transgenic mice. Although these pathologies may not be recognized as a component of the typical pathological profile of ALS, they may be relevant to CHCHD10-ALS.

A recent description of the human pathology of CHCHD10 p.R15L-ALS describes anterior horn neuronal CHCHD10-positive, TDP-43-negative protein aggregates (Keith et al., 2020). Such aggregates are not apparent in the CHCHD10-R15L transgenic mice, but p62-positive, TDP-43-negative punctate staining is apparent in the spinal cord, indicating that the mice display some deficit in CNS protein degradation. Although axonal swelling, as observed in the CHCHD10-R15L transgenic mice, is not described in the human case, such pathology may not be readily observed due to species differences, limitations of detection, or prior loss of pathological axons.

By virtue of the presence of a coiled-coil-helix-coiled-coil-helix domain in CHCHD10, and the involvement of such a domain in the disulfide relay system to maintain proteins within the mitochondrial intermembrane space (Herrmann and Riemer, 2012; Modjtahedi et al., 2016), CHCHD10 is understood to be a mitochondrial protein. Work from a number of research groups have demonstrated CHCHD10 localization to mitochondria (Bannwarth et al., 2014; Ajroud-Driss et al., 2015; Huang et al., 2018; Burstein et al., 2018; Straub et al., 2018; Woo et al., 2017), as well as to the nucleus (Purandare et al., 2018). CHCHD10 is highly expressed in skeletal muscle and the heart, tissues known to have a relatively large mitochondrial population. Using the endogenous *CHCHD10* promoter in our transgenic models, we did not restrict expression and subsequently detected severe pathologies of tissues where CHCHD10 is known to be abundant, i.e. skeletal muscle and heart, as well as in subpopulations of CNS neurons.

The CNS pathology is characterized by large axonal swellings that can occur in isolation or in sequence along an axon. The CNS pathology is apparent in all three CHCHD10-R15L transgenic lines, regardless of transgene copy number and never observed in either CHCHD10-WT transgenic line. This provides evidence that it arises due to the mutation and not as a result of transgene overexpression. A similar CNS pathology has been described in other transgenic mouse models related to ALS expressing both wild-type SOD1 and SOD1 p.G93A (Dal Canto and Gurney, 1997; Wong et al., 1995; Jaarsma et al., 2000, 2001; Tu et al., 1996). These models demonstrate mitochondrial vacuolation leading to swellings in axons of diverse CNS neurons akin to what we observe in CHCHD10-R15L transgenic mice. It is also noted that these swellings do not necessarily lead to neuronal death in SOD1-WT transgenic mice, as also appears to be the case in CHCHD10-R15L mice given that they survive many months, even years, after the first presentation of the pathological swellings. Given that neurons harboring swellings do not appear to degenerate, the possibility arises that such swellings might be protective against unrecognized pathogenic mechanisms or the life span of the mouse is not sufficiently long for the pathology to manifest as clinical disease.

The immunohistochemical profile visualized in the CNS when using antibodies targeting CHCHD10 is surprising in CHCHD10-R15L transgenic mice. Immunoreactivity is not obviously mitochondrial or nuclear but apparent in the pathological swellings and long stretches of axonal processes. The observation of this immunohistochemical profile with all independent antibodies used and lack of staining in Chchd10-KO mice indicates that this is an accurate representation of transgenic CHCHD10 protein localization. Focal components of the swellings that are strongly immunoreactive with CHCHD10 antibodies also display immunoreactivity with antibodies targeting mitochondrial proteins. This suggests that compromised

mitochondria contribute to the formation of these swellings. Indeed, profiles of swollen mitochondria with distended cristae, likely to be in an intermediate pathological stage leading toward this eventuality, are apparent (Figure S6F). Although pathological, these swellings do not appear to compromise cell viability, with indirect evidence provided by equivalent numbers and caliber distribution of femoral nerve motor branch axons. This highlights the resilience of neuronal systems to severe pathology, an underappreciated aspect of neuropathology. The mechanisms at play in driving the formation of the swellings remain to be fully determined. Plausible possibilities include deficits of mitochondrial dynamics, and our examination of mitochondrial transport in axons of primary neurons of CHCHD10-R15L (M) mice suggest mitochondrial trafficking abnormalities might contribute.

Given the severity of the CNS pathology including of motor system neurons, it is remarkable that CHCHD10-R15L transgenic mice perform, comparably to controls, in motor behavioral tests for the vast majority of life. Because the pathology is first apparent around 60 days of age in CHCHD10-R15L (M) mice, but they do not display any motor behavior deficit for approximately another 18 months, it is evident that emergence of pathology does not strictly correlate with manifestation of disease and raises the question as to when does CNS pathology become disease. The observation of pathology without a clinical disease phenotype can be a feature of human neurodegenerative disease. We note a report of an individual with a *C9orf72* hexanucleotide repeat expansion mutation who underwent temporal lobe resection for epilepsy five years before the onset of FTD (Vatsavayai et al., 2016). The resected tissue harbored RNA foci, dipeptide repeat protein inclusions, and loss of nuclear TDP-43 but lacked TDP-43-positive protein inclusions. Upon postmortem examination 8 years after FTD symptom onset, abundant TDP-43 protein inclusions were detected. This case highlights the evolution of pathology that may progress for many years without disease manifestation, before the burden ultimately cannot be tolerated.

Due to the fact that the CHCHD10-R15L transgenic mice live for a relatively long time and die unexpectedly, it is difficult to attribute a precise cause of death. In examining the skeletal muscle and cardiac pathology of these mice, we observed further striking pathology characterized by protein inclusions comprising CHCHD10, p62, and/or ubiquitin. Of note, CHCHD10-WT (H) transgenic mice display a similar, but much milder, muscle pathology indicating that overexpression of transgenic human CHCHD10 protein can result in abnormal protein inclusions in muscle. Mutant CHCHD10 exacerbates the disruption to the myofibrillar network that will disturb normal function over time and likely contributes to premature death of CHCHD10-R15L transgenic mice alongside pathological CNS axonal swellings. Obvious degeneration of cardiomyocytes with protein inclusions are apparent in CHCHD10-R15L (M) and CHCHD10-R15L (H) mice that may contribute to cardiac failure later in life. Indeed, echocardiographic analysis of an older cohort of mice revealed severe functional deficits in a 16-month-old CHCHD10-R15L (H) mouse 10 days prior to death. The wide time frame of age of death made it difficult to capture this in other mice of the same genotype and revealed the onset of echocardiographic deficits to be abrupt. Cardiac dysfunction has been reported in ALS patients and sometimes attributed as a cause of death (Rosenbohm et al., 2017). Cardiac dysfunction has also been reported in mouse models of a distinct motor neuron disease, spinal muscular atrophy (Heier et al., 2010; Shababi et al., 2010). This provides further evidence that comorbidity of motor neuron disease and cardiac dysfunction may be relevant to disease course and phenotype. Our data warrant consideration to cardiac dysfunction being given to patients with a CHCHD10 p.R15L mutation. Additional evidence that mutant CHCHD10 impacts upon multiple tissues is provided by three independently reported knock-in mouse models of the CHCHD10 p.S59L mutation (Anderson et al., 2019; Genin et al., 2019; Liu et al., 2020b). This mutation was identified in patients with complex and varying phenotypes including myopathy, ataxia, cognitive impairment, motor neuron disease, and deafness, as well as a singleton ALS-FTD case (Bannwarth et al., 2014). The knock-in mouse models report pathology of the nervous system, skeletal muscle, and heart. Although the pathology we describe in our CHCHD10-R15L transgenic mouse models is unique, the common involvement of these three systems across different mouse models highlights the importance of CHCHD10 in those systems.

Longitudinal study of the behavior and pathology of Chchd10-KO mice was unremarkable. This is largely consistent with a previous report using a different global knockout strategy, which identified a mild ADP-stimulated respiration deficiency in skeletal muscle mitochondria as well as electron dense structures of unknown origin in the heart (Burstein et al., 2018). A conditional skeletal muscle Chchd10-KO mouse model has also been studied and displays some mild motor deficits, along with neuromuscular junction structural and electrophysiological deficits (Xiao et al., 2019). Combined with a lack of pathology or behavioral

phenotype in Chchd10-KO mice, the data presented initially suggested a toxic gain-of-function of CHCHD10 p.R15L in CNS, skeletal muscle, and heart resulting in severe pathology causing premature death in a copy-number correlated fashion. The recent report of Chchd10/Chchd2 double KO mice displaying a cardiac phenotype brings forth the possibility that mutant CHCHD10 might act through a toxic gain-of-function or a combination of loss-of-function of mutant CHCHD10 and a dominant negative mechanism of action on wild-type CHCHD10 and CHCHD2 to prevent compensation in the heart. This is distinct from the CNS pathology, which appears to arise as result of a toxic gain-of-function of CHCHD10 p.R15L, as it is absent from CHCHD10-WT transgenic mice and Chchd10-KO mice and not reported in Chchd10/Chchd2 double KO mice.

In conclusion, we present here transgenic mouse models that provide a valuable preclinical resource that can be used to interrogate mechanisms of CHCHD10 p.R15L-ALS. Our work underlines genetic pleiotropy as an important consideration in disease causation, as it greatly expands the clinical pathology to systems previously excluded from consideration in the natural history of diseases such as ALS.

Limitations of the study

Limitations of the technology prevented precise regulation of the level of expression of the transgene. We sought to address this limitation by developing and characterizing five independent transgenic mouse lines. Although the CHCHD10-WT lines do not exhibit precisely matched transgene expression levels to the CHCHD10-R15L (M) and CHCHD10-R15L (H) lines, these mouse models remain a valuable preclinical resource displaying numerous striking pathologies. It is possible that some aspects of the phenotype of these models arise due to transgene overexpression, rather than the mutation, or a combination of both. Importantly, although the severity of the CNS pathology positively correlates with transgene expression level, the data indicate that it arises due to the mutation because it is present in all three CHCHD10-R15L lines and absent from the CHCHD10-WT (H) line that has a higher transgene expression level than the CHCHD10-R15L (L) line.

Resource availability

Lead contact

Further information and requests for resources and reagents should be directed to and will be fulfilled by the Lead Contact, Teepu Siddique (t-siddique@northwestern.edu).

Materials availability

All unique/stable reagents generated in this study are available from the Lead Contact with a completed Materials Transfer Agreement.

Data and code availability

The published article includes all datasets generated or analyzed during this study.

METHODS

All methods can be found in the accompanying Transparent Methods supplemental file.

SUPPLEMENTAL INFORMATION

Supplemental information can be found online at https://doi.org/10.1016/j.isci.2021.102061.

ACKNOWLEDGMENTS

This study was supported by the National Institute of Neurological Disorders and Stroke (NS099638), the Foglia Family Foundation, the Les Turner ALS Foundation, and the Les Turner ALS Foundation/Herbert C. Wenske Foundation Professorship. The genetically engineered mice were generated with the assistance of the Northwestern University Transgenic and Targeted Mutagenesis Laboratory, which is partially supported by NIH grant CA60553 to the Robert H. Lurie Comprehensive Cancer Center. Open Field and DigiGait testing of mice was performed at the Northwestern University Behavioral Phenotyping Core Facility. Tissue embedding work was supported by the Northwestern University Pathology Core Facility and a Cancer Center Support Grant (NCI CA060553). Confocal and electron microscopy imaging was performed at the Northwestern University Center for Advanced Microscopy generously supported by NCI

CCSG P30 CA060553 awarded to the Robert H Lurie Comprehensive Cancer Center. Echocardiography research was supported by George M. O'Brien Kidney Research Core Center (NU GoKidney), which is generously supported by the award P30 DK114857 from the National Institute of Diabetes and Digestive and Kidney Diseases, within the National Institutes of Health. We thank Dr. Erdong Liu, Ms Hong Zhai, and Ms Michele Hadhazy for technical assistance. We thank Dr. Jon Lomasney and Dr. Alexis Demonbreun for assistance with data analysis.

AUTHOR CONTRIBUTIONS

Conceptualization, É.B.R., Y.C.M, H-X.D., and T.S.; Methodology, É.B.R., J.Y., N.M., S.D., Y.C.M., H-X.D., and T.S.; Investigation, É.B.R., J.Y., S.D., and Y.C.M; Resources, S.D., Y.C.M., and T.S.; Writing—Original Draft, É.B.R., Writing—Review and Editing, É.B.R., J.Y., S.D., Y.C.M, H-X.D., and T.S.; Supervision, T.S.; Funding Acquisition, T.S.

DECLARATION OF INTERESTS

The authors declare no competing interests.

Received: November 19, 2019
Revised: August 27, 2020
Accepted: January 12, 2021
Published: February 19, 2021

REFERENCES

Ajroud-Driss, S., Fecto, F., Ajroud, K., Lalani, I., Calvo, S.E., Mootha, V.K., Deng, H.X., Siddique, N., Tahmoush, A.J., Heiman-Patterson, T.D., and Siddique, T. (2015). Mutation in the novel nuclear-encoded mitochondrial protein CHCHD10 in a family with autosomal dominant mitochondrial myopathy. Neurogenetics *16*, 1–9.

An, J., Shi, J., He, Q., Lui, K., Liu, Y., Huang, Y., and Sheikh, M.S. (2012). CHCM1/CHCHD6, novel mitochondrial protein linked to regulation of mitofilin and mitochondrial cristae morphology. J. Biol. Chem. *287*, 7411–7426.

Anderson, C.J., Bredvik, K., Burstein, S.R., Davis, C., Meadows, S.M., Dash, J., Case, L., Milner, T.A., Kawamata, H., Zuberi, A., et al. (2019). ALS/FTD mutant CHCHD10 mice reveal a tissue-specific toxic gain-of-function and mitochondrial stress response. Acta Neuropathol. *138*, 103–121.

Aras, S., Bai, M., Lee, I., Springett, R., Huttemann, M., and Grossman, L.I. (2015). MNRR1 (formerly CHCHD2) is a bi-organellar regulator of mitochondrial metabolism. Mitochondrion *20*, 43–51.

Auranen, M., Ylikallio, E., Shcherbii, M., Paetau, A., Kiuru-Enari, S., Toppila, J.P., and Tyynismaa, H. (2015). CHCHD10 variant p.(Gly66Val) causes axonal Charcot-Marie-Tooth disease. Neurol. Genet. *1*, e1.

Bannwarth, S., Ait-El-Mkadem, S., Chaussenot, A., Genin, E.C., Lacas-Gervais, S., Fragaki, K., Berg-Alonso, L., Kageyama, Y., Serre, V., Moore, D.G., et al. (2014). A mitochondrial origin for frontotemporal dementia and amyotrophic lateral sclerosis through CHCHD10 involvement. Brain *137*, 2329–2345.

Borel, F., Gernoux, G., Cardozo, B., Metterville, J.P., Toro Cabrera, G.C., Song, L., Su, Q., Gao, G.P., Elmallah, M.K., Brown, R.H., Jr., and Mueller, C. (2016). Therapeutic rAAVrh10 mediated SOD1 silencing in adult SOD1(G93A) mice and nonhuman primates. Hum. Gene Ther. *27*, 19–31.

Brockmann, S.J., Freischmidt, A., Oeckl, P., Muller, K., Ponna, S.K., Helferich, A.M., Paone, C., Reinders, J., Kojer, K., Orth, M., et al. (2018). CHCHD10 mutations p.R15L and p.G66V cause motoneuron disease by haploinsufficiency. Hum. Mol. Genet. *27*, 706–715.

Brown, R.H., and Al-Chalabi, A. (2017). Amyotrophic lateral sclerosis. N. Engl. J. Med. *377*, 162–172.

Burstein, S.R., Valsecchi, F., Kawamata, H., Bourens, M., Zeng, R., Zuberi, A., Milner, T.A., Cloonan, S.M., Lutz, C., Barrientos, A., and Manfredi, G. (2018). In vitro and in vivo studies of the ALS-FTLD protein CHCHD10 reveal novel mitochondrial topology and protein interactions. Hum. Mol. Genet. *27*, 160–177.

Dal Canto, M.C., and Gurney, M.E. (1997). A low expressor line of transgenic mice carrying a mutant human Cu,Zn superoxide dismutase (SOD1) gene develops pathological changes that most closely resemble those in human amyotrophic lateral sclerosis. Acta Neuropathol. *93*, 537–550.

Darshi, M., Trinh, K.N., Murphy, A.N., and Taylor, S.S. (2012). Targeting and import mechanism of coiled-coil helix coiled-coil helix domain-containing protein 3 (ChChd3) into the mitochondrial intermembrane space. J. Biol. Chem. *287*, 39480–39491.

Dejesus-Hernandez, M., Mackenzie, I.R., Boeve, B.F., Boxer, A.L., Baker, M., Rutherford, N.J., Nicholson, A.M., Finch, N.A., Flynn, H., Adamson, J., et al. (2011). Expanded GGGGCC hexanucleotide repeat in noncoding region of C9ORF72 causes chromosome 9p-linked FTD and ALS. Neuron *72*, 245–256.

Deng, H.X., Bigio, E.H., Zhai, H., Fecto, F., Ajroud, K., Shi, Y., Yan, J., Mishra, M., Ajroud-Driss, S., Heller, S., et al. (2011). Differential involvement of optineurin in amyotrophic lateral sclerosis with or without SOD1 mutations. Arch. Neurol. *68*, 1057–1061.

Deng, H.X., Zhai, H., Bigio, E.H., Yan, J., Fecto, F., Ajroud, K., Mishra, M., Ajroud-Driss, S., Heller, S., Sufit, R., et al. (2010). FUS-immunoreactive inclusions are a common feature in sporadic and non-SOD1 familial amyotrophic lateral sclerosis. Ann. Neurol. *67*, 739–748.

Fecto, F., Yan, J., Vemula, S.P., Liu, E., Yang, Y., Chen, W., Zheng, J.G., Shi, Y., Siddique, N., Arrat, H., et al. (2011). SQSTM1 mutations in familial and sporadic amyotrophic lateral sclerosis. Arch. Neurol. *68*, 1440–1446.

Fischer, M., and Riemer, J. (2013). The mitochondrial disulfide relay system: roles in oxidative protein folding and beyond. Int. J. Cell Biol. *2013*, 742923.

Funayama, M., Ohe, K., Amo, T., Furuya, N., Yamaguchi, J., Saiki, S., Li, Y., Ogaki, K., Ando, M., Yoshino, H., et al. (2015). CHCHD2 mutations in autosomal dominant late-onset Parkinson's disease: a genome-wide linkage and sequencing study. Lancet Neurol. *14*, 274–282.

Genin, E.C., Madji Hounoum, B., Bannwarth, S., Fragaki, K., Lacas-Gervais, S., Mauri-Crouzet, A., Lespinasse, F., Neveu, J., Ropert, B., Auge, G., et al. (2019). Mitochondrial defect in muscle precedes neuromuscular junction degeneration and motor neuron death in CHCHD10(S59L/+) mouse. Acta Neuropathol. *138*, 123–145.

Genin, E.C., Plutino, M., Bannwarth, S., Villa, E., Cisneros-Barroso, E., Roy, M., Ortega-Vila, B., Fragaki, K., Lespinasse, F., Pinero-Martos, E., et al. (2016). CHCHD10 mutations promote loss of mitochondrial cristae junctions with impaired mitochondrial genome maintenance and

inhibition of apoptosis. EMBO Mol. Med. *8*, 58–72.

Heier, C.R., Satta, R., Lutz, C., and Didonato, C.J. (2010). Arrhythmia and cardiac defects are a feature of spinal muscular atrophy model mice. Hum. Mol. Genet. *19*, 3906–3918.

Herrmann, J.M., and Riemer, J. (2012). Mitochondrial disulfide relay: redox-regulated protein import into the intermembrane space. J. Biol. Chem. *287*, 4426–4433.

Huang, X., Wu, B.P., Nguyen, D., Liu, Y.T., Marani, M., Hench, J., Benit, P., Kozjak-Pavlovic, V., Rustin, P., Frank, S., and Narendra, D.P. (2018). CHCHD2 accumulates in distressed mitochondria and facilitates oligomerization of CHCHD10. Hum. Mol. Genet. *27*, 3881–3900.

Jaarsma, D., Haasdijk, E.D., Grashorn, J.A., Hawkins, R., Van Duijn, W., Verspaget, H.W., London, J., and Holstege, J.C. (2000). Human Cu/Zn superoxide dismutase (SOD1) overexpression in mice causes mitochondrial vacuolization, axonal degeneration, and premature motoneuron death and accelerates motoneuron disease in mice expressing a familial amyotrophic lateral sclerosis mutant SOD1. Neurobiol. Dis. *7*, 623–643.

Jaarsma, D., Rognoni, F., Van Duijn, W., Verspaget, H.W., Haasdijk, E.D., and Holstege, J.C. (2001). CuZn superoxide dismutase (SOD1) accumulates in vacuolated mitochondria in transgenic mice expressing amyotrophic lateral sclerosis-linked SOD1 mutations. Acta Neuropathol. *102*, 293–305.

Jiao, B., Xiao, T., Hou, L., Gu, X., Zhou, Y., Zhou, L., Tang, B., Xu, J., and Shen, L. (2016). High prevalence of CHCHD10 mutation in patients with frontotemporal dementia from China. Brain *139*, e21.

Johnson, J.O., Glynn, S.M., Gibbs, J.R., Nalls, M.A., Sabatelli, M., Restagno, G., Drory, V.E., Chio, A., Rogaeva, E., and Traynor, B.J. (2014). Mutations in the CHCHD10 gene are a common cause of familial amyotrophic lateral sclerosis. Brain *137*, e311.

Johnson, J.O., Mandrioli, J., Benatar, M., Abramzon, Y., Van Deerlin, V.M., Trojanowski, J.Q., Gibbs, J.R., Brunetti, M., Gronka, S., Wuu, J., et al. (2010). Exome sequencing reveals VCP mutations as a cause of familial ALS. Neuron *68*, 857–864.

Keith, J.L., Swinkin, E., Gao, A., Alminawi, S., Zhang, M., Mcgoldrick, P., Mckeever, P., Robertson, J., Rogaeva, E., and Zinman, L. (2020). Neuropathologic description of CHCHD10 mutated amyotrophic lateral sclerosis. Neurol. Genet. *6*, e394.

Kim, H.J., Kim, N.C., Wang, Y.D., Scarborough, E.A., Moore, J., Diaz, Z., Maclea, K.S., Freibaum, B., Li, S., Molliex, A., et al. (2013). Mutations in prion-like domains in hnRNPA2B1 and hnRNPA1 cause multisystem proteinopathy and ALS. Nature *495*, 467–473.

Kurzwelly, D., Kruger, S., Biskup, S., and Heneka, M.T. (2015). A distinct clinical phenotype in a German kindred with motor neuron disease carrying a CHCHD10 mutation. Brain *138*, e376.

Kwiatkowski, T.J., Bosco, D.A., Leclerc, A.L., Tamrazian, E., Vanderburg, C.R., Russ, C., Davis, A., Gilchrist, J., Kasarskis, E.J., Munsat, T., et al. (2009). Mutations in the FUS/TLS gene on chromosome 16 cause familial amyotrophic lateral sclerosis. Science *323*, 1205–1208.

Lehmer, C., Schludi, M.H., Ransom, L., Greiling, J., Junghanel, M., Exner, N., Riemenschneider, H., Van Der Zee, J., Van Broeckhoven, C., Weydt, P., et al. (2018). A novel CHCHD10 mutation implicates a Mia40-dependent mitochondrial import deficit in ALS. EMBO Mol. Med. *10*, e8558.

Liu, T., Woo, J.A., Bukhari, M.Z., Lepochat, P., Chacko, A., Selenica, M.B., Yan, Y., Kotsiviras, P., Buosi, S.C., Zhao, X., and Kang, D.E. (2020a). CHCHD10-regulated OPA1-mitofilin complex mediates TDP-43-induced mitochondrial phenotypes associated with frontotemporal dementia. FASEB J. *34*, 8493–8509.

Liu, Y.T., Huang, X., Nguyen, D., Shammas, M.K., Wu, B.P., Dombi, E., Springer, D.A., Poulton, J., Sekine, S., and Narendra, D.P. (2020b). Loss of CHCHD2 and CHCHD10 activates OMA1 peptidase to disrupt mitochondrial cristae phenocopying patient mutations. Hum. Mol. Genet. *29*, 1547–1567.

Mackenzie, I.R., Bigio, E.H., Ince, P.G., Geser, F., Neumann, M., Cairns, N.J., Kwong, L.K., Forman, M.S., Ravits, J., Stewart, H., et al. (2007). Pathological TDP-43 distinguishes sporadic amyotrophic lateral sclerosis from amyotrophic lateral sclerosis with SOD1 mutations. Ann. Neurol. *61*, 427–434.

Mccampbell, A., Cole, T., Wegener, A.J., Tomassy, G.S., Setnicka, A., Farley, B.J., Schoch, K.M., Hoye, M.L., Shabsovich, M., Sun, L., et al. (2018). Antisense oligonucleotides extend survival and reverse decrement in muscle response in ALS models. J. Clin. Invest. *128*, 3558–3567.

Meng, H., Yamashita, C., Shiba-Fukushima, K., Inoshita, T., Funayama, M., Sato, S., Hatta, T., Natsume, T., Umitsu, M., Takagi, J., et al. (2017). Loss of Parkinson's disease-associated protein CHCHD2 affects mitochondrial crista structure and destabilizes cytochrome c. Nat. Commun. *8*, 15500.

Modjtahedi, N., Tokatlidis, K., Dessen, P., and Kroemer, G. (2016). Mitochondrial proteins containing coiled-coil-helix-coiled-coil-helix (CHCH) domains in health and disease. Trends Biochem. Sci. *41*, 245–260.

Muller, K., Andersen, P.M., Hubers, A., Marroquin, N., Volk, A.E., Danzer, K.M., Meitinger, T., Ludolph, A.C., Strom, T.M., and Weishaupt, J.H. (2014). Two novel mutations in conserved codons indicate that CHCHD10 is a gene associated with motor neuron disease. Brain *137*, e309.

Ott, C., Dorsch, E., Fraunholz, M., Straub, S., and Kozjak-Pavlovic, V. (2015). Detailed analysis of the human mitochondrial contact site complex indicate a hierarchy of subunits. PLoS One *10*, e0120213.

Penttila, S., Jokela, M., Bouquin, H., Saukkonen, A.M., Toivanen, J., and Udd, B. (2015). Late onset spinal motor neuronopathy is caused by mutation in CHCHD10. Ann. Neurol. *77*, 163–172.

Project Mine Als Sequencing Consortium (2018). CHCHD10 variants in amyotrophic lateral sclerosis: where is the evidence? Ann. Neurol. *84*, 110–116.

Purandare, N., Somayajulu, M., Huttemann, M., Grossman, L.I., and Aras, S. (2018). The cellular stress proteins CHCHD10 and MNRR1 (CHCHD2): partners in mitochondrial and nuclear function and dysfunction. J. Biol. Chem. *293*, 6517–6529.

Renton, A.E., Majounie, E., Waite, A., Simon-Sanchez, J., Rollinson, S., Gibbs, J.R., Schymick, J.C., Laaksovirta, H., Van Swieten, J.C., Myllykangas, L., et al. (2011). A hexanucleotide repeat expansion in C9ORF72 is the cause of chromosome 9p21-linked ALS-FTD. Neuron *72*, 257–268.

Riemer, J., Fischer, M., and Herrmann, J.M. (2011). Oxidation-driven protein import into mitochondria: insights and blind spots. Biochim. Biophys. Acta *1808*, 981–989.

Rosen, D.R., Siddique, T., Patterson, D., Figlewicz, D.A., Sapp, P., Hentati, A., Donaldson, D., Goto, J., Oregan, J.P., Deng, H.X., et al. (1993). Mutations in Cu/Zn superoxide-dismutase gene are associated with familial amyotrophic-lateral-sclerosis. Nature *362*, 59–62.

Rosenbohm, A., Schmid, B., Buckert, D., Rottbauer, W., Kassubek, J., Ludolph, A.C., and Bernhardt, P. (2017). Cardiac findings in amyotrophic lateral sclerosis: a magnetic resonance imaging study. Front. Neurol. *8*, 479.

Seibenhener, M.L., and Wooten, M.C. (2015). Use of the Open Field Maze to measure locomotor and anxiety-like behavior in mice. J. Vis. Exp. e52434.

Shababi, M., Habibi, J., Yang, H.T., Vale, S.M., Sewell, W.A., and Lorson, C.L. (2010). Cardiac defects contribute to the pathology of spinal muscular atrophy models. Hum. Mol. Genet. *19*, 4059–4071.

Simon, P., Dupuis, R., and Costentin, J. (1994). Thigmotaxis as an index of anxiety in mice. Influence of dopaminergic transmissions. Behav. Brain Res. *61*, 59–64.

Straub, I.R., Janer, A., Weraarpachai, W., Zinman, L., Robertson, J., Rogaeva, E., and Shoubridge, E.A. (2018). Loss of CHCHD10-CHCHD2 complexes required for respiration underlies the pathogenicity of a CHCHD10 mutation in ALS. Hum. Mol. Genet. *27*, 178–189.

Tan, C.F., Eguchi, H., Tagawa, A., Onodera, O., Iwasaki, T., Tsujino, A., Nishizawa, M., Kakita, A., and Takahashi, H. (2007). TDP-43 immunoreactivity in neuronal inclusions in familial amyotrophic lateral sclerosis with or without SOD1 gene mutation. Acta Neuropathol. *113*, 535–542.

Tu, P.H., Raju, P., Robinson, K.A., Gurney, M.E., Trojanowski, J.Q., and Lee, V.M. (1996). Transgenic mice carrying a human mutant superoxide dismutase transgene develop neuronal cytoskeletal pathology resembling human amyotrophic lateral sclerosis lesions. Proc. Natl. Acad. Sci. U S A *93*, 3155–3160.

Vance, C., Rogelj, B., Hortobagyi, T., De Vos, K.J., Nishimura, A.L., Sreedharan, J., Hu, X., Smith, B.,

Ruddy, D., Wright, P., et al. (2009). Mutations in FUS, an RNA processing protein, cause familial amyotrophic lateral sclerosis type 6. Science *323*, 1208–1211.

Vatsavayai, S.C., Yoon, S.J., Gardner, R.C., Gendron, T.F., Vargas, J.N., Trujillo, A., Pribadi, M., Phillips, J.J., Gaus, S.E., Hixson, J.D., et al. (2016). Timing and significance of pathological features in C9orf72 expansion-associated frontotemporal dementia. Brain *139*, 3202–3216.

Watts, G.D., Wymer, J., Kovach, M.J., Mehta, S.G., Mumm, S., Darvish, D., Pestronk, A., Whyte, M.P., and Kimonis, V.E. (2004). Inclusion body myopathy associated with Paget disease of bone and frontotemporal dementia is caused by mutant valosin-containing protein. Nat. Genet. *36*, 377–381.

Wong, P.C., Pardo, C.A., Borchelt, D.R., Lee, M.K., Copeland, N.G., Jenkins, N.A., Sisodia, S.S., Cleveland, D.W., and Price, D.L. (1995). An adverse property of a familial ALS-linked SOD1 mutation causes motor neuron disease characterized by vacuolar degeneration of mitochondria. Neuron *14*, 1105–1116.

Woo, J.A., Liu, T., Trotter, C., Fang, C.C., De Narvaez, E., Lepochat, P., Maslar, D., Bukhari, A., Zhao, X., Deonarine, A., et al. (2017). Loss of function CHCHD10 mutations in cytoplasmic TDP-43 accumulation and synaptic integrity. Nat. Commun. *8*, 15558.

Xiao, Y., Zhang, J., Shu, X., Bai, L., Xu, W., Wang, A., Chen, A., Tu, W.-Y., Wang, J., Zhang, K., et al. (2019). Loss of mitochondrial protein CHCHD10 in skeletal muscle causes neuromuscular junction impairment. Hum. Mol. Genet. *29*, 1784–1796.

Zhang, M., Xi, Z., Zinman, L., Bruni, A.C., Maletta, R.G., Curcio, S.A., Rainero, I., Rubino, E., Pinessi, L., Nacmias, B., et al. (2015). Mutation analysis of CHCHD10 in different neurodegenerative diseases. Brain *138*, e380.

iScience, Volume *24*

Supplemental Information

Early death of ALS-linked CHCHD10-R15L transgenic mice with central nervous system, skeletal muscle, and cardiac pathology

Éanna B. Ryan, Jianhua Yan, Nimrod Miller, Sudarshan Dayanidhi, Yongchao C. Ma, Han-Xiang Deng, and Teepu Siddique

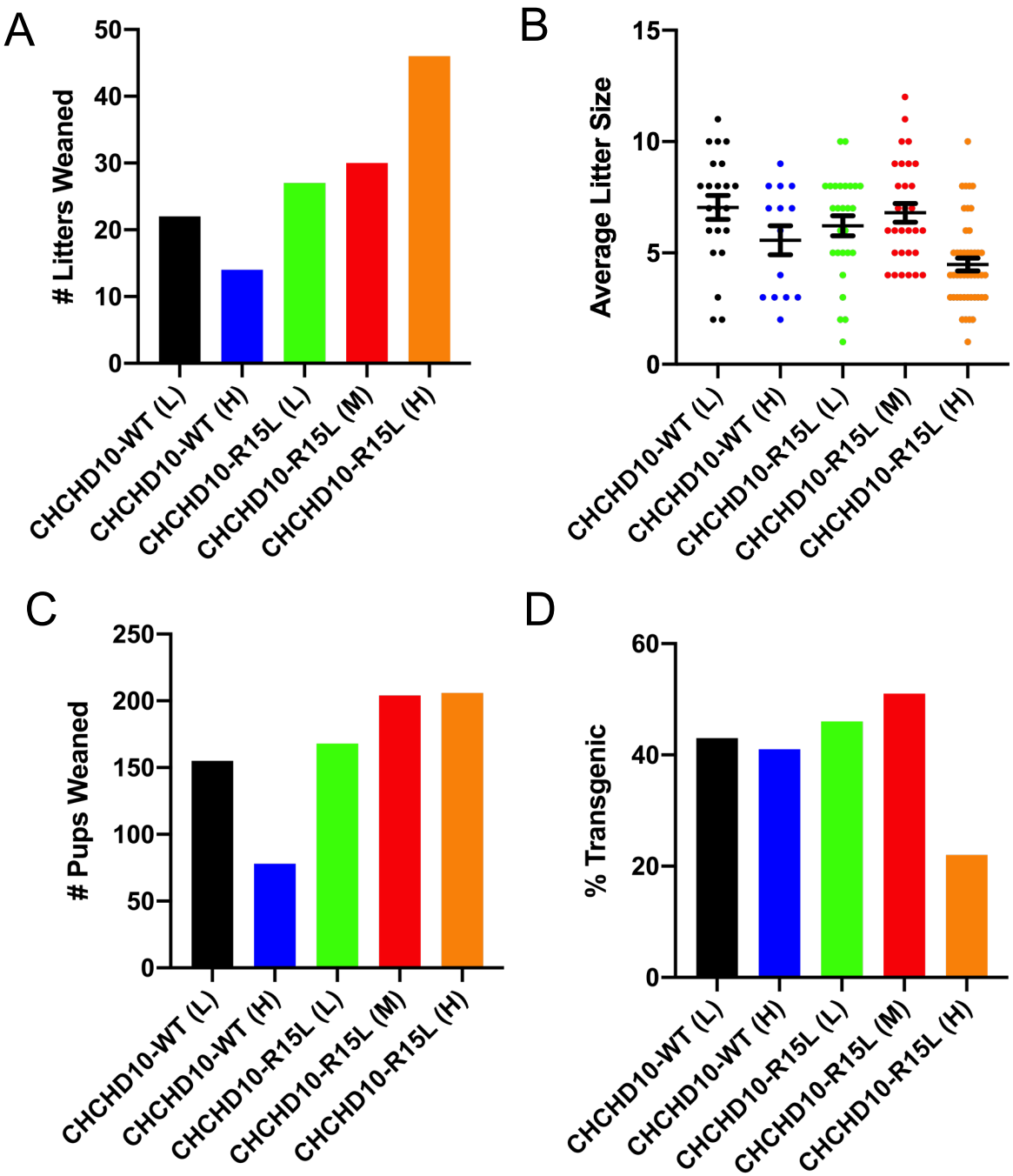

Figure S1. Breeding & Genotyping Summary. Related to Figure 1.

(A) Number of litters weaned.
(B) Average litter size at weaning day P21. Data are represented as mean +/- SEM.
(C) Number of mice weaned at P21.
(D) Percentage of weaned mice that were transgenic.

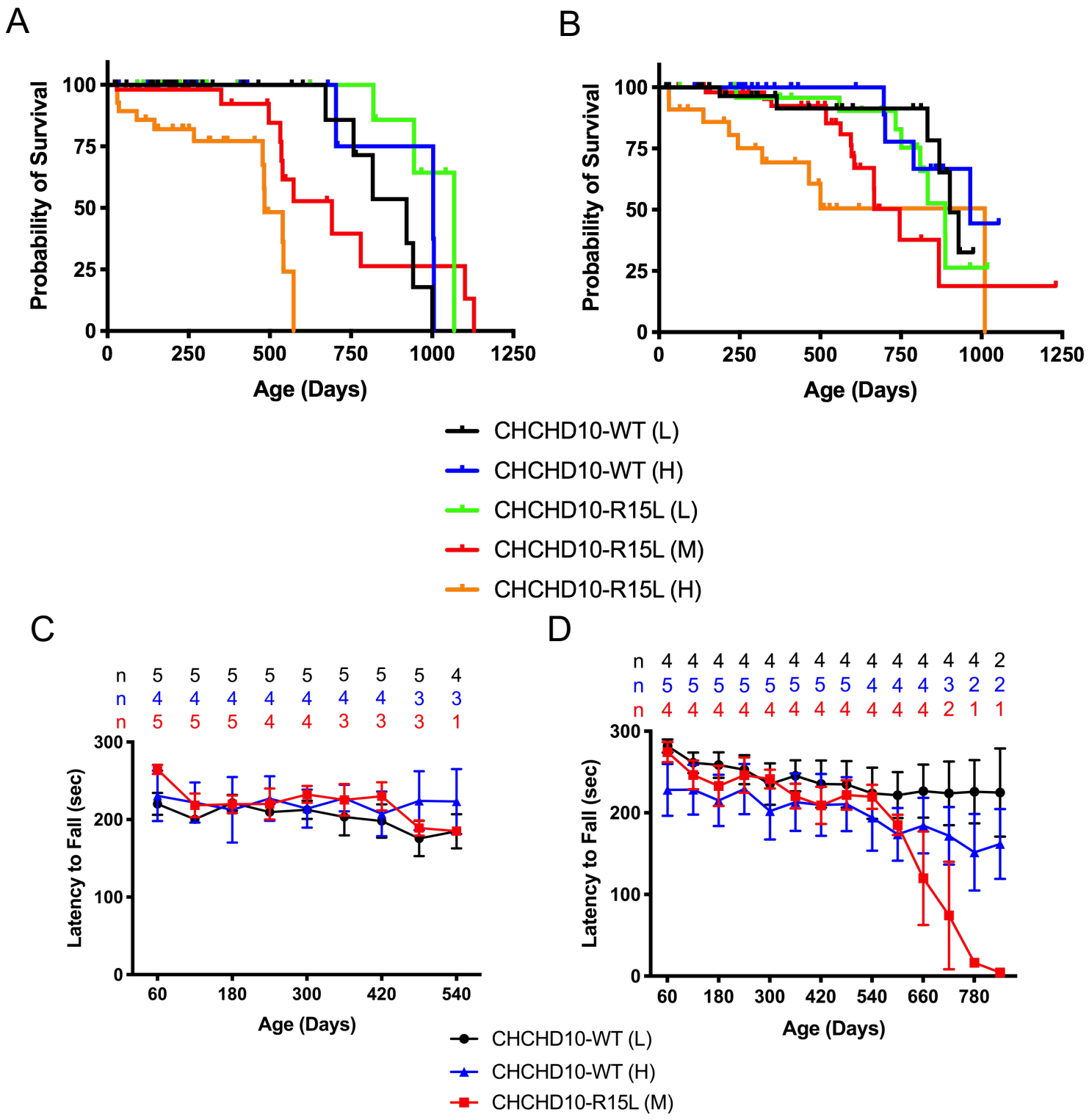

Figure S2. Survival analysis and rotarod testing of CHCHD10 transgenic mice separated by gender. Related to Figures 1 and 2, and Tables S7-S18.

(A) Kaplan-Meier survival analysis of male mice of the indicated CHCHD10 founder lines. Death of a mouse for unknown reasons is considered a death event, as indicated by a drop in the line. Mice still living or death of a mouse due to intervention by the investigators are considered censored events, as indicated by tick marks along a line. Median survival for CHCHD10-WT (L) is 921 days, n=6 death events and n=34 censored events. Median survival for CHCHD10-WT (H) is 1003 days, n=3 death events and n=25 censored events. Gehan-Breslow-Wilcoxon test, p=0.3454 in comparison to CHCHD10-WT (L) line. Median survival for CHCHD10-R15L (L) is 1068 days, n=3 death events and 51 censored events. Gehan-Breslow-Wilcoxon test, p=0.0361 in comparison to

CHCHD10-WT (L) line. Gehan-Breslow-Wilcoxon test, p=0.3496 in comparison to CHCHD10-WT (H) line. Median survival for CHCHD10-R15L (M) is 691 days, n=11 death events and n=52 censored events. Gehan-Breslow-Wilcoxon test, p=0.0977 comparison to CHCHD10-WT (L) line. Gehan-Breslow-Wilcoxon test, p=0.1283 in comparison to CHCHD10-WT (H) line. Median survival for CHCHD10-R15L (H) is 484 days, n=12 death events and n=17 censored events. Gehan-Breslow-Wilcoxon test, p=0.0007 in comparison to CHCHD10-WT (L) line. Gehan-Breslow-Wilcoxon test, p=0.0043 in comparison to CHCHD10-WT (H) line.

(B) Kaplan-Meier survival analysis of female mice of the indicated CHCHD10 founder lines. Death of a mouse for unknown reasons is considered a death event, as indicated by a drop in the line. Mice still living or death of a mouse due to intervention by the investigators are considered censored events, as indicated by tick marks along a line. Median survival for CHCHD10-WT (L) is 902 days, n=6 death events and n=42 censored events. Median survival for CHCHD10-WT (H) is undefined as the mice are still being aged out. n=4 death event and n=26 censored events. Gehan-Breslow-Wilcoxon test, p=0.363 in comparison to CHCHD10-WT (L) line. Median survival for CHCHD10-R15L (L) is 887 days, n=8 death events and 32 censored events. Gehan-Breslow-Wilcoxon test, p=0.7128 in comparison to CHCHD10-WT (L) line. Gehan-Breslow-Wilcoxon test, p=0.3621 in comparison to CHCHD10-WT (H) line. Median survival for CHCHD10 R15L (M) is 746 days, n=13 death events and n=55 censored events. Gehan-Breslow-Wilcoxon test, p=0.2028 comparison to CHCHD10-WT (L) line. Gehan-Breslow-Wilcoxon test, p=0.026 in comparison to CHCHD10-WT (H) line. Median survival for CHCHD10 R15L (H) is 1010 days, n=9 death events and n=13 censored events. Gehan-Breslow-Wilcoxon test, p=0.005 in comparison to CHCHD10-WT (L) line. Gehan-Breslow-Wilcoxon test, p=0.0012 in comparison to CHCHD10-WT (H) line.

(C) Male mouse rotarod performance. Mice were tested on an accelerating rotarod task every 60 days beginning at 60 days of age until all CHCHD10-R15L (M) mice in the cohort died. The overlying numbers indicate the number of mice from each line used to calculate mean latency to fall at each time point. Data are represented as mean +/- SEM. Two way ANOVA with Holm-Šidák post hoc statistical analysis summarized in Table S13-S18.

(D) Female mouse rotarod performance. Mice were tested on an accelerating rotarod task every 60 days beginning at 60 days of age until all CHCHD10-R15L (M) mice in the cohort died. The overlying numbers indicate the number of mice from each line used to calculate mean latency to fall at each time point. Data are represented as mean +/- SEM. Two way ANOVA with Holm-Šidák post hoc statistical analysis summarized in Table S7-S12.

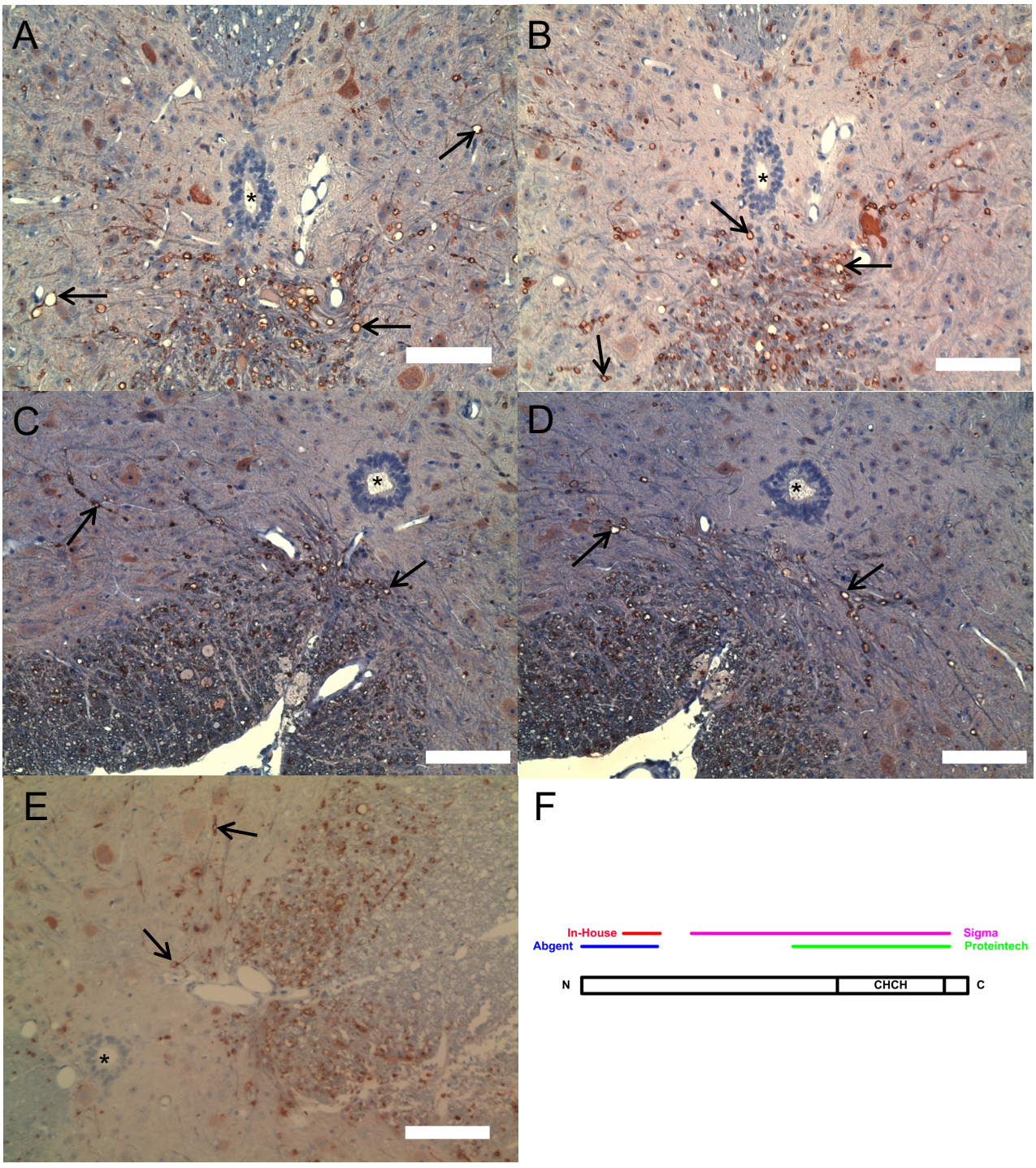

Figure S3. Atypical immunostaining profile of CHCHD10 R15L transgenic mice. Related to Figures 3 and 4.
(A-E) Immunohistochemistry of 10 month old male CHCHD10-R15L (M) mouse spinal cord using different antibodies targeting CHCHD10, demonstrating the ability to visualize axonal pathology using antibodies targeting different epitopes of CHCHD10. (A) In-house designed antibody. (B) Abgent. (C) Proteintech. (D) Millipore. (E) Sigma. Black asterisks indicate the central canal. Black arrows indicate examples of pathological swellings. Scale bars = 100μm.
(F) CHCHD10 protein schematic indicating N- and C-termini and CHCH domain. Overlying bars represent epitopes used to generate indicated antibodies. The Millipore antibody was generated using an unknown 79 amino acid immunogen.

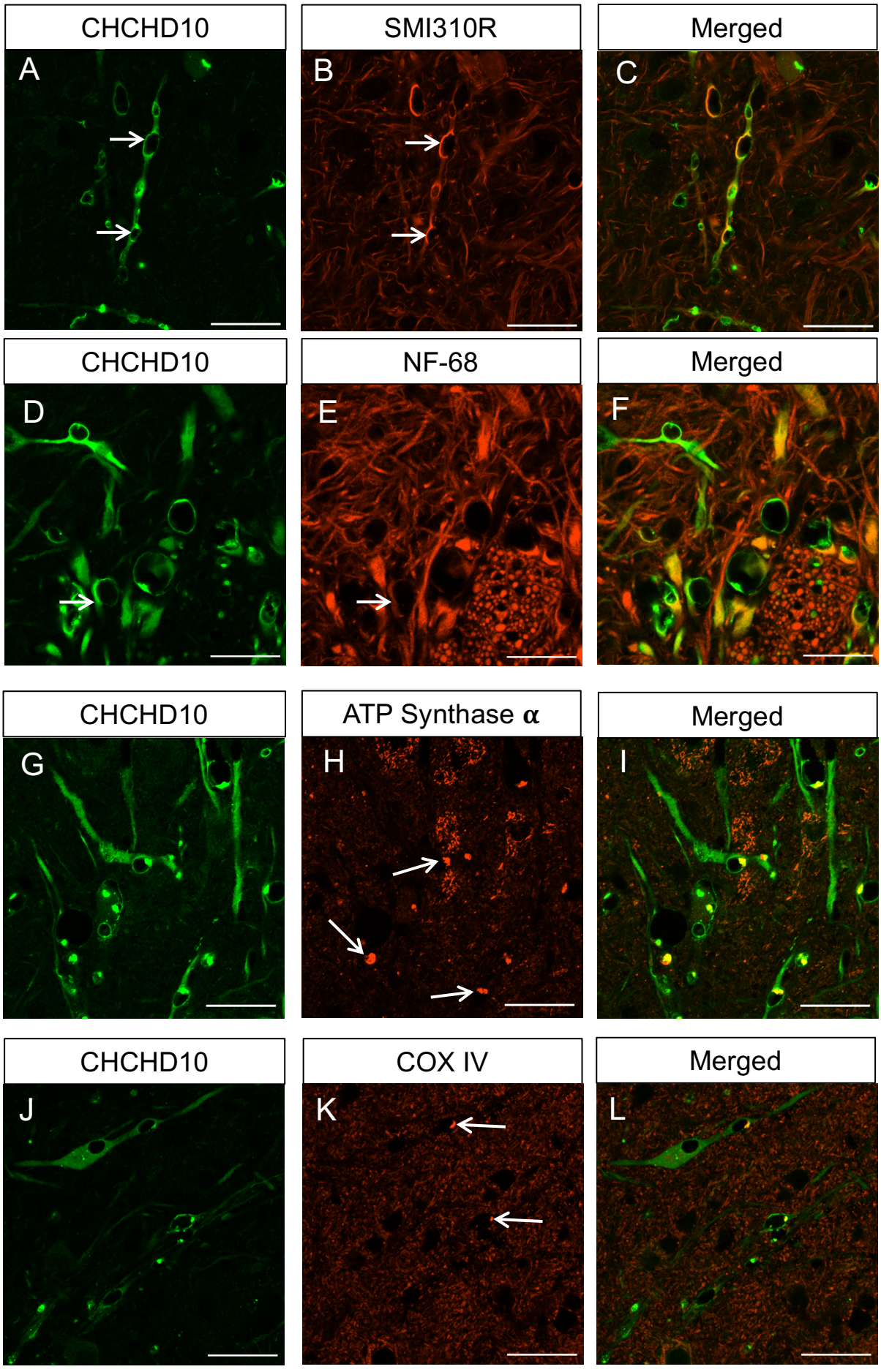
CHCHD10
SMI310R
Merged
A
B
C
CHCHD10
NF-68
Merged
D
E
F
CHCHD10
ATP Synthase α
Merged
G
H
I
CHCHD10
COX IV
Merged
J
K
L

Figure S4. CNS axonal pathology evident in CHCHD10-R15L transgenic mice. Related to Figures 3 and 4.
(A-C) Immunofluorescence of 10 month old CHCHD10-R15L (M) transgenic mice spinal cord gray matter using antibodies targeting CHCHD10 and SMI 310R, phosphorylated neurofilament heavy chain protein. Co-localization indicates that the CHCHD10-positive process harboring pathological swellings (white arrows) is also SMI 310R-positive. Scale bars = 25μm.
(D-F) Immunofluorescence of 10 month old CHCHD10-R15L (M) transgenic mice spinal cord gray matter using antibodies targeting CHCHD10 and NF-68, neurofilament light chain protein. Co-localization indicates a CHCHD10-positive process harboring pathological swellings (white arrow) is also SMI 310R-positive. Scale bars = 25μm.
(G-I) Immunofluorescence of 10 month old male CHCHD10-R15L (M) transgenic mouse spinal cord gray matter using antibodies targeting CHCHD10 and the mitochondrial protein, ATP synthase α. The white arrows in (H) indicate examples of ATP synthase α immunoreactive components of pathological axonal swellings. Scale bars = 25μm.
(J-L) Immunofluorescence of 10 month old male CHCHD10-R15L (M) transgenic mouse spinal cord gray matter using antibodies targeting CHCHD10 and mitochondrial protein complex IV, subunit VIb. The white arrows in (I) indicate examples of complex IV, subunit VIb immunoreactive components of pathological axonal swellings. Scale bars = 25μm.

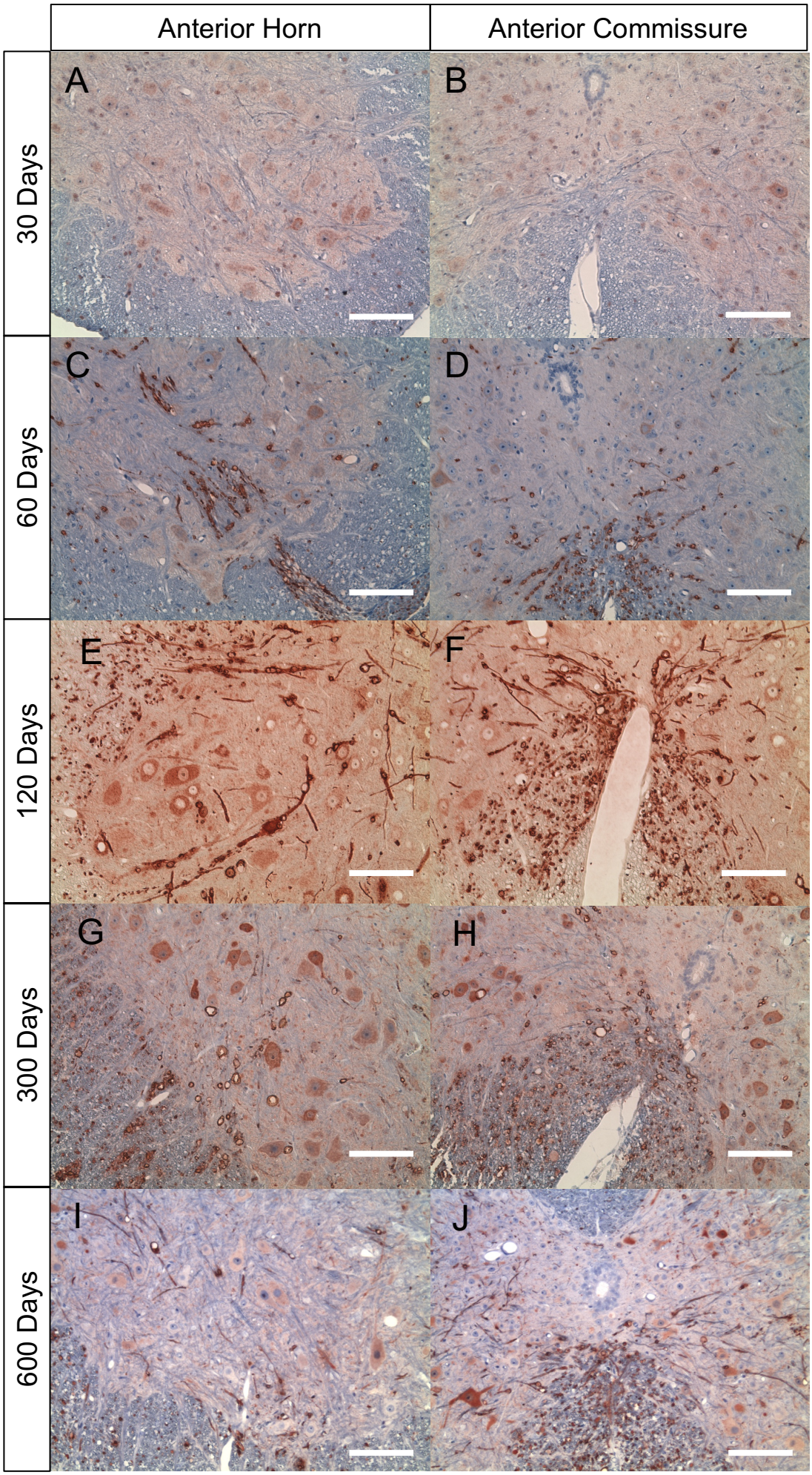
Anterior Horn
Anterior Commissure
30 Days
60 Days
120 Days
300 Days
600 Days
A
B
C
D
E
F
G
H
I
J

Figure S5. Progression of CHCHD10-R15L spinal cord pathology. Related to Figures 3 and 4.
(A-J) Immunohistochemistry, using an antibody targeting CHCHD10, of CHCHD10-R15L (M) transgenic mouse spinal cord displaying the progression of pathology of the indicated regions of the spinal cord at the indicated timepoints. Scale bars = 100μm.

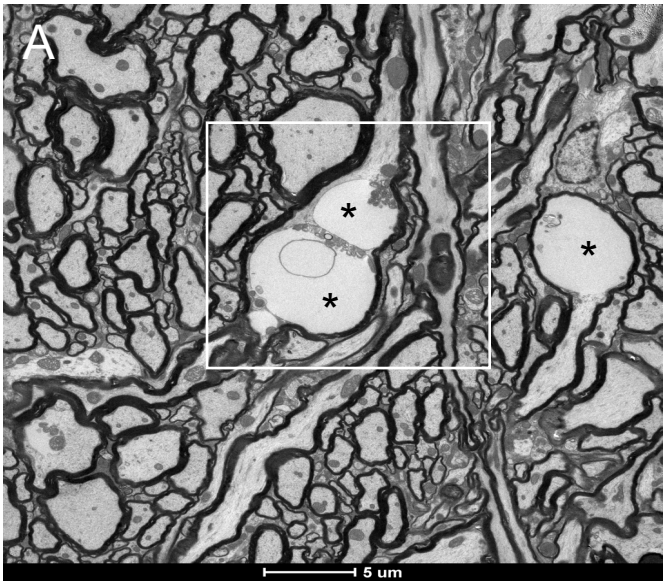
A
5 um

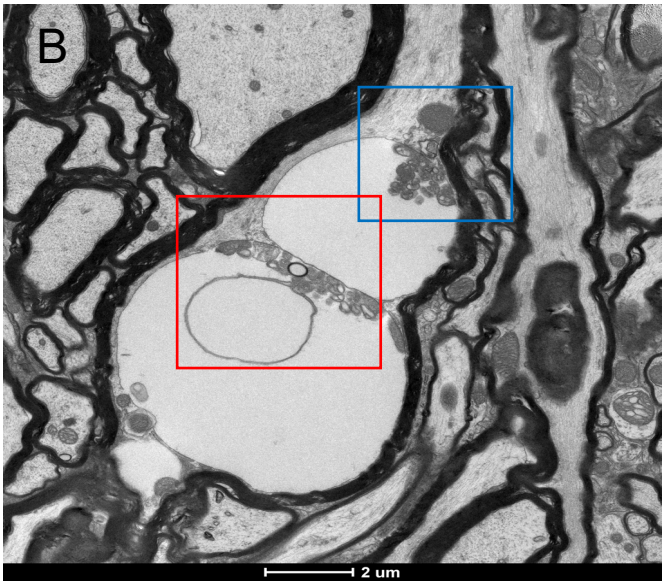
B
2 um

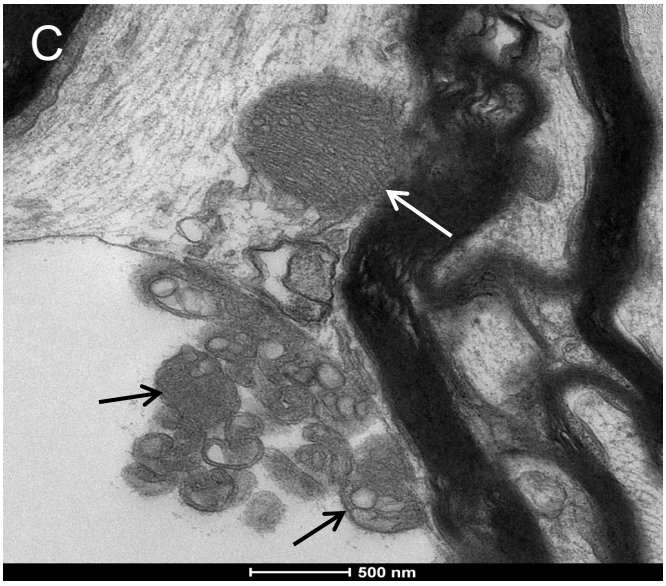
C
500 nm


D
500 nm

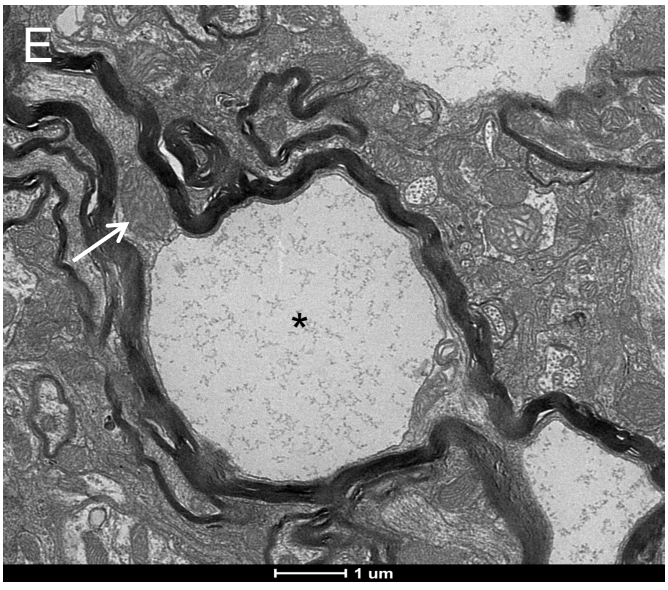
E
1 um

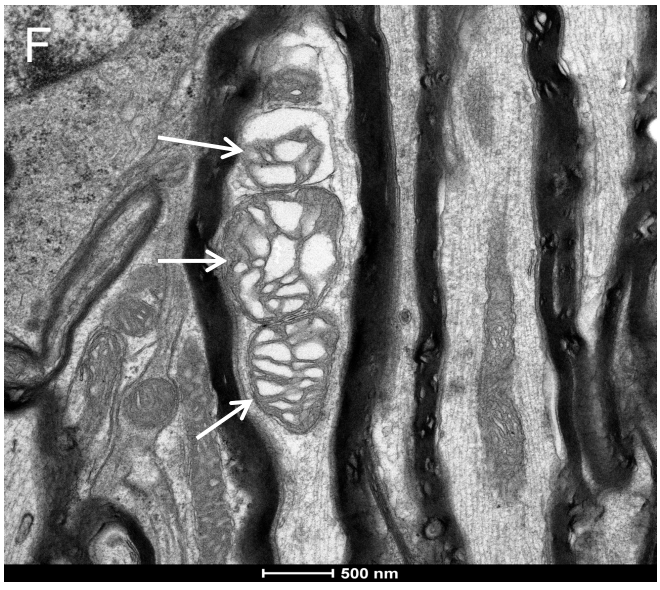
F
500 nm

Figure S6. Transmission electron microscopy images of CHCHD10-R15L (M) spinal cord. Related to Figures 3 and 4.

- **(A)** Black asterisks indicate pathological swellings in axons traversing the spinal cord white matter of a 10 month old male mouse. The white box indicates the region magnified in B.
- **(B)** Two pathological swellings in close apposition are apparent. The blue box indicates the region magnified in C. The red box indicates the region magnified in D.
- **(C)** White arrow indicates a relatively typical mitochondrial profile. Black arrows indicate examples of membranous components of the pathological swelling.
- **(D)** Black arrows indicate examples of membranous components of the pathological swelling.
- **(E)** A myelinated axon in the spinal cord gray matter of a 5 month old male mouse harboring at least one pathologic swelling (black asterisk) is apparent. A mitochondrion is observed apposed to the swelling (white arrow).
- **(F)** A range of mitochondrial profiles are apparent in myelinated axons in the spinal cord gray matter of a 5 month old male mouse. Multiple abnormal, swollen mitochondria are observed, possibly in an early stage of development of the pathology (white arrows).

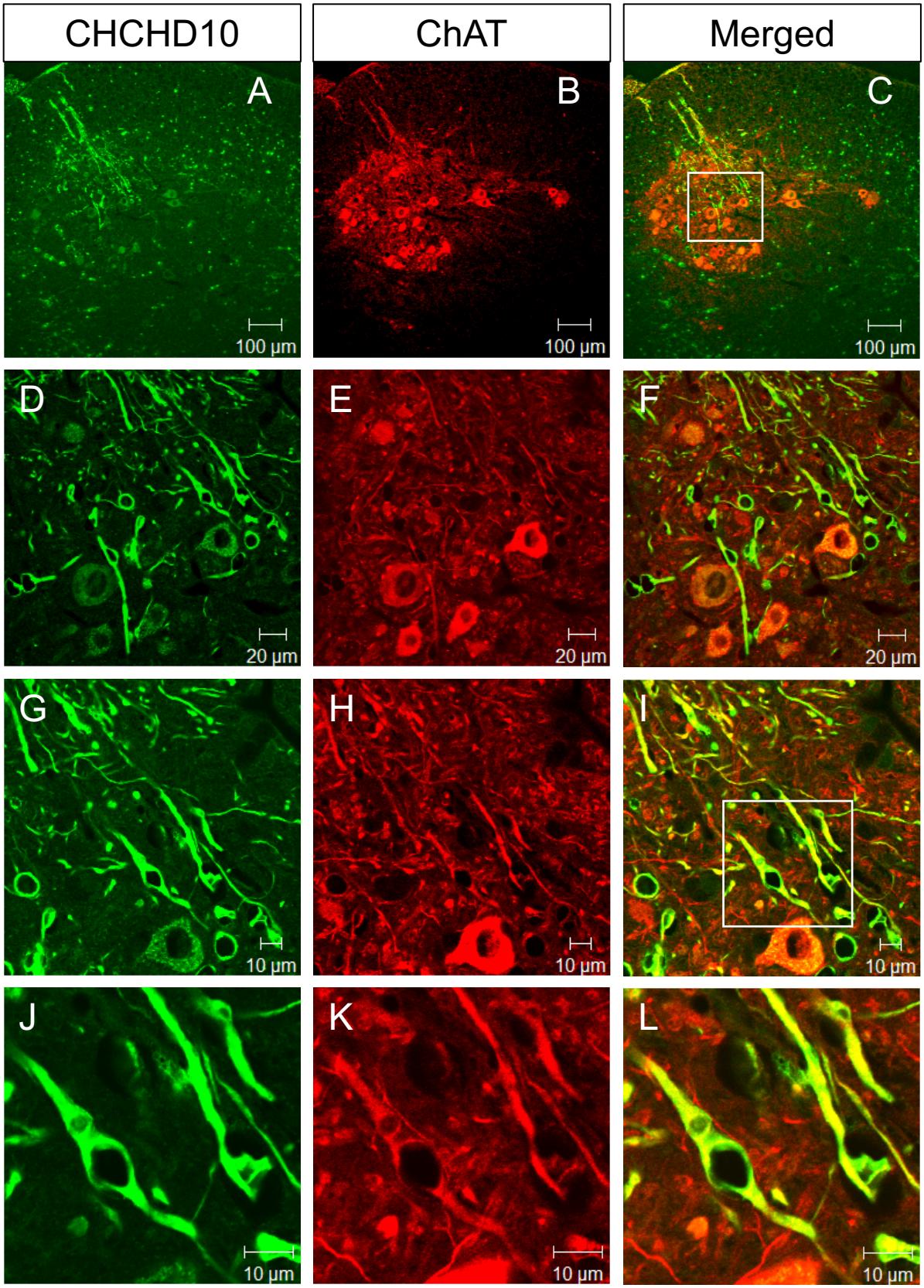

Figure S7. Axonal swellings present in spinal cord anterior horn cholinergic neurons. Related to Figures 3 and 4. (A-L) Immunofluorescence of 4 month old CHCHD10-R15L (M) transgenic mouse spinal cord anterior horn using antibodies targeting CHCHD10 and Choline Acetyl Transferase (ChAT). Co-localization indicates that the ChAT-positive neurons harbor pathological axonal swellings. White boxes indicate the regions magnified in the panels below. Scale bar sizes indicated in figure.

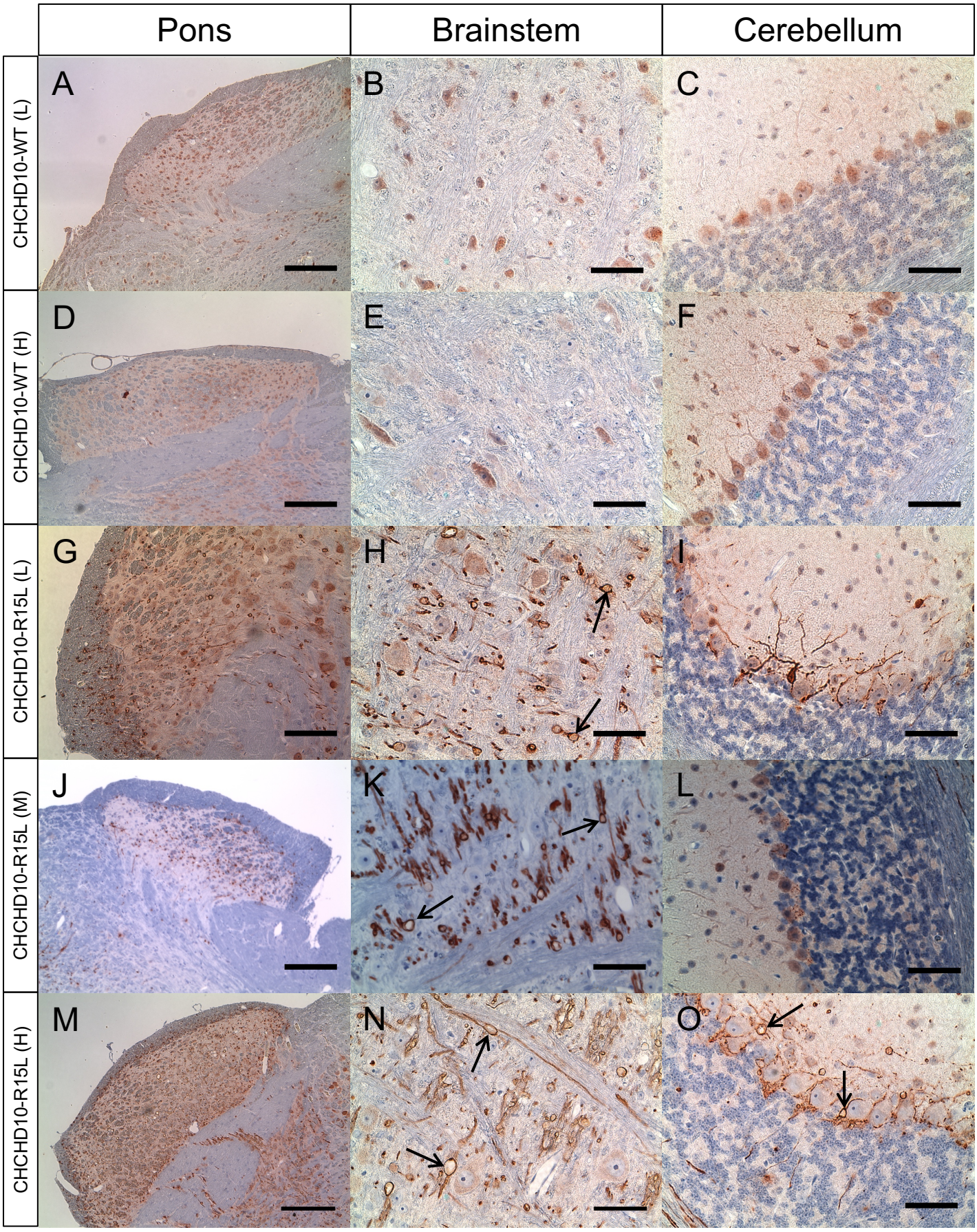
Pons
Brainstem
Cerebellum
CHCHD10-WT (L)
CHCHD10-WT (H)
CHCHD10-R15L (L)
CHCHD10-R15L (M)
CHCHD10-R15L (H)
A
B
C
D
E
F
G
H
I
J
K
L
M
N
O

Figure S8. Immunohistochemistry of indicated brain regions using an antibody targeting CHCHD10. Related to Figures 3 and 4.
(A-C) 20 month old female CHCHD10-WT (L) transgenic mouse. Scale bar in (A) = 200μm. Scale bar in (B, C) = 50μm.
(D-F) 13 month old female CHCHD10-WT (H) transgenic mouse. Scale bar in (D) = 200μm. Scale bar in (E, F) = 50μm.
(G-I) 12 month old female CHCHD10-R15L (L) transgenic mouse. Black arrows indicated examples of pathological swellings. Scale bar in (G) = 200μm. Scale bar in (H, I) = 50μm.
(J-L) 20 month old female CHCHD10-R15L (M) transgenic mouse. Black arrows indicated examples of pathological swellings. Scale bar in (J) = 200μm. Scale bar in (K, L) = 50μm.
(M-O) 14 month old female CHCHD10-R15L (H) transgenic mouse. Black arrows indicated examples of pathological swellings. Scale bar in (M) = 200μm. Scale bar in (N, O) = 50μm.

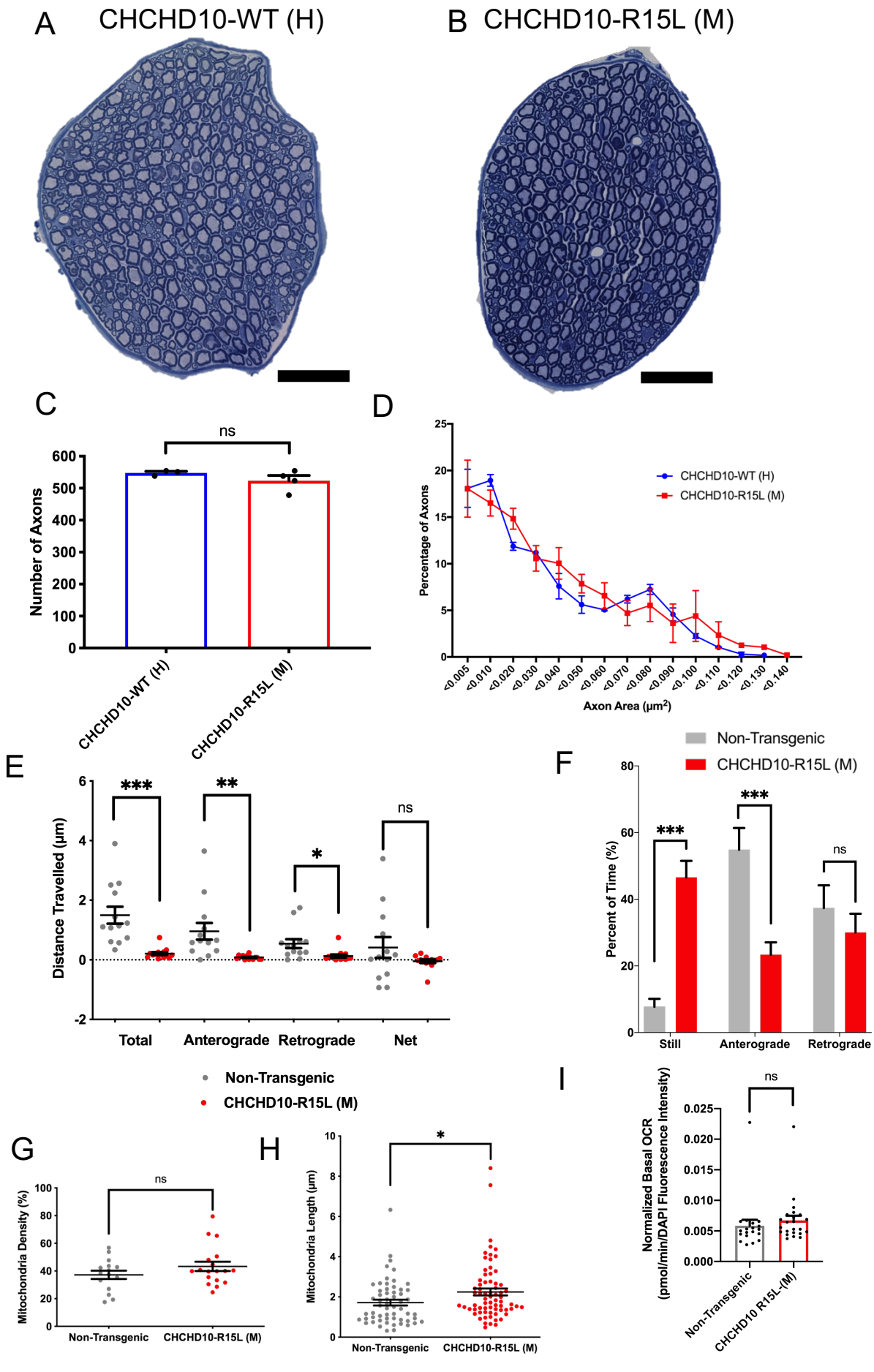
A
CHCHD10-WT (H)
B
CHCHD10-R15L (M)
C
ns
Number of Axons
600
500
400
300
200
100
0
CHCHD10-WT (H)
CHCHD10-R15L (M)
D
Percentage of Axons
25
20
15
10
5
0
CHCHD10-WT (H)
CHCHD10-R15L (M)
≤0.005
≤0.010
≤0.020
≤0.030
≤0.040
≤0.050
≤0.060
≤0.070
≤0.080
≤0.090
≤0.100
≤0.110
≤0.120
≤0.130
≤0.140
Axon Area (μm²)
E
Distance Travelled (μm)
6
4
2
0
-2
***
**
*
ns
Total
Anterograde
Retrograde
Net
Non-Transgenic
CHCHD10-R15L (M)
F
Non-Transgenic
CHCHD10-R15L (M)
Percent of Time (%)
80
60
40
20
0
***
***
ns
Still
Anterograde
Retrograde
G
Mitochondria Density (%)
100
80
60
40
20
0
ns
Non-Transgenic
CHCHD10-R15L (M)
H
Mitochondria Length (μm)
10
8
6
4
2
0
*
Non-Transgenic
CHCHD10-R15L (M)
I
Normalized Basal OCR (pmol/min/DAPI Fluorescence Intensity)
0.025
0.020
0.015
0.010
0.005
0.000
ns
Non-Transgenic
CHCHD10 R15L-(M)

Figure S9. Femoral nerve motor branch axon counts and area distribution and mitochondrial transport analysis in spinal cord primary neurons. Related to Figures 3 and 4, and Table S34.

(A) Representative toluidine blue stained 1µm semithin transverse section of the femoral nerve motor branch from a CHCHD10-WT (H) transgenic mouse. Scale bar = 50µm.

(B) Representative toluidine blue stained 1µm semithin transverse section of the femoral nerve motor branch from a CHCHD10-R15L (M) transgenic mouse. Scale bar = 50 µm.

(C) Quantitation of the number of axons for the indicated genotype. CHCHD10 WT (H) n=3 9 month old mice. CHCHD10 R15L (M) n=4 7 month old mice. Data are represented as mean +/- SEM. Unpaired t test, ns $p>0.05$.

(D) Quantitation of the percentage of axons of the total population for the indicated genotype binned by axonal area. CHCHD10 WT (H) n=3 9 month old mice. CHCHD10 R15L (M) n=4 7 month old mice. Data are represented as mean +/- SEM. Unpaired t test statistical analysis for each axon area is summarized in Table S34.

(E) Distance travelled by mitochondria in primary spinal cord neurons derived from E12.5 CHCHD10-R15L (M) mice or non-transgenic littermates. Data are represented as mean +/- SEM. Unpaired t test, ns $p>0.05$, * $p<0.05$, ** $p<0.01$, *** $p<0.001$

(F) Percent of time mitochondria observed to be stationary, moving anterogradely or retrogradely. Data are represented as mean +/- SEM. Unpaired t test, ns $p>0.05$, *** $p<0.001$.

(G) Density of mitochondria in primary spinal cord neurons. Data are represented as mean +/- SEM. Unpaired t test, ns $p>0.05$.

(H) Length of mitochondria in primary spinal cord neurons. Data are represented as mean +/- SEM. Unpaired t test, * $p<0.05$.

(I) Basal mitochondrial oxygen consumption of primary spinal cord neurons derived from E12.5 CHCHD10-R15L (M) mice or non-transgenic littermates. Data are represented as mean +/- SEM. Unpaired t test, ns $p>0.05$.

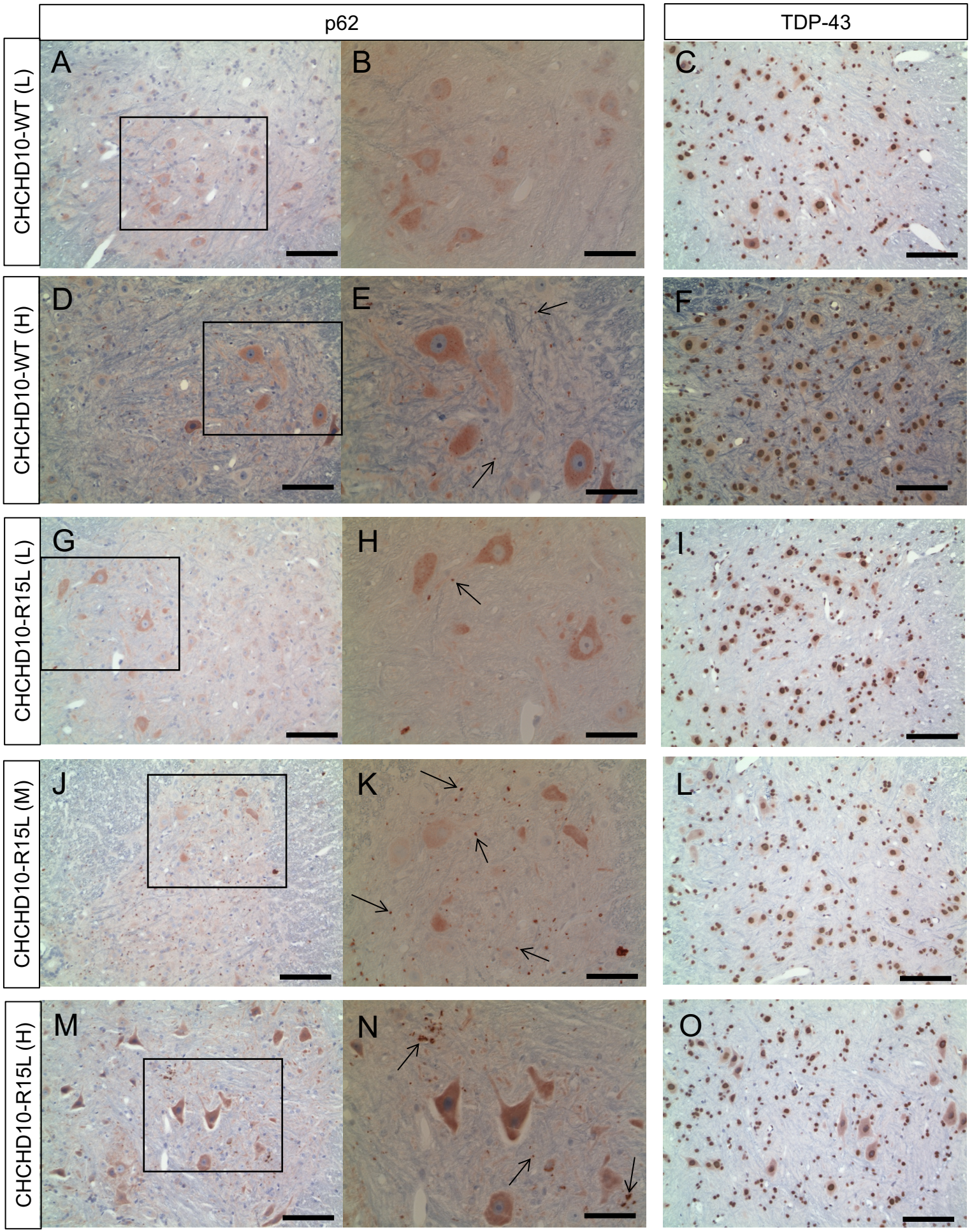
p62
TDP-43
CHCHD10-WT (L)
CHCHD10-WT (H)
CHCHD10-R15L (L)
CHCHD10-R15L (M)
CHCHD10-R15L (H)
A
B
C
D
E
F
G
H
I
J
K
L
M
N
O

Figure S10. Immunohistochemistry of spinal cord anterior horn using indicated antibodies. Related to Figures 3 and 4.
(A-C) 20 month old male CHCHD10-WT (L) transgenic mouse. Black box in A represents region magnified in B. Scale bars A, C = 100μm. Scale bar B = 50μm.
(D-F) 35 month old male CHCHD10-WT (H) transgenic mouse. Black box in D represents region magnified in E. Scale bars D, F = 100μm. Scale bar E = 50μm. Black arrows indicate examples of rare p62-positive puncta.
(G-I) 20 month old female CHCHD10-R15L (L) transgenic mouse. Black box in G represents region magnified in H. Scale bars G, I = 100μm. Scale bar H = 50μm. Black arrows indicate examples of rare p62-positive puncta.
(J-L) 20 month old female CHCHD10-R15L (M) transgenic mouse. Black box in J represents region magnified in K. Scale bars J, L = 100μm. Scale bar K = 50μm. Black arrows indicate examples of abundant p62-positive puncta.
(M-O) 14 month old female CHCHD10-R15L (H) transgenic mouse. Black box in M represents region magnified in N. Scale bars M, O = 100μm. Scale bar N = 50μm. Black arrows indicate examples of abundant p62-positive puncta.

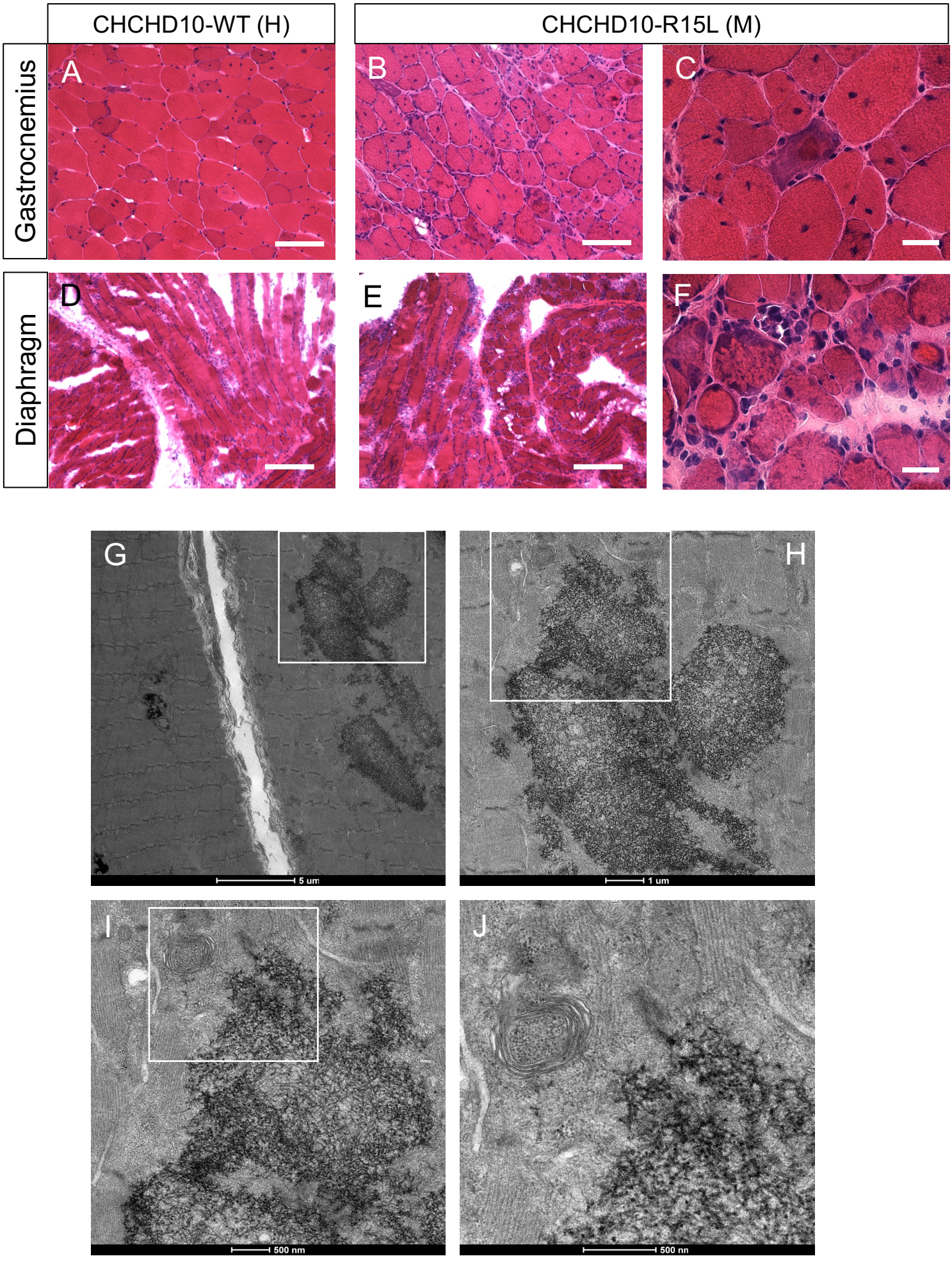
CHCHD10-WT (H)
CHCHD10-R15L (M)
Gastrocnemius
Diaphragm
A
B
C
D
E
F
G
H
I
J
5 um
1 um
500 nm
500 nm

Figure S11. Skeletal muscle myopathic features. Relate to Figure 5.
(A-F) Hematoxylin and eosin staining of gastrocnemius (A-C) and diaphragm (D-F) of 14 month old female CHCHD10-WT (H) and 15 month old female CHCHD10-R15L (M) mice. Abundant myopathic features are apparent in the CHCHD10-R15L (M) transgenic mice including central nuclei, hematoxylin invasion, eosinophilic cores. Milder myopathic changes are apparent in CHCHD10-WT (H) skeletal muscle with occasional central nuclei. Scale bars (A, B) = 100μm. Scale bar (C) = 25μm.
(G-J) Transmission electron microscopy images of quadriceps from a 10 month old male CHCHD10-R15L (M) mouse. White box in G indicates the region magnified in H. White box in H indicates the region magnified in I. White box in I indicates the region magnified in J. The myofibrillary network is disturbed by large electron-dense, possibly fibrous material of unknown composition or origin.

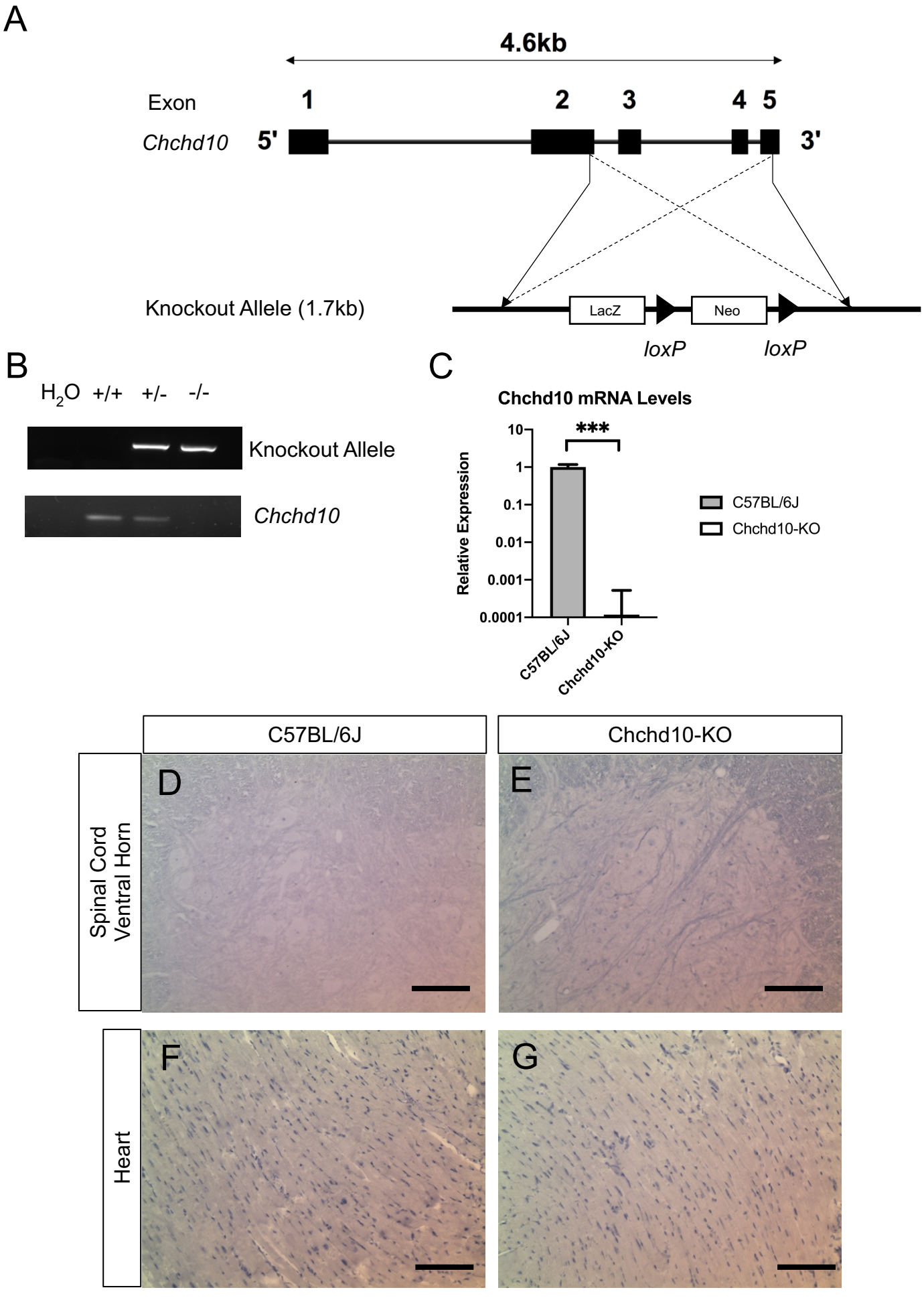
A
4.6kb
Exon
1
2
3
4
5
Chchd10
5'
3'
Knockout Allele (1.7kb)
LacZ
Neo
loxP
loxP
B
H2O
+/+
+/-
-/-
Knockout Allele
Chchd10
C
Chchd10 mRNA Levels
***
Relative Expression
10
1
0.1
0.01
0.001
0.0001
C57BL/6J
Chchd10-KO
C57BL/6J
Chchd10-KO
Spinal Cord Ventral Horn
D
E
Heart
F
G

Figure S12. Chchd10-Knockout mouse design and pathology. Related to Figure 8.

- **(A)** Design strategy employed by the UC Davis knockout mouse project to knockout Chchd10.
- **(B)** PCR amplification of indicated alleles demonstrating knockout of Chchd10 in homozygous condition.
- **(C)** qRT-PCR result demonstrating the lack of Chchd10 mRNA transcript in Chchd10-KO mouse spinal cord. Gapdh is used as a reference. Relative expression levels represent the mean of three biological and three technical replicates. Data are represented as mean +/- confidence intervals. Unpaired t test of ΔC_T, ***p<0.001.
- **(D)** Immunohistochemical staining of 10 month old male C57BL/6J transverse spinal cord using an antibody targeting CHCHD10 does not reveal any obvious pathology. Scale bar = 100μm.
- **(E)** Immunohistochemical staining of 10 month old female Chchd10-KO transverse spinal cord using an antibody targeting CHCHD10 does not reveal any obvious pathology. Scale bar = 100μm.
- **(F)** Immunohistochemical staining of 22 month old female C57BL/6J heart using an antibody targeting CHCHD10 does not reveal any obvious pathology. Scale bar = 100μm.
- **(G)** Immunohistochemical staining of 25 month old male Chchd10-KO heart using an antibody targeting CHCHD10 does not reveal any obvious pathology. Scale bar = 100μm.

Two-way ANOVA	Ordinary	
Alpha	0.05	
Source of Variation	**% of total variation**	**P value**
Interaction	21.4	<0.0001
Age	32.41	<0.0001
Genotype	11.23	<0.0001

ANOVA table	**SS**	**DF**	**MS**	**F (DFn, DFd)**	**P value**
Interaction	120869	13	9298	F (13, 168) = 4.547	P<0.0001
Age	183027	13	14079	F (13, 168) = 6.885	P<0.0001
Genotype	63399	1	63399	F (1, 168) = 31.01	P<0.0001
Residual	343521	168	2045		

Table S1. Two-way ANOVA analysis of rotarod performance between CHCHD10-WT (L) and CHCHD10-R15L (M) transgenic mouse lines. Related to Figure 2A, Table S2.

Sidak's multiple comparisons test	Mean Diff.	95.00% CI of diff.	Adjusted P Value
WT (L) - R15L (M) (Days)			
60	-21.4	-84.23 to 41.44	0.9952
120	-3.42	-66.25 to 59.42	>0.9999
180	12.33	-50.5 to 75.17	>0.9999
240	-4.418	-69.19 to 60.35	>0.9999
300	-14.25	-79.02 to 50.52	>0.9999
360	-0.619	-67.79 to 66.55	>0.9999
420	-3.413	-70.59 to 63.76	>0.9999
480	-5.813	-72.99 to 61.36	>0.9999
540	-8.333	-84.32 to 67.66	>0.9999
600	27.22	-54.4 to 108.8	0.9961
660	102.5	20.86 to 184.1	0.0041
720	145.8	40.47 to 251.2	0.001
780	191.8	49.3 to 334.3	0.0015
840	198.4	49.39 to 347.4	0.0018

Table S2. Holm-Šidák post hoc statistical analysis of rotarod performance between CHCHD10-WT (L) and CHCHD10-R15L (M) transgenic mouse lines for each timepoint. Related to Figure 2A, Table S1.

Two-way ANOVA	Ordinary	
Alpha	0.05	
Source of Variation	% of total variation	P value
Interaction	13.32	0.0063
Age	28.55	<0.0001
Genotype	4.164	0.0022

ANOVA table	SS (Type III)	DF	MS	F (DFn, DFd)	P value
Interaction	93318	13	7178	F (13, 157) = 2.374	P=0.0063
Age	200058	13	15389	F (13, 157) = 5.089	P<0.0001
Genotype	29175	1	29175	F (1, 157) = 9.648	P=0.0022
Residual	474745	157	3024		

Table S3. Two-way ANOVA analysis of rotarod performance between CHCHD10-WT (H) and CHCHD10-R15L (M) transgenic mouse lines. Related to Figure 2A, Table S4.

Sidak's multiple comparisons test	Predicted (LS) mean diff.	95.00% CI of diff.	Adjusted P Value
R15L (M) - WT (H)			
60	39.77	-36.72 to 116.3	0.8507
120	5.321	-71.17 to 81.81	>0.9999
180	11.59	-64.90 to 88.08	>0.9999
240	5.023	-73.82 to 83.86	>0.9999
300	29.48	-49.37 to 108.3	0.9882
360	3.014	-78.75 to 84.78	>0.9999
420	9.4	-72.37 to 91.17	>0.9999
480	-3.46	-90.19 to 83.27	>0.9999
540	6.19	-88.82 to 101.2	>0.9999
600	5.444	-96.25 to 107.1	>0.9999
660	-68.64	-170.3 to 33.06	0.499
720	-117	-252.7 to 18.79	0.1553
780	-170	-351.4 to 11.38	0.0855
840	-183.5	-364.9 to -2.121	0.0451

Table S4. Holm-Šidák post hoc statistical analysis of rotarod performance between CHCHD10-WT (H) and CHCHD10-R15L (M) transgenic mouse lines for each timepoint. Related to Figure 2A, Table S3.

Two-way ANOVA	Ordinary	
Alpha	0.05	
Source of Variation	% of total variation	P value
Interaction	1.474	0.9975
Age	5.433	0.5888
Genotype	1.445	0.085

ANOVA table	SS (Type III)	DF	MS	F (DFn, DFd)	P value
Interaction	9510	13	731.5	F (13, 191) = 0.2351	P=0.9975
Age	35064	13	2697	F (13, 191) = 0.8670	P=0.5888
Genotype	9328	1	9328	F (1, 191) = 2.999	P=0.0850
Residual	594194	191	3111		

Table S5. Two-way ANOVA analysis of rotarod performance between CHCHD10-WT (L) and CHCHD10-WT (H) transgenic mouse lines. Related to Figure 2A, Table S6.

Sidak's multiple comparisons test	Predicted (LS) mean diff.	95.00% CI of diff.	Adjusted P Value
WT (L) - WT (H)			
60	18.37	-59.00 to 95.74	>0.9999
120	1.901	-75.47 to 79.27	>0.9999
180	23.93	-53.45 to 101.3	0.9982
240	0.6049	-76.77 to 77.98	>0.9999
300	15.22	-62.15 to 92.59	>0.9999
360	2.395	-74.98 to 79.77	>0.9999
420	5.988	-71.38 to 83.36	>0.9999
480	-9.273	-91.99 to 73.44	>0.9999
540	-2.143	-87.09 to 82.80	>0.9999
600	32.67	-52.28 to 117.6	0.985
660	33.85	-51.10 to 118.8	0.9795
720	28.88	-64.69 to 122.4	0.9983
780	21.77	-81.11 to 124.6	>0.9999
840	14.89	-101.2 to 130.9	>0.9999

Table S6. Holm-Šidák post hoc statistical analysis of rotarod performance between CHCHD10-WT (L) and CHCHD10-WT (H) transgenic mouse lines for each timepoint. Related to Figure 2A, Table S5.

Two-way ANOVA	Ordinary
Alpha	0.05
Source of Variation	% of total variation
Interaction	19.46
Age	36.87
Genotype	17.99

ANOVA table	SS	DF	MS	F (DFn, DFd)	P value
Interaction	84734	13	6518	F (13, 74) = 2.379	P=0.0100
Age	160567	13	12351	F (13, 74) = 4.509	P<0.0001
Genotype	78359	1	78359	F (1, 74) = 28.6	P<0.0001
Residual	202715	74	2739		

Table S7. Two-way ANOVA analysis of rotarod performance between CHCHD10-WT (L) and CHCHD10-R15L (M) transgenic female mice. Related to Figure S2D, Table S8.

Sidak's multiple comparisons test	Mean Diff.	95.00% CI of diff.	Adjusted P Value
WT (L) - R15L (M) (Days)			
60	7.444	-103.7 to 118.5	>0.9999
120	14.78	-96.32 to 125.9	>0.9999
180	25.58	-85.51 to 136.7	>0.9999
240	6.639	-104.5 to 117.7	>0.9999
300	-6.167	-117.3 to 104.9	>0.9999
360	24.92	-86.18 to 136	>0.9999
420	26.22	-84.88 to 137.3	0.9999
480	13.08	-98.01 to 124.2	>0.9999
540	4.333	-106.8 to 115.4	>0.9999
600	36.5	-74.6 to 147.6	0.9961
660	106.8	-4.347 to 217.8	0.0695
720	149.6	13.52 to 285.6	0.0206
780	209.6	33.95 to 385.3	0.0085
840	220.5	28.07 to 412.9	0.0134

Table S8. Holm-Šidák post hoc statistical analysis of rotarod performance between CHCHD10-WT (L) and CHCHD10-R15L (M) transgenic female mice for each timepoint. Related to Figure S2D, Table S7.

Two-way ANOVA	Ordinary	
Alpha	0.05	
Source of Variation	% of total variation	P value
Interaction	11.31	0.3397
Age	34.36	0.0003
Genotype	1.423	0.1759

ANOVA table	SS (Type III)	DF	MS	F (DFn, DFd)	P value
Interaction	60761	13	4674	F (13, 79) = 1.140	P=0.3397
Age	184570	13	14198	F (13, 79) = 3.463	P=0.0003
Genotype	7647	1	7647	F (1, 79) = 1.865	P=0.1759
Residual	323930	79	4100		

Table S9. Two-way ANOVA analysis of rotarod performance between CHCHD10-WT (H) and CHCHD10-R15L (M) transgenic female mice. Related to Figure S2D, Table S10.

Sidak's multiple comparisons test	Predicted (LS) mean diff.	95.00% CI of diff.	Adjusted P Value
R15L (M) - WT (H)			
60	46.26	-82.42 to 174.9	0.9908
120	18.05	-110.6 to 146.7	>0.9999
180	17.75	-110.9 to 146.4	>0.9999
240	17.11	-111.6 to 145.8	>0.9999
300	39.26	-89.42 to 167.9	0.9982
360	7.383	-121.3 to 136.1	>0.9999
420	-0.65	-129.3 to 128.0	>0.9999
480	11.24	-117.4 to 139.9	>0.9999
540	25.67	-110.0 to 161.3	>0.9999
600	11.64	-124.0 to 147.3	>0.9999
660	-64.58	-200.2 to 71.06	0.9095
720	-97.54	-272.6 to 77.57	0.7682
780	-135.3	-370.3 to 99.60	0.726
840	-157.6	-392.5 to 77.32	0.4969

Table S10. Holm-Šidák post hoc statistical analysis of rotarod performance between CHCHD10-WT (H) and CHCHD10-R15L (M) transgenic female mice for each timepoint. Related to Figure S2D, Table S9.

Two-way ANOVA	Ordinary	
Alpha	0.05	
Source of Variation	% of total variation	P value
Interaction	1.225	>0.9999
Age	9.795	0.6676
Genotype	10.36	0.0014

ANOVA table	SS (Type III)	DF	MS	F (DFn, DFd)	P value
Interaction	5244	13	403.4	F (13, 85) = 0.09893	P>0.9999
Age	41930	13	3225	F (13, 85) = 0.7910	P=0.6676
Genotype	44336	1	44336	F (1, 85) = 10.87	P=0.0014
Residual	346611	85	4078		

Table S11. Two-way ANOVA analysis of rotarod performance between CHCHD10-WT (L) and CHCHD10-WT (H) transgenic female mice. Related to Figure S2D, Table S12.

Sidak's multiple comparisons test	Predicted (LS) mean diff.	95.00% CI of diff.	Adjusted P Value
WT (L) - WT (H)			
60	53.7	-73.62 to 181.0	0.9565
120	32.83	-94.49 to 160.1	0.9995
180	43.33	-83.99 to 170.7	0.9928
240	23.74	-103.6 to 151.1	>0.9999
300	33.09	-94.23 to 160.4	0.9995
360	32.3	-95.02 to 159.6	0.9996
420	25.57	-101.7 to 152.9	>0.9999
480	33.33	-100.9 to 167.5	0.9997
540	25.67	-108.5 to 159.9	>0.9999
600	48.14	-86.07 to 182.3	0.9884
660	42.17	-92.04 to 176.4	0.9966
720	52.05	-92.91 to 197.0	0.9883
780	74.28	-90.09 to 238.6	0.9285

Table S12. Holm-Šidák post hoc statistical analysis of rotarod performance between CHCHD10-WT (L) and CHCHD10-WT (H) transgenic female mice for each timepoint. Related to Figure S2D, Table S11.

Two-way ANOVA	Ordinary	
Alpha	0.05	
Source of Variation	% of total variation	P value
Interaction	3.531	0.9239
Age	19.58	0.0458
Genotype	5.125	0.0385

ANOVA table	SS	DF	MS	F (DFn, DFd)	P value
Interaction	3523	8	440.4	F (8, 59) = 0.386	P=0.9239
Age	19532	8	2442	F (8, 59) = 2.14	P=0.0458
Genotype	5113	1	5113	F (1, 59) = 4.483	P=0.0385
Residual	67303	59	1141		

Table S13. Two-way ANOVA analysis of rotarod performance between CHCHD10-WT (L) and CHCHD10-R15L (M) transgenic male mice. Related to Figure S2C, Table S14.

Sidak's multiple comparisons test	Mean Diff.	95.00% CI of diff.	Adjusted P Value
WT (L) - R15L (M) (Days)			
60	-44.47	-105.8 to 16.85	0.3185
120	-17.98	-79.29 to 43.34	0.9904
180	1.733	-59.58 to 63.05	>0.9999
240	-10.67	-75.7 to 54.37	0.9999
300	-19.83	-84.86 to 45.21	0.9874
360	-22.19	-92.99 to 48.61	0.9848
420	-31.92	-102.7 to 38.88	0.8668
480	-13.44	-84.24 to 57.36	0.9997
540	-0.3333	-108.7 to 108.1	>0.9999

Table S14. Holm-Šidák post hoc statistical analysis of rotarod performance between CHCHD10-WT (L) and CHCHD10-R15L (M) transgenic male mice for each timepoint. Related to Figure S2C, Table S13.

Two-way ANOVA	Ordinary	
Alpha	0.05	
Source of Variation	% of total variation	P value
Interaction	5.566	0.9201
Age	6.859	0.8629
Genotype	0.001808	0.9747

ANOVA table	SS (Type III)	DF	MS	F (DFn, DFd)	P value
Interaction	7097	8	887.1	F (8, 49) = 0.3912	P=0.9201
Age	8746	8	1093	F (8, 49) = 0.4821	P=0.8629
Genotype	2.306	1	2.306	F (1, 49) = 0.001017	P=0.9747
Residual	111115	49	2268		

Table S15. Two-way ANOVA analysis of rotarod performance between CHCHD10-WT (H) and CHCHD10-R15L (M) transgenic male mice. Related to Figure S2C, Table S16.

Sidak's multiple comparisons test	Predicted (LS) mean diff.	95.00% CI of diff.	Adjusted P Value
R15L (M) - WT (H) (Days)			
60	34.08	-58.33 to 126.5	0.9549
120	-3.578	-95.98 to 88.83	>0.9999
180	7.183	-85.22 to 99.59	>0.9999
240	-6.833	-104.2 to 90.57	>0.9999
300	18.36	-79.04 to 115.8	0.9997
360	-2.269	-107.5 to 102.9	>0.9999
420	22.71	-82.50 to 127.9	0.999
480	-35.07	-147.5 to 77.40	0.9847
540	-38.15	-197.2 to 120.9	0.9977

Table S16. Holm-Šidák post hoc statistical analysis of rotarod performance between CHCHD10-WT (H) and CHCHD10-R15L (M) transgenic male mice for each timepoint. Related to Figure S2C, Table S15.

Two-way ANOVA	Ordinary	
Alpha	0.05	
Source of Variation	% of total variation	P value
Interaction	3.241	0.9678
Age	2.92	0.9722
Genotype	3.952	0.1324

ANOVA table	SS (Type III)	DF	MS	F (DFn, DFd)	P value
Interaction	5085	8	676.9	F (8, 59) = 0.2869	P=0.9678
Age	4582	8	644.7	F (8, 59) = 0.2733	P=0.9722
Genotype	6201	1	5492	F (1, 59) = 2.328	P=0.1324
Residual	139987	59	2359		

Table S17. Two-way ANOVA analysis of rotarod performance between CHCHD10-WT (L) and CHCHD10-WT (H) transgenic male mice. Related to Figure S2C, Table S18.

Sidak's multiple comparisons test	Predicted (LS) mean diff.	95.00% CI of diff.	Adjusted P Value
WT (L) - WT (H) (Days)			
60	-10.39	-103.3 to 82.56	>0.9999
120	-21.56	-114.5 to 71.39	0.9983
180	8.917	-84.03 to 101.9	>0.9999
240	-17.5	-110.4 to 75.45	0.9997
300	-1.467	-94.42 to 91.48	>0.9999
360	-24.46	-117.4 to 68.49	0.9956
420	-9.206	-102.2 to 83.74	>0.9999
480	-48.52	-149.7 to 52.67	0.8212
540	-38.48	-144.3 to 67.35	0.9602

Table S18. Holm-Šidák post hoc statistical analysis of rotarod performance between CHCHD10-WT (L) and CHCHD10-WT (H) transgenic male mice for each timepoint. Related to Figure S2C, Table S17.

Two-way ANOVA	Ordinary	
Alpha	0.05	
Source of Variation	% of total variation	P value
Interaction	15.81	0.0081
Age	27.37	<0.0001
Genotype	21.25	<0.0001

ANOVA table	SS	DF	MS	F (DFn, DFd)	P value
Interaction	649	13	49.93	F (13, 74) = 2.449	P=0.0081
Age	1124	13	86.42	F (13, 74) = 4.24	P<0.0001
Genotype	872.2	1	872.2	F (1, 74) = 42.79	P<0.0001
Residual	1508	74	20.38		

Table S19. Two-way ANOVA analysis of body weight between CHCHD10-WT (L) and CHCHD10-R15L (M) transgenic female mice. Related to Figure 2C, Table S20.

Sidak's multiple comparisons test	Mean Diff.	95.00% CI of diff.	Adjusted P Value
WT (L) - R15L (M) (Days)			
60	-1.25	-10.83 to 8.333	>0.9999
120	-2.5	-12.08 to 7.083	0.9997
180	-0.125	-9.708 to 9.458	>0.9999
240	2.775	-6.808 to 12.36	0.999
300	4.175	-5.408 to 13.76	0.952
360	3.925	-5.658 to 13.51	0.9707
420	6.225	-3.358 to 15.81	0.5469
480	9.85	0.2667 to 19.43	0.0393
540	11.78	2.192 to 21.36	0.006
600	11.85	2.267 to 21.43	0.0055
660	12.18	2.592 to 21.76	0.0039
720	10.63	-1.112 to 22.36	0.1087
780	8.55	-6.603 to 23.7	0.7509
840	10.55	-6.049 to 27.15	0.5812

Table S20. Holm-Šidák post hoc statistical analysis of body weight between CHCHD10-WT (L) and CHCHD10-R15L (M) transgenic female mice for each timepoint. Related to Figure 2C, Table S19.

Two-way ANOVA	Ordinary	
Alpha	0.05	
Source of Variation	% of total variation	P value
Interaction	13.3	0.0268
Age	44.77	<0.0001
Genotype	1.227	0.132

ANOVA table	SS (Type III)	DF	MS	F (DFn, DFd)	P value
Interaction	116.7	12	9.722	F (12, 77) = 2.095	P=0.0268
Age	392.7	12	32.72	F (12, 77) = 7.051	P<0.0001
Genotype	10.76	1	10.76	F (1, 77) = 2.318	P=0.1320
Residual	357.4	77	4.641		

Table S21. Two-way ANOVA analysis of body weight between CHCHD10-WT (H) and CHCHD10-R15L (M) transgenic female mice. Related to Figure 2C, Table S22.

Sidak's multiple comparisons test	Predicted (LS) mean diff.	95.00% CI of diff.	Adjusted P Value
R15L (M) - WT (H)			
60	0.93	-3.366 to 5.226	>0.9999
120	2.11	-2.186 to 6.406	0.876
180	1.815	-2.481 to 6.111	0.9555
240	2.645	-1.651 to 6.941	0.6165
300	3.035	-1.261 to 7.331	0.4037
360	4.32	0.02395 to 8.616	0.0477
420	1.9	-2.396 to 6.196	0.9379
480	0.725	-3.803 to 5.253	>0.9999
540	-1.375	-5.903 to 3.153	0.9975
600	-1.1	-5.628 to 3.428	0.9998
660	-3.4	-7.928 to 1.128	0.3135
720	-1.883	-7.730 to 3.963	0.9956
780	-0.75	-8.593 to 7.093	>0.9999

Table S22. Holm-Šidák post hoc statistical analysis of body weight between CHCHD10-WT (H) and CHCHD10-R15L (M) transgenic female mice for each timepoint. Related to Figure 2C, Table S21.

Two-way ANOVA	Ordinary	
Alpha	0.05	
Source of Variation	% of total variation	P value
Interaction	9.509	0.0422
Age	30.45	<0.0001
Genotype	27.93	<0.0001

ANOVA table	SS (Type III)	DF	MS	F (DFn, DFd)	P value
Interaction	397.6	12	33.13	F (12, 82) = 1.930	P=0.0422
Age	1273	12	106.1	F (12, 82) = 6.183	P<0.0001
Genotype	1168	1	1168	F (1, 82) = 68.06	P<0.0001
Residual	1407	82	17.16		

Table S23. Two-way ANOVA analysis of body weight between CHCHD10-WT (L) and CHCHD10-WT (H) transgenic female mice. Related to Figure 2C, Table S24.

Sidak's multiple comparisons test	Predicted (LS) mean diff.	95.00% CI of diff.	Adjusted P Value
WT (L) - WT (H)			
60	-0.32	-8.566 to 7.926	>0.9999
120	-0.39	-8.636 to 7.856	>0.9999
180	1.69	-6.556 to 9.936	>0.9999
240	5.42	-2.826 to 13.67	0.5178
300	7.21	-1.036 to 15.46	0.1365
360	8.245	-0.0009181 to 16.49	0.05
420	8.125	-0.1209 to 16.37	0.0566
480	10.58	1.883 to 19.27	0.0068
540	10.4	1.708 to 19.09	0.0083
600	10.75	2.058 to 19.44	0.0056
660	8.775	0.08304 to 17.47	0.0461
720	8.742	-0.6467 to 18.13	0.0882
780	7.8	-2.845 to 18.45	0.3499

Table S24. Holm-Šidák post hoc statistical analysis of body weight between CHCHD10-WT (L) and CHCHD10-WT (H) transgenic female mice for each timepoint. Related to Figure 2C, Table S23.

Two-way ANOVA	Ordinary	
Alpha	0.05	
Source of Variation	% of total variation	P value
Interaction	26.74	<0.0001
Age	24.39	<0.0001
Genotype	20.47	<0.0001

ANOVA table	SS	DF	MS	F (DFn, DFd)	P value
Interaction	727	8	90.88	F (8, 59) = 9.352	P<0.0001
Age	663.1	8	82.88	F (8, 59) = 8.529	P<0.0001
Genotype	556.4	1	556.4	F (1, 59) = 57.26	P<0.0001
Residual	573.4	59	9.718		

Table S25. Two-way ANOVA analysis of body weight between CHCHD10-WT (L) and CHCHD10-R15L (M) transgenic male mice. Related to Figure 2B, Table S26.

Sidak's multiple comparisons test	Mean Diff.	95.00% CI of diff.	Adjusted P Value
WT (L) - R15L (M) (Days)			
60	-1.64	-7.299 to 4.019	0.9912
120	-3.02	-8.679 to 2.639	0.7172
180	-1.66	-7.319 to 3.999	0.9904
240	4.39	-1.613 to 10.39	0.308
300	6.855	0.8524 to 12.86	0.0157
360	8.673	2.139 to 15.21	0.003
420	10.64	4.105 to 17.17	0.0002
480	15.49	8.959 to 22.03	<0.0001
540	12.75	2.746 to 22.75	0.0049

Table S26. Holm-Šidák post hoc statistical analysis of body weight between CHCHD10-WT (L) and CHCHD10-R15L (M) transgenic male mice for each timepoint. Related to Figure 2B, Table S25.

Two-way ANOVA	Ordinary	
Alpha	0.05	
Source of Variation	% of total variation	P value
Interaction	28.48	<0.0001
Age	37.55	<0.0001
Genotype	3.193	0.022

ANOVA table	SS (Type III)	DF	MS	F (DFn, DFd)	P value
Interaction	119.5	8	14.93	F (8, 49) = 6.238	P<0.0001
Age	157.6	8	19.7	F (8, 49) = 8.226	P<0.0001
Genotype	13.4	1	13.4	F (1, 49) = 5.595	P=0.0220
Residual	117.3	49	2.394		

Table S27. Two-way ANOVA analysis of body weight between CHCHD10-WT (H) and CHCHD10-R15L (M) transgenic male mice. Related to Figure 2B, Table S28.

Sidak's multiple comparisons test	Predicted (LS) mean diff.	95.00% CI of diff.	Adjusted P Value
R15L (M) - WT (H) (Days)			
60	0.475	-2.528 to 3.478	>0.9999
120	7.56	4.557 to 10.56	<0.0001
180	1.645	-1.358 to 4.648	0.6817
240	1.05	-2.115 to 4.215	0.9769
300	0.8	-2.365 to 3.965	0.9966
360	1.192	-2.227 to 4.610	0.9682
420	-0.825	-4.244 to 2.594	0.9976
480	-2.133	-5.788 to 1.521	0.6034
540	-1.167	-6.335 to 4.002	0.9986

Table S28. Holm-Šidák post hoc statistical analysis of body weight between CHCHD10-WT (H) and CHCHD10-R15L (M) transgenic male mice for each timepoint. Related to Figure 2B, Table S27.

Two-way ANOVA	Ordinary	
Alpha	0.05	
Source of Variation	% of total variation	P value
Interaction	13.9	<0.0001
Age	32.07	<0.0001
Genotype	28.87	<0.0001

ANOVA table	SS (Type III)	DF	MS	F (DFn, DFd)	P value
Interaction	421	8	52.62	F (8, 60) = 5.353	P<0.0001
Age	971.6	8	121.4	F (8, 60) = 12.35	P<0.0001
Genotype	874.4	1	874.4	F (1, 60) = 88.95	P<0.0001
Residual	589.8	60	9.83		

Table S29. Two-way ANOVA analysis of body weight between CHCHD10-WT (L) and CHCHD10-WT (H) transgenic male mice. Related to Figure 2B, Table S30.

Sidak's multiple comparisons test	Predicted (LS) mean diff.	95.00% CI of diff.	Adjusted P Value
WT (L) - WT (H) (Days)			
60	-1.165	-7.198 to 4.868	0.9996
120	4.54	-1.493 to 10.57	0.2736
180	-0.015	-6.048 to 6.018	>0.9999
240	5.44	-0.5933 to 11.47	0.1041
300	7.655	1.622 to 13.69	0.0051
360	9.865	3.832 to 15.90	0.0001
420	9.815	3.782 to 15.85	0.0002
480	13.36	6.792 to 19.93	<0.0001
540	11.58	4.714 to 18.45	<0.0001

Table S30. Holm-Šidák post hoc statistical analysis of body weight between CHCHD10-WT (L) and CHCHD10-WT (H) transgenic male mice for each timepoint. Related to Figure 2B, Table S29.

	Limb	Belt Speed (cm/s)	Stride (s)	Stride Length (cm)	Stride Frequency (steps/s)				
Average WT (L)	Right Hind	10	0.362	3.633	2.817				
SEM WT (L)	Right Hind		0.010	0.088	0.070				
Average R15L (M)	Right Hind	10	0.398	3.967	2.589				
SEM R15L (M)	Right Hind		0.010	0.093	0.061				
P-Value: WT (L) Vs R15L (M)	Right Hind		0.027	0.028	0.031				

	Limb	Belt Speed (cm/s)	Overlap Distance (cm)						
Average WT (L)	Left Fore	17	1.613						
SEM WT (L)	Left Fore		0.117						
Average R15L (M)	Left Fore	17	1.157						
SEM R15L (M)	Left Fore		0.141						
P-Value: WT (L) Vs R15L (M)	Left Fore		0.039						
	Limb	**Belt Speed (cm/s)**	**Stride (s)**	**Stride Length (cm)**	**Stride Frequency (steps/s)**	**Paw Angle (Degrees)**	**Absolute Paw Angle**	**#Steps**	**Paw Area Variability at Peak Stance (cm^2)**
Average WT (L)	Right Hind	17	0.293	4.967	3.483	17.350	17.350	15.500	0.058
SEM WT (L)	Right Hind		0.007	0.131	0.079	1.325	1.325	0.428	0.009
Average R15L (M)	Right Hind	17	0.325	5.522	3.156	22.467	22.467	13.333	0.039
SEM R15L (M)	Right Hind		0.010	0.161	0.093	1.471	1.471	0.717	0.004
P-Value: WT (L) Vs R15L (M)	Right Hind		0.029	0.029	0.027	0.031	0.031	0.041	0.044

	Limb	Belt Speed (cm/s)	Stance Width (cm)	MIN dA/dT (cm^2/s)	Paw Angle (Degrees)	Absolute Paw Angle (Degrees)	Axis Distance (cm)		
Average WT (L)	Left Hind	24	2.180	-11.840	16.060	16.060	1.204		
SEM WT (L)	Left Hind		0.086	0.481	2.168	2.168	0.053		
Average R15L (M)	Left Hind	24	2.425	-9.283	21.663	21.663	1.315		

SEM R15L (M)	Left Hind		0.037	0.386	0.991	0.991	0.019		
P-Value: WT (L) Vs R15L (M)	Left Hind		0.012	0.002	0.022	0.022	0.040		

Table S31. Summary of statistically significant differences of indicated gait parameters between 120 day old CHCHD10-WT (L) and CHCHD10-R15L (M) transgenic mice.

	Limb	Belt Speed (cm/s)	Midline Distance (cm)			
Average WT (L)	Right Hind	10	2.244			
SEM WT (L)	Right Hind		0.218			
Average R15L (M)	Right Hind	10	1.659			
SEM R15L (M)	Right Hind		0.080			
P-Value: WT (L) Vs R15L (M)	Right Hind		0.010			
	Limb	**Belt Speed (cm/s)**	**Propel (s)**	**% Propel Stride**	**% Brake Stance**	**% Propel Stance**
Average WT (L)	Right Fore	17	0.142	43.280	29.500	70.500
SEM WT (L)	Right Fore		0.008	2.540	4.966	4.966
Average R15L (M)	Right Fore	17	0.121	35.250	41.138	58.863
SEM R15L (M)	Right Fore		0.009	2.666	5.112	5.112
P-Value: WT (L) Vs R15L (M)	Right Fore		0.007	0.009	0.030	0.030
	Limb	**Belt Speed (cm/s)**	**Axis Distance (cm)**			
Average WT (L)	Right Hind	17	1.484			
SEM WT (L)	Right Hind		0.083			
Average R15L (M)	Right Hind	17	1.298			
SEM R15L (M)	Right Hind		0.039			
P-Value: WT (L) Vs R15L (M)	Right Hind		0.042			
	Limb	**Belt Speed (cm/s)**	**Stance Width CV (%)**	**MAX dA/dT (cm^2/s)**		
Average WT (L)	Left Fore	24	34.580	18.875		
SEM WT (L)	Left Fore		1.993	2.564		
Average R15L (M)	Left Fore	24	43.610	11.256		
SEM R15L (M)	Left Fore		1.951	1.213		
P-Value: WT (L) Vs R15L (M)	Left Fore		0.015	0.023		
	Limb	**Belt Speed (cm/s)**	**#Steps**			
Average WT (L)	Right Fore	24	22.875			
SEM WT (L)	Right Fore		0.774			
Average R15L (M)	Right Fore	24	18.100			
SEM R15L (M)	Right Fore		1.478			

P-Value: WT (L) Vs R15L (M)	Right Fore		0.033			
	Limb	**Belt Speed (cm/s)**	**#Steps**			
Average WT (L)	Left Hind	24	22.875			
SEM WT (L)	Left Hind		0.875			
Average R15L (M)	Left Hind	24	17.500			
SEM R15L (M)	Left Hind		1.483			
P-Value: WT (L) Vs R15L (M)	Left Hind		0.023			
	Limb	**Belt Speed (cm/s)**	**#Steps**			
Average WT (L)	Right Hind	24	23.000			
SEM WT (L)	Right Hind		0.816			
Average R15L (M)	Right Hind	24	17.900			
SEM R15L (M)	Right Hind		1.065			
P-Value: WT (L) Vs R15L (M)	Right Hind		0.008			

Table S32. Summary of statistically significant differences of indicated gait parameters between 600 day old CHCHD10-WT (L) and CHCHD10-R15L (M) transgenic mice.

	4 Months		**20 Months**	
Belt Speed (cm/s)	**WT (L) (n)**	**R15L (M) (n)**	**WT (L) (n)**	**R15L (M) (n)**
10	6	9	5	9
17	6	9	5	8
24	5	8	4	5

Table S33. Summary of the number of mice (n) of the indicated age and genotype that successfully completed the Digigait task.

Axon Area	P value	Mean WT (L)	Mean R15L (M)
<0.005	0.993	18.090	18.050
<0.010	0.217	18.940	16.510
<0.020	0.083	11.860	14.830
<0.030	0.720	11.200	10.570
<0.040	0.336	7.590	10.040
<0.050	0.172	5.616	7.860
<0.060	0.399	5.052	6.567
<0.070	0.401	6.201	4.709
<0.080	0.402	7.246	5.535
<0.090	0.686	4.565	3.620
<0.100	0.373	2.249	4.393
<0.110	0.303	1.034	2.348

Table S34. Summary of unpaired t-test statistical analysis of the percentage of axons of a particular caliber comprising the femoral nerve motor branch population. Related to Figure S9D.

Two-way ANOVA	Ordinary	
Alpha	0.05	
Source of Variation	**% of total variation**	**P value**
Interaction	1.909	0.9153
Row Factor	50.34	<0.0001
Column Factor	11.48	<0.0001

ANOVA table	SS (Type III)	DF	MS	F (DFn, DFd)	P value
Interaction	42.07	11	3.824	F (11, 87) = 0.4728	P=0.9153
Row Factor	1109	11	100.9	F (11, 87) = 12.47	P<0.0001
Column Factor	253.0	1	253.0	F (1, 87) = 31.28	P<0.0001
Residual	703.7	87	8.089		

Table S35. Two-way ANOVA analysis of body weight between C57BL/6J and Chchd10-KO male mice. Related to Figure 8A, Table S36.

Sidak's multiple comparisons test	Predicted (LS) mean diff.	95.00% CI of diff.	Adjusted P Value
C57BL/6 - Chchd10-KO (Days)			
60	1.537	-3.351 to 6.425	0.9951
120	1.277	-3.778 to 6.331	0.9994
180	1.540	-3.739 to 6.819	0.9976
240	3.280	-1.999 to 8.559	0.5903
300	3.320	-1.959 to 8.599	0.5723
360	4.280	-0.9994 to 9.559	0.2107
420	2.960	-2.319 to 8.239	0.7303
480	4.140	-1.139 to 9.419	0.2506
540	5.000	-0.2794 to 10.28	0.0771
600	3.760	-3.224 to 10.74	0.7775
660	3.350	-3.634 to 10.33	0.8813
720	5.300	-4.339 to 14.94	0.7536

Table S36. Holm-Šidák post hoc statistical analysis of body weight between C57BL/6J and Chchd10-KO male mice for each timepoint. Related to Figure 8A, Table S35.

Two-way ANOVA	Ordinary	
Alpha	0.05	
Source of Variation	**% of total variation**	**P value**
Interaction	3.187	0.9628
Row Factor	35.06	<0.0001
Column Factor	0.008149	0.9071

ANOVA table	SS (Type III)	DF	MS	F (DFn, DFd)	P value
Interaction	107.2	13	8.244	F (13, 103) = 0.4115	P=0.9628
Row Factor	1179	13	90.69	F (13, 103) = 4.527	P<0.0001
Column Factor	0.2740	1	0.2740	F (1, 103) = 0.01368	P=0.9071
Residual	2064	103	20.03		

Table S37. Two-way ANOVA analysis of body weight between C57BL/6J and Chchd10-KO female mice. Related to Figure 8B, Table S38.

Sidak's multiple comparisons test	Predicted (LS) mean diff.	95.00% CI of diff.	Adjusted P Value
C57BL/6 - Chchd10-KO (Days)			
60	0.09667	-7.965 to 8.158	>0.9999
120	-0.5900	-8.652 to 7.472	>0.9999
180	-0.9067	-8.968 to 7.155	>0.9999
240	2.530	-5.532 to 10.59	0.9977
300	0.4067	-7.655 to 8.468	>0.9999
360	1.467	-6.595 to 9.528	>0.9999
420	2.213	-5.848 to 10.27	0.9995
480	2.280	-6.140 to 10.70	0.9995
540	1.880	-6.540 to 10.30	>0.9999
600	0.6200	-8.311 to 9.551	>0.9999
660	-1.200	-10.92 to 8.523	>0.9999
720	-1.900	-12.07 to 8.268	>0.9999
780	-3.750	-15.28 to 7.780	0.9967
840	-4.500	-17.81 to 8.813	0.9952

Table S38. Holm-Šidák post hoc statistical analysis of body weight between C57BL/6J and Chchd10-KO female mice for each timepoint. Related to Figure 8B, Table S37.

Two-way ANOVA	Ordinary	
Alpha	0.05	
Source of Variation	**% of total variation**	**P value**
Interaction	3.487	0.8152
Row Factor	5.081	0.5140
Column Factor	0.2418	0.4470

ANOVA table	SS (Type III)	DF	MS	F (DFn, DFd)	P value
Interaction	14287	13	1099	F (13, 217) = 0.6439	P=0.8152
Row Factor	20821	13	1602	F (13, 217) = 0.9384	P=0.5140
Column Factor	990.6	1	990.6	F (1, 217) = 0.5804	P=0.4470
Residual	370352	217	1707		

Table S39. Two-way ANOVA analysis of rotarod performance between C57Bl/6J and Chchd10-KO mice. Related to Figure 8D, Table S40.

Sidak's multiple comparisons test	Predicted (LS) mean diff.	95.00% CI of diff.	Adjusted P Value
C57BL/6 - Chchd10 KO/KO			
60	-16.00	-67.06 to 35.06	0.9980
120	2.165	-49.81 to 54.14	>0.9999
180	-15.46	-68.50 to 37.58	0.9991
240	-0.8131	-53.85 to 52.22	>0.9999
300	2.531	-50.51 to 55.57	>0.9999
360	-15.90	-68.94 to 37.14	0.9987
420	11.61	-41.43 to 64.64	>0.9999
480	-19.49	-73.77 to 34.80	0.9922
540	-3.856	-58.14 to 50.43	>0.9999
600	-23.60	-86.28 to 39.08	0.9878
660	-32.37	-98.85 to 34.12	0.9039
720	-18.60	-94.69 to 57.48	0.9999
780	-4.675	-102.0 to 92.65	>0.9999
840	69.06	-52.33 to 190.4	0.7568

Table S40. Holm-Šidák post hoc statistical analysis of rotarod performance between C57BL/6J and Chchd10-KO mice for each timepoint. Related to Figure 8D, Table S39.

Two-way ANOVA	Ordinary	
Alpha	0.05	
Source of Variation	**% of total variation**	**P value**
Interaction	6.914	0.8206
Row Factor	6.999	0.8137
Column Factor	0.1115	0.7162

ANOVA table	SS (Type III)	DF	MS	F (DFn, DFd)	P value
Interaction	16924	13	1302	F (13, 103) = 0.6338	P=0.8206
Row Factor	17132	13	1318	F (13, 103) = 0.6416	P=0.8137
Column Factor	273.0	1	273.0	F (1, 103) = 0.1329	P=0.7162
Residual	211558	103	2054		

Table S41. Two-way ANOVA analysis of rotarod performance between C57Bl/6J and Chchd10-KO female mice. Related to Figure 8F, Table S42.

Sidak's multiple comparisons test	Predicted (LS) mean diff.	95.00% CI of diff.	Adjusted P Value
C57BL/6 - Chchd10 KO/KO (Days)			
60	-31.69	-113.3 to 49.94	0.9825
120	-3.281	-84.91 to 78.34	>0.9999
180	-12.37	-94.00 to 69.25	>0.9999
240	-6.985	-88.61 to 74.64	>0.9999
300	25.02	-56.60 to 106.6	0.9982
360	-12.19	-93.81 to 69.44	>0.9999
420	27.81	-53.81 to 109.4	0.9948
480	-8.200	-93.46 to 77.06	>0.9999
540	7.844	-77.41 to 93.10	>0.9999
600	-23.66	-114.1 to 66.77	0.9997
660	-32.02	-130.5 to 66.42	0.9967
720	-31.14	-134.1 to 71.82	0.9985
780	-10.92	-127.7 to 105.8	>0.9999
840	69.06	-65.75 to 203.9	0.8592

Table S42. Holm-Šidák post hoc statistical analysis of rotarod performance between C57BL/6J and Chchd10-KO female mice for each timepoint. Related to Figure 8F, Table S41.

Two-way ANOVA	Ordinary		
Alpha	0.05		
Source of Variation	**% of total variation**	**P value**	**P value summary**
Interaction	3.208	0.9851	ns
Row Factor	6.707	0.8082	ns
Column Factor	2.552	0.1112	ns

ANOVA table	SS (Type III)	DF	MS	F (DFn, DFd)	P value
Interaction	4858	11	441.6	F (11, 87) = 0.2960	P=0.9851
Row Factor	10157	11	923.3	F (11, 87) = 0.6188	P=0.8082
Column Factor	3864	1	3864	F (1, 87) = 2.589	P=0.1112
Residual	129824	87	1492		

Table S43. Two-way ANOVA analysis of rotarod performance between C57Bl/6J and Chchd10-KO male mice. Related to Figure 8F, Table S44.

Sidak's multiple comparisons test	Predicted (LS) mean diff.	95.00% CI of diff.	Adjusted P Value
C57BL/6 - Chchd10 KO/KO (Days)			
60	-1.686	-68.07 to 64.70	>0.9999
120	7.611	-61.04 to 76.26	>0.9999
180	-19.09	-90.79 to 52.62	0.9990
240	8.356	-63.35 to 80.06	>0.9999
300	-20.42	-92.13 to 51.28	0.9981
360	-18.56	-90.26 to 53.15	0.9992
420	-3.244	-74.95 to 68.46	>0.9999
480	-30.78	-102.5 to 40.93	0.9419
540	-15.56	-87.26 to 56.15	0.9999
600	-28.54	-123.4 to 66.31	0.9967
660	-30.59	-125.4 to 64.27	0.9939
720	-2.815	-133.7 to 128.1	>0.9999

Table S44. Holm-Šidák post hoc statistical analysis of rotarod performance between C57BL/6J and Chchd10-KO male mice for each timepoint. Related to Figure 8F, Table S43.

Transparent Methods

Construction of *CHCHD10* Transgene and Development of Transgenic Mice

The 6.4kb *CHCHD10* transgene was amplified in 3 fragments from a human BAC clone RP11 124F9. This transgene includes 3.4kb upstream of the transcription start site to ensure inclusion of the endogenous *CHCHD10* promoter. A 2.8kb fragment was PCR amplified from the BAC clone using a *Kpn*I-anchored primer (P1 5'-CATAGGTACCTTCAGTCTCATCCCTGATTTTCGGGGT-3') and a primer immediately downstream from a *Sac*II restriction site (P2 5'- CTGCCAATGCTGGCAGCCTTACGCAGT-3'). This PCR product was digested with *Kpn*I and *Sac*II (New England Biolabs, Inc.), agarose gel purified, and cloned into the *pBluescript* II SK(-) plasmid vector. A 1.3kb fragment was PCR amplified from the BAC clone using a primer that includes the *Sac*II restriction site (P3 5'-GCCTCATATCCCCCGCGGGCACTGCGTAAG-3') and a primer immediately downstream from an *Xho*I restriction site (P4 5'- GGACACTTGGGCAGCTCCCTGTGTG-3'). This PCR product was digested with *Sac*II and *Xho*I (New England Biolabs, Inc.), agarose gel purified, and cloned into the *pBluescript* II SK(-) plasmid vector. A 2.3kb fragment was PCR amplified from the BAC clone using a primer that includes the *Xho*I restriction site (P5 5'-CCGAGGATTATCTCGAGGCCACACAG-3') and a primer that includes a *Bam*HI restriction site (P6 5'-CAGAGTGGGATCCCTTCCTGCAGGAC-3'). This PCR product was digested with *Xho*I and *Bam*HI (New England Biolabs, Inc.), agarose gel purified, and cloned into the *pBluescript* II SK(-) plasmid vector. A c.44 G > T (p.R15L) mutation was introduced into the 1.3kb *Sac*II/*Xho*I fragment by site-directed mutagenesis (QuikChange Multi Site-Directed Mutagenesis Kit, #200515, Agilent Technologies, Inc.) (P7 5'- TCCCACCCCGCAGCC**T**CCC**A**GCCGCGCCCT-3'; bold **T** indicates mutation site, bold **A** indicates a single nucleotide polymorphism, rs179468). The entire CHCHD10-WT and CHCHD10-R15L transgenes were assembled by ligation of the 2.8kb *Kpn*I/*Sac*II fragment, 1.3kb *Sac*II/*Xho*I fragment and 2.3kb *Xho*I/*Bam*HI fragment into the *pBluescript* II SK(-) plasmid vector. The transgenes were released from their respective plasmids by restriction digestion with *Kpn*I and *Bam*HI, agarose-gel purified, and used for microinjection into fertilized eggs derived from a zygote of a C57BL/6 × SJL cross. Transgenic mice were identified by PCR using a primer set (CHCHD10-P8 5'-CCAGGTTTGAAACGCACCTCCA-3' and CHCHD10-P9 5'-AGCTATCTGGGTACAATCTGGTGTTGTG-3'). The relative transgene copy number was estimated by PCR using transgene-specific primers (CHCHD10-P8 and CHCHD10-P9) and mouse beta-actin gene specific primers (Actb-P10, 5′-TGTTACCAACTGGGACGACA-3′ and Actb-P11, 5′-ACCTGGGTCATCTTTTCACG-3′) in the same PCR system. Subsequent generations were backcrossed on to a C57BL/6J background. Two CHCHD10-WT and three CHCHD10-R15L founder lines were established and studied.

Development of *Chchd10* Knockout Mice

Mouse embryonic stem cells (ESCs) harboring a *Chchd10* knockout allele (Chchd10$^{tm1(KOMP)Vlcg}$, Project ID: 13977) were acquired from the UC Davis Knockout Mouse Project Repository. This allele replaces 1725bp of *Chchd10* (chr10:75,935,967-75,937,691) with a LacZ reporter and neomycin selection cassette. The ESCs were implanted into a female mouse and resulting chimeric mice were interbred with C57BL/6J mice and heterozygous knockout mice were identified by PCR using knockout allele-specific primers (Chchd10-KO-P12, 5'-CACCTGACTCTAAGGACGCTGCCGT-3' and Chchd10-KO-P13, 5'-CCGTTCAAAGATCTGAGTTGCTGGC-3'). Homozygous knockout mice were obtained by interbreeding heterozygous knockout mice and identified by PCR using knockout allele-specific primers and mouse Chchd10-specific primers (Chchd10-P14, 5'-CTGCCAGGCCGGTCAGGTGAGAG-3' and Chchd10-P15, 5'-CCAGTGGGACCCTCGTTTAGACT-3').

Animal Care and Use

Animal-use protocols have been approved by the Institutional Animal Care and Use Committee of Northwestern University for this project. All experiments were carried out according to regulatory standards. The mice used in this study were maintained on a C57BL/6J background (The Jackson Laboratory, stock no. 000664) and were housed in pathogen-free conditions in microisolator cages in the barrier facilities of Northwestern University Center for Comparative Medicine.

qRT-PCR

Total RNA was isolated from mouse spinal cord using an RNeasy Lipid Tissue Mini Kit (74804, Qiagen). Reverse transcription was carried out using a BcaBEST™ RNA PCR Kit (RR023A, Takara Bio Inc.) and quantitative PCR was performed using iTaq™ Universal SYBR® Green Supermix (1725121, Bio-Rad Laboratories, Inc.) and a QuantStudio™ 7 Flex Real-Time PCR System (Applied Biosystems). Primers used in quantitative PCR include (Chchd10 qRT-PCR F-P16, 5'-CTCCTATGAGATCAAGCAGTTCC-3' and Chchd10 qRT-PCR R-P17, 5'-AGCTCAGACCGTGATTGTATTT-3', Gapdh qRT-PCR F-P18, 5'- AACAGCAACTCCCACTCTTC-3' and Gapdh qRT-PCR R-P19, 5'- CCTGTTGCTGTAGCCGTATT-3'.

Mouse Behavioral Testing

CHCHD10-WT (H), CHCHD10-WT (L) and CHCHD10-R15L (M) mice were tested on a RotaRod task every 60 days beginning at 60 days of age. Each test involved a trial on 3 consecutive days with each trial consisting of 3 experiments separated by at least 5 minutes. The latency to fall was recorded for each mouse as the RotaRod (Ugo Basile) accelerated from 5rpm to 40rpm up to a maximum of 5 minutes. Results indicate the average latencies to fall of all

experiments per test. The body weight of this cohort of mice was measured every 60 days beginning at 60 days of age. Separate cohorts of 4 month or 14-20 month old mice were subjected to an open field task. Each mouse was placed in a novel open field environment for five minutes and their movements were video recorded. Limelight software (Coulbourn Instruments) was used to determine total distance travelled, velocity and duration of time spent in the periphery and center of the open field. Gait analysis was carried out on 4 month and 20 month old mice using a DigiGait (Mouse Specifics, Inc.). Mice were placed on a treadmill moving at 10cm/s, 17cm/s and 24cm/s and various parameters related to gait features were recorded and analyzed using the DigiGait software. The numbers and gender of mice used are indicated in the figures and/or figure legends.

Immunohistochemistry and Confocal Microscopy
Mice were deeply anesthetized and transcardially perfused with 4% paraformaldehyde (Electron Microscopy Sciences). 6µm sections were cut from paraffin-embedded spinal cord and brain. The sections were deparaffinized with xylene and rehydrated with a descending series of diluted ethanol and water. Antigens in the sections were retrieved using 1X antigen decloaker, a citrate buffer heat retrieval solution, pH 6.0 (Biocare Medical), and a high-pressure decloaking chamber. For immunohistochemistry, endogenous peroxidase activity was blocked with 3% hydrogen peroxide (BioGenex). Non-specific background was blocked with 1% bovine serum albumin (BSA) (Sigma Aldrich). Primary antibodies were diluted in 1% BSA and applied to sections at 4ºC overnight. Biotinylated goat anti-rabbit and anti-mouse IgG were used as the secondary antibodies (Biocare Medical). Immunoreactive signals were detected with peroxidase-conjugated streptavidin (BioGenex) using 3-amino-9-ethylcarbazole (BioGenex) as a chromogen. The slides were counterstained with hematoxylin and mounted with Aqua PolyMount (Polyscience). Brightfield light microscopy imaging was performed using an Olympus AX70 microscope. For confocal microscopy, non-specific background was blocked with 1% BSA. Primary antibodies were diluted in 1% BSA and applied to sections at 4ºC overnight. The appropriate secondary anti-rabbit, anti-mouse or anti-goat IgG, conjugated with Alexa Fluor 488 or Alexa Fluor 555 (Invitrogen) were diluted in 1% BSA for 1 hour at room temperature. The slides were mounted with ProLong™ Gold antifade reagent with or without DAPI (Invitrogen). Fluorescence was detected using a Nikon A1R+ Confocal Laser Microscope System.

Antibodies
We designed and synthesized an antibody which was raised in rabbit using a polypeptide of human CHCHD10 (amino acids 17-30: AAPSAHPPAHPPPSA) (Biosynthesis, Inc.) The antiserum was affinity-purified. Other antibodies used in this study include anti-CHCHD10 (AP16303a, Abgent, Inc.; 25671-1-AP, Proteintech Group, Inc.; MABN1524, Millipore Sigma; HPA003440, Sigma), anti-ubiquitin (10R-U101b, Fitzgerald Industries International), anti-SQSTM1/P62 (H00008878-M01, Abnova), anti-ATP Synthase α subunit (612517, BD Transduction), COX IV subunit VIb (A-21366, Molecular Probes), anti-Map2 (M1406, Sigma), anti-SMI 32 (801701, Biolegend), anti-SMI 310R (Covance), anti-NF-68 (N5139, Sigma), and anti-ChAT (AB144p, Millipore), anti-TDP-43 (10782-2-AP, Proteintech).

Western Blotting
Mouse forebrain lysate was prepared using RIPA buffer (50mM Tris pH 8.0, 150mM NaCl, 1% NP-40, 0.1% SDS, 0.5% Sodium Deoxycholate, 1X Halt™ Protease and Phosphatase Inhibitor Cocktail (Thermo Scientific)). Protein concentration was determined using a Pierce™ BCA Protein Assay Kit (Thermo Scientific). 15µg total protein was separated on NuPAGE™ 4-12% Bis-Tris Protein Gels (Thermo Scientific) by electrophoresis and blotted onto PVDF membrane (Bio-Rad Laboratories, Inc.). Membranes were blocked with 5% milk in PBS with 0.1% Tween20® (Sigma-Aldrich). Anti-CHCHD10 (AP16303a, Abgent, Inc.) diluted in 5% BSA (Sigma-Aldrich) was applied to the membranes overnight at 4ºC. Secondary goat anti-rabbit IgG (H+L)-HRP conjugate (1721019, Bio-Rad Laboratories, Inc.) was diluted in 5% milk in PBS with 0.1% Tween20 and applied for 1 hour at room temperature. Chemiluminescence upon application of Immobilon™ Western Chemiluminescent HRP Substrate (Millipore) was detected using an Azure Biosystems c600 imaging system. The membranes were stripped using Restore™ Western Blot Stripping Buffer (Thermo Scientific) and re-probed with anti-GAPDH (NB300-324, Novus Biologicals) to serve as a loading control.

Electron Microscopy
Mice were transcardially perfused under deep anesthesia with fixative (4% paraformaldehyde and 2.5% glutaraldehyde in 0.1M phosphate buffer (Electron Microscopy Sciences)). Post-fixation in 1% OsO_4 in 0.1M phosphate buffer was followed by dehydration through an ethanol series and propylene oxide before embedding using an EMbed812 kit (Electron Microscopy Sciences). 1µm semithin sections were stained with toluidine blue. 100nm ultrathin sections were contrasted with uranyl acetate, lead nitrate and sodium citrate. Electron microscopy images were acquired using an FEI Tecnai Spirit G2 transmission electron microscope.

Femoral Nerve Motor Branch Axon Counts
Dissection and procedure was carried out as described (Burgess et al., 2010). Nerve tissue was processed and embedded as described for electron microscopy sample preparation. 1µm semithin sections were stained with toluidine

blue. Light microscopy images were acquired using an Olympus AX70 microscope and merged using Photoshop. Axons numbers and areas were counted and calculated using Fiji software.

Mouse primary spinal cord neuron culture
Primary neurons from mouse spinal cords were cultured in Neurobasal™ medium (Life Technologies) supplemented with B-27™ (Life Technologies). Spinal cords from E12.5 mouse embryos were dissected out and dissociated with 0.25% trypsin. After enriching motor neurons with Optiprep™ (Sigma) density gradient centrifugation and a BSA cushion, cells were seeded on glass coverslips coated with 20µg/ml poly-L-lysine (Sigma) and 8µg/ml laminin (Sigma) and grown in the presence of 50µg/ml BDNF, 50µg/ml CNTF, and 25µg/ml GDNF (PeproTech). Neurons were transfected with Lipofectamine™ 2000 (Life Technologies) following manufacturer's instructions.

Oxygen Consumption Rate Measurements in Primary Spinal Cord Neurons
Primary spinal cord neuron mitochondrial oxygen consumption rates (OCR) were measured using a Seahorse XFe96 Analyzer (Agilent). Basal mitochondrial OCR was determined by subtracting the OCR following antimycin A (Sigma) and rotenone (Sigma) treatment from the baseline OCR. OCR was normalized to cell number quantified by DAPI staining.

Live imaging and data analysis of mitochondria transport, density and fragmentation
Time-lapse live imaging by confocal microscope was used to measure axonal mitochondrial transport, density and fragmentation. After culturing for 5–7 days, primary spinal cord neurons were transfected with mitochondria targeting sequence-tagged DsRed (mito-DsRed). 48 hours after transfection, images were acquired using a Zeiss LSM 700 confocal microscope equipped with a 63X/NA 1.15 water LD C-Apochromat objective lens and a temperature (37ºC) and CO_2 (5%) controlled stage. Images were captured every two seconds for a period of two minutes using Zen 2009 software. The 561nm laser intensity was set at 0.2mW to minimize damage, and pinholes were opened maximally to allow the entire thickness of the axon to be imaged. Axon fragments of 50-100µm in length located at least 50µm away from the cell body were selected for analysis. Custom-made Image J plug-ins were used to generate kymographs and analyze mitochondria motility (Pekkurnaz et al., 2014). Distance travelled was defined as the average distance travelled by each mitochondrion in one minute; Percent of Time was defined as the average of time spent mobile in each direction. Mitochondria that moved continuously in one direction were scored as 100% of Time in motion for that direction, while those that were entirely stationary or only moved in the opposite direction were scored as 0% Time in motion for that direction. Mitochondria length and density were measured by using the first frame of each time-lapse recording on selected axons, and analyzed with Imaris software (Bitplane). Mitochondria density was calculated by dividing the total length of mitochondria with the length of axon in the same view field.

Skeletal Muscle and Heart Sample Preparation
Quadriceps, gastrocnemius and diaphragm skeletal muscle was collected from deeply anesthetized mice and flash frozen in liquid nitrogen-cooled isopentane. 4µm sections were cut using a cryostat and stained with hematoxylin and eosin. Mouse hearts were immerse fixed in 4% paraformaldehyde and paraffin-embedded. 6µm sections were cut using a microtome and deparaffinization was carried out as descried above. Immunostaining of skeletal and cardiac muscle was carried out as described above.

Skeletal Muscle Respirometry
High-resolution respirometry was performed using an Oroboros O2K (Oroboros Instruments, Innsbruck, Austria) per established protocols (Kuznetsov et al., 2008, LaBarge et al., 2016). Briefly, tibialis anterior and soleus muscles were harvested immediately after euthanasia and preserved in preservation solution (BIOPS; 2.77mM CaK_2EGTA, 7.23mM K_2EGTA, 5.7mM Na_2ATP, 6.56mM $MgCl_2$, 20mM taurine, 15mM Na_2Phosphocreatine, 20mM imidazole, 0.5mM DTT, and 50mM MES). The muscles were mechanically separated in ice-cold BIOPS under a dissecting microscope to obtain replicates of around 2-3mg and permeabilized with 50 µg/ml saponin for 30 min followed by a 10 min wash in mitochondrial respiration media [MiR05; 0.5mM EGTA, 3mM $MgCl_2$, 60mM K-lactobionate, 20mM taurine, 10mM KH_2PO_4, 20mM 4-(2-hydroxyethyl)-1-piperazineethanesulfonic acid, 110mM sucrose, 1g/L fatty acid-free bovine serum albumin]. All data were collected at 37°C in hyperoxygenated (200–400µM O_2) conditions in MiR05 to avoid limitations with oxygen diffusion. The substrate-uncoupler-inhibitor titrations (SUIT) respiration protocol used to test for maximal phosphorylation and electron transport chain capacity of complex-I and complex-II mediated respiration was: 0.5mM malate, 5mM pyruvate, 5mM ADP, 10mM glutamate, 10mM cytochrome c, 10mM succinate, followed by 0.5mM titrations carbonyl cyanide m-chloro phenyl hydrazine (CCCP), 0.5mM rotenone, and 2.5mM antimycin A. Any replicates that were higher than 10% following the addition of cytochrome c were considered to be over-permeabilized and those data were not used. The state of respiration after addition of glutamate is considered complex-I (+III+IV+ATP Synthase) mediated phosphorylation capacity, that after succinate is complex-I+II (+III+IV+ATP Synthase), i.e. maximal phosphorylation capacity and the state after addition of CCCP (uncoupler) is maximal electron transport chain capacity.

Echocardiography
Mice were anesthetized by inhalation of 1.5% isoflurane. Parasternal short axis views were collected using a Vevo® 3100 Imaging System and analyzed with Vevo® LAB software (FUJIFILM Visual Sonics). M-mode measurements were used to calculate the reported parameters.

Supplemental References

BURGESS, R. W., COX, G. A. & SEBURN, K. L. 2010. Neuromuscular disease models and analysis. *Methods Mol Biol,* 602**,** 347-93.

KUZNETSOV, A. V., VEKSLER, V., GELLERICH, F. N., SAKS, V., MARGREITER, R. & KUNZ, W. S. 2008. Analysis of mitochondrial function in situ in permeabilized muscle fibers, tissues and cells. *Nat Protoc,* 3**,** 965-76.

LABARGE, S. A., MIGDAL, C. W., BUCKNER, E. H., OKUNO, H., GERTSMAN, I., STOCKS, B., BARSHOP, B. A., NALBANDIAN, S. R., PHILP, A., MCCURDY, C. E. & SCHENK, S. 2016. p300 is not required for metabolic adaptation to endurance exercise training. *FASEB J,* 30**,** 1623-33.

PEKKURNAZ, G., TRINIDAD, J. C., WANG, X., KONG, D. & SCHWARZ, T. L. 2014. Glucose regulates mitochondrial motility via Milton modification by O-GlcNAc transferase. *Cell,* 158**,** 54-68.